Aalto University
School of Engineering
Department of Mechanical Engineering

Vishesh Lohani

Effects of geometric and material parameters on failure modes of SC elements

Thesis submitted in partial fulfilment of the requirements for the degree of
Master of Science in Technology

Master's Thesis
Espoo, Finland

May 30th, 2016

Supervisor: Prof., Dr. Jukka Tuhkuri, Aalto University
Advisors: Dr. Ludovic Fülöp, VTT Technical Research Centre of Finland Ltd
Dr. Jouni Freund, Aalto University

Author: Vishesh Lohani

Title of thesis: Effects of geometric and material parameters on failure modes of SC elements

Degree Programme: Mechanical Engineering **Major:** Mechanical Engineering **Code:** IA3027

Thesis supervisor: Jukka Tuhkuri

Thesis advisors: Ludovic Fülöp and Jouni Freund

Date: 30.05.2016 **Number of pages:** 80+11 **Language:** English

Abstract

A steel-concrete-steel composite (SC) element resembles double skin sandwich composite structure in which the concrete core is in-filled between steel skins. Mechanical shear connectors connect the skins and they are embedded in concrete. These connectors transfer shear forces and have an important role in performance of composite element. SC element is prone to different failure modes such as flexural failure, de-bonding between steel plate and concrete, and shear failure. There are 3 aims of the thesis to study the effects of geometric and material parameters on the failure modes of SC elements via finite element (FE) method.

Six SC beam specimens are used to examine failure modes in this research. The first two specimens are configured to a four-point bending test with the intention of obtaining flexural failure. The remaining specimens are configured to a three-point bending test with the intention to obtain a shear failure. Based on characteristics of the specimens, models are created and analysed with the aid of commercial Abaqus/Explicit FE software. A quasi-static analysis is accomplished to replicate the experimental behaviour of the specimens. The results of experiments and simulations are compared to validate the models. Failure modes in experiments and simulations are similar. Specimen may fail due to yielding of the tensile steel plate followed by buckling of the compression steel plate or due to vertical shear cracks in the concrete followed by yielding of the shear connectors.

According to the parametric study, the failure of SC beam in bending is affected by thickness of tensile steel plate as well as stud geometry. Failure of SC beam in shear is affected by stud geometric parameters. With increasing tensile plate thickness in bending, the beam fails only because of yielding of tensile steel plate. Geometric parameters and position of studs significantly affect the end slip between concrete and steel plate in both bending and shear failures. Although magnitude of ultimate load is different, the failure modes of SC beams considered in this study are not affected by material properties of steel plates in bending and material properties of tie bars in shear.

Keywords: Failure mode, Finite element method, Parametric study, SC beam, Validation

Acknowledgements

First and foremost, it is a great pleasure to acknowledge my deepest thanks and gratitude to my advisor, Dr. Ludovic Fülöp from VTT Technical Research Centre of Finland for his continuous support, encouragement, and immense knowledge. My gratitude is also owed to my supervisor, prof., Dr. Jukka Tuhkuri and advisor Dr. Jouni Freund from Aalto University for their kind supervision and valuable feedbacks.

Furthermore I would like to thank Dr. Petr Hradil, Vilho Jussila, and Kim Calonius for their assistance and guidance in material modelling, finite element analysis, and documentation during my master thesis work. A special thank goes to 'Infrastructure Health' team as well as other colleague from VTT for their expertise, valuable suggestions and accessibility. I am also thankful to 'RFCS-SCIENCE' project, Radiation and Nuclear Safety Authority (STUK), and Peikko Group for supporting this project.

Last but not the least; my deepest gratitude goes to my parents for all the support throughout my life and to my wife for her patience and understanding.

Thank you!

Vishesh Lohani
Espoo, Finland
May, 2016

Table of Contents

Notation

A_s	Cross-section area of the steel plate
$d_{c/t}$	Damage variables
d_{stud}	Diameter of stud
d_{tie}	Diameter of tie bar
E	Modulus of elasticity
E_{cm}	Elastic modulus of the concrete
f_{ck}	Characteristic compressive cylinder strength of concrete
f_{cm}	Mean value of concrete cylinder compressive strength
f_{ctm}	Mean value of axial tensile strength of concrete
f_u	Ultimate stress
f_y	Yield stress
G_f	Fracture Energy
h_{stud}	Overall nominal height of stud
H	Height of the SC beam
I_{eq}	Equivalent second moment of area about the neutral axis
L	Length of the SC structure
$M_{pl,RD}$	Design plastic bending moment resistance strength
n	Ramberg-Osgood constant
$N_{cu.Rd}$	Expected compressive strength of concrete at crushing
P_{RD}	Design shear resistance strength of a headed stud
$R_{p0.2}$	Proof strength at 0.2% strain
s_{tie}	Spacing between two tie bars
s_{stud}	Spacing between two studs
t_c	Compression plate thickness
V_{RD}	Transverse shear resistance strength of SC beam
W	Width of the SC structure
α	Imperfection factor
γ	Safety factor
δ	Deflection of the beam
ε	Strain
θ	Shear crack angle

ϱ	Density
σ	Stress
τ	Shear stress
υ	Poisson's ratio
χ	Buckling reduction factor

Abbreviations and Acronyms

ACI	American Concrete Institute
CDP	Concrete damage plasticity
CPU	Central processing unit
C3D8R	Continuum, 3-Dimensional, 8-nodes, Reduced integration
DOFs	Degree of freedoms
FE	Finite Element
FEA	Finite Element Analysis
FEM	Finite Element Method
GUI	Graphical User Interface
NPP	Nuclear Power Plant
R3D4	Rigid, 3-Dimensional, 4-nodes
RC	Reinforced Concrete
SC	Steel-Concrete-Steel Composite
S4R	Shell, 4-nodes, Reduced integration
VTT	VTT Technical Research Centre of Finland Ltd

List of Figures

List of Tables

1 Introduction

A steel-concrete-steel composite (SC) element (SC beam) illustrated in Figure 1 resembles double–skin sandwich composite structure in which the concrete is in-filled between outer steel skins which act as permanent formwork [1]. The thin steel plates are connected to concrete by shear connectors (Stud and Tie bar). Studs are welded on the inner surface of the steel plates while tie bars are connecting the steel plates and both are embedded in the concrete [2]. The load transfer between these structural elements is significantly influenced by the interactions of material interfaces in SC beams. The connectors transfer shear forces in vertical as well as in horizontal directions, resist longitudinal slips, and have, therefore, an important role in the performance of composite elements. The structural performance of SC beams shows superiority over reinforced concrete structures in applications required high strength, high ductility, structural integrity, and ability to prevent impact, leakage and explosion [3].

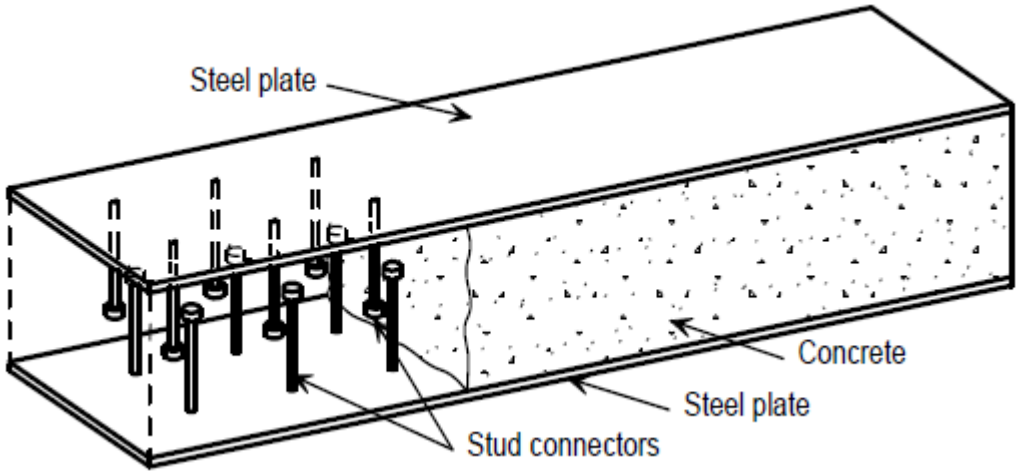

Figure 1: Structure of SC beam [4].

The advantages of SC structures include the elimination of formwork, the elimination of reinforcing bars, the ability to support equipment anywhere on the steel plate without any anchor attachments, and shift of considerable amount of work from construction sites to fabrication shops. SC construction significantly reduces the on-site installation person-hours (illustrated in Figure 2). Additionally, the quantity of steel needed for SC structure is 25% lesser than in a traditional steel-concrete structure. [5] Because of quicker, efficient, and

economic construction processes of SC structure, it can replace reinforced concrete (RC) structures in demanding industrial applications or in difficult construction circumstances.

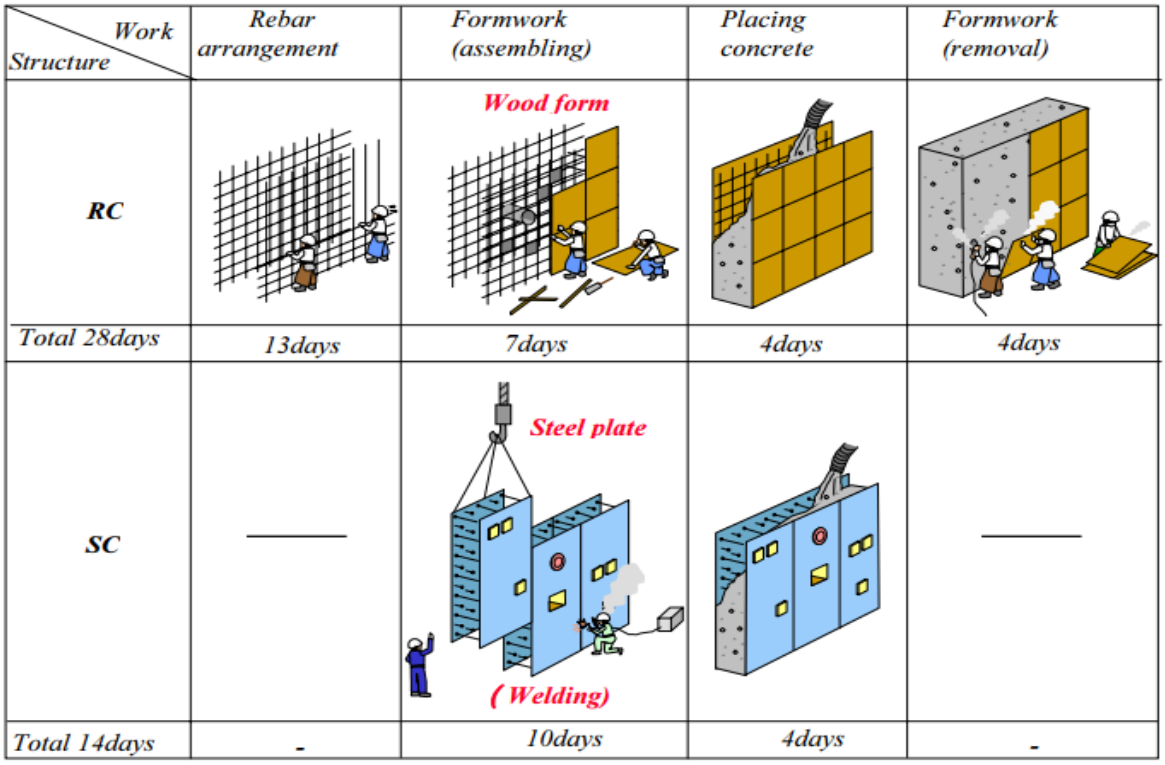

Figure 2: Comparison of construction time of SC and RC structures [5]

Figure 3: (a) Containment module of AP1000 reactor [5] (b) decking system of offshore platforms [6]

Some representative examples of SC structures include foundation of off-shore wind towers, transfer beams in high-rise buildings, beams in industrial structures supporting concentrated

loads, and composite beams in bridges. In addition, SC structures provide blast resistance capability regarding to terrorist attack.[7] Containment module of AP1000 reactor (Westinghouse) and ice-resisting wall of oil production platform (Northstar Island, Alaskan Beaufort Sea) shown in Figure 3(a) and (b) respectively were made from SC structures.

The concept development of SC structure began during 1970s when Solomon et al. proposed an alternative solution of girder and deck for bridge/highway construction. SC beam was designed without mechanical shear connectors. The steel plates were attached to concrete core by means of epoxy resin adhesive in this construction. The adhesive acted as a shear transfer medium between steel plate and concrete core. This beam behaved in the same manner as RC beams [8] without shear reinforcements, exhibited satisfactory bending moment capacity but lack of enough shear strength.[9] To improve structural integrity and performance, different types of mechanical shear connectors were used since 1980s. Double-skin SC construction with headed stud, Bi-steel SC construction with shear bar, and SC construction with J-hook connectors, as illustrated in Figure 4(a), (b) and (c) respectively, represent the state-of-the-art of SC beam construction [10].

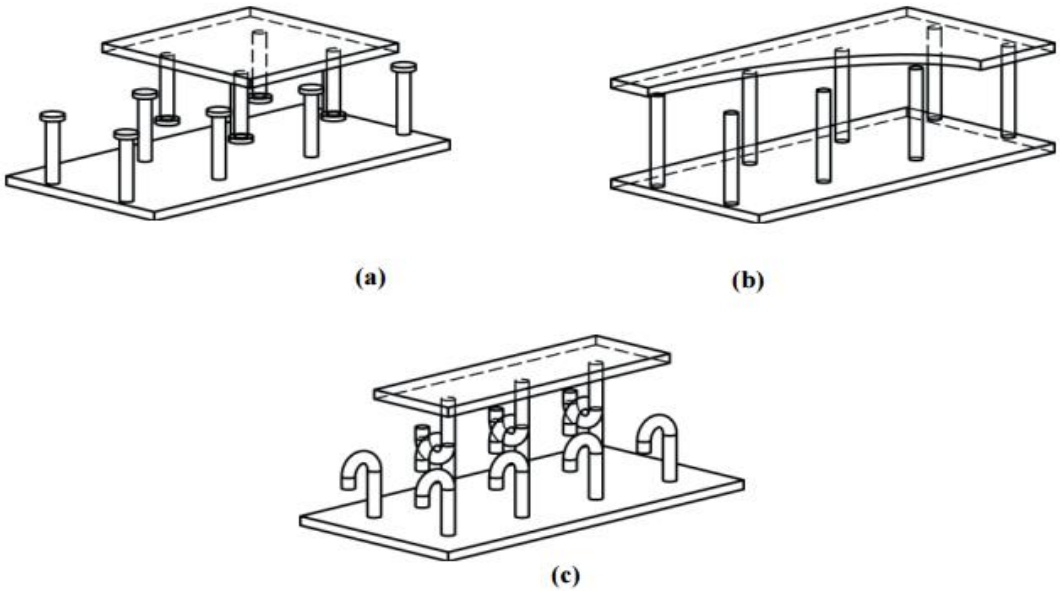

Figure 4: Schematic representation of (a) Double skin SC (b) Bi-steel SC, and (c) SC with J-hook connectors [10]

In ‘Double skin’ SC structure, headed studs are welded to the inner side of steel plate and terminate within the concrete core. These studs not only develop a tie between the core and

the skin but also prevent local buckling of the skin. The first research on the fundamental aspects of double-skin SC structure illustrated in Figure 4(a) was carried out by Oduyemi and Wright in 1989. [3]

Corus Construction & Industrial Ltd initially developed the concepts of Bi-steel SC structure in 1998. Bi-steel SC (illustrated in Figure 4(b)) is another type of SC structure which consists of shear bar connectors. In this SC construction, the strength and composite action of the structure is improved because of the shear bar connectors embedded in concrete core which connect the top and bottom steel plates. The design guidelines for this structure ensure that the tensile plate yields before any other type of failure.[11]

Liew et al. [12] proposed a SC structure with J-hook connectors (illustrated in Figure 4(c)) in 2008. A pair of J-hook is welded to the inner surface of steel plates, interlocked each other and embedded in the concrete core. These connectors provide relatively high tensile capacity due to confinement by the concrete core and transfer shear force between core and skin. The interlocking mechanism of J-hook connectors prevent local buckling phenomena of top steel plate, provide cross sectional shear resistance, and retain the structural integrity.[12]

Apart from SC constructions described above, there is also undergoing research on connectors, e.g., angle connector, C channel connector, corrugated strip connector. Most of the SC studies have been concentrated on the load bearing capacity of SC structure under static and dynamic loading. Although design methodologies and design standards of SC structures with headed stud and Bi-steel are available in literature, they are usually tightly calibrated for a certain failure mode or a few modes and are not endorsed yet in Eurocode perspective. This lack of established design and construction guides has led to uncertainty in the structural design of SC structures.

Research on the SC structure via finite element method has been carried out since 30 years. Shukry (1986), Kumar (2000), and Sohel (2008) did research on SC structure using commercial FE software. FE analysis of a SC structure without shear connectors was carried out by Shukry (1986). In this research, the FE results indicated a stiffer beam than the test results. [13] A series of double skin SC plates were analysed by Kumar (2000). The ultimate strength of SC plates obtained from FE analysis was in good agreements with the test results but was not able to describe interaction between stud and concrete core. [14] Sohel (2008)

carried out FE analysis of a SC structure with J-hook connectors subjected to impact loading. The FE model predicted ultimate strength and failure modes similar to the experiments but the results were limited to impact tests. [15]

1.1 Scope and structure

VTT Technical Research Centre of Finland is actively participating in research activities on SC structures. In the first phase, detailed design of SC beams at ambient temperature was accomplished based on available literature of SC structure and Eurocodes. Based on the design report, experimental analysis of 12 full scale SC beam specimens and push-out test were carried out in the second phase. The interpretation of experiment results and parametric study of SC beams with the aid of FEM are the aims of the third phase.[4][16][17] The objectives of this research are as follow:

a) To formulate and implement a SC beam model
b) To validate the FE results against experiment results
c) To study the effects of geometric and material parameters on failure modes of SC beam

A finite element (FE) software package; Abaqus/Explicit is applied for numerical calculations and data analysis. The implementation of SC beam model is based on the Plug-in technique proposed by Donnadieu and Fülöp [16] which executes in Abaqus by using Python script and Abaqus GUI toolkit. The outcomes of six experiments by Koukkari and Fülöp [17] are used to validate the model. The model is also used to find the main geometric and material parameters affecting the failure modes of SC beam.

Chapter 2 presents the structure and current design rules for a SC beam applied in VTT. The key concepts and fundamental theory behind SC structures presented in this chapter are based on the beam theory. In chapter 3, the failure modes of SC structures are discussed. Geometric parts, geometric parameters, and material models of the SC beam model are presented in chapter 4. Contact modelling, loading, and boundary conditions are also discussed in this chapter. Implementation of SC beam model in the commercial Abaqus/Explicit FE software is

addressed in chapter 5. The experiment results are summarised in chapter 6. The outcomes of FE analysis are compared to experiment results in chapter 7. The effects of geometric and materials parameters are discussed in chapter 8. In chapter 9, a set of conclusions is derived from the parametric study and recommendations are given for the future work in the same area.

2 Structure and design of SC element

In this chapter, structure and design principles of the SC element used in VTT are discussed. Loading is described by shear force and bending moment acting on a cross section of SC beam. It is assumed that the top steel plate and concrete core above the neutral axis are under compression while the bottom steel plate and concrete core below the neutral axis are under tension due to the positive bending moment. Longitudinal shear stress between the interface of steel plate and concrete core and vertical shear stress are also developed due to the shear force.

2.1 Design methodology

The design methodology of a SC beam in VTT is based on the available design specifications in Eurocode and on the beam model. The design method involves ultimate limit state design of the SC beams and beam columns. The following design standards and design documents are primarily used: [4]

a) EN 1990: Eurocode: Basis of structural design
b) EN 1992-1-1: Design of Concrete Structures, General rules and rules for buildings
c) EN 1993-1-1: Design of Steel Structures, General rules and rules for buildings
d) EN 1994-1-1: Design of Composite Steel and Concrete Structures, General rules and rules for buildings
e) The Design Guide for Steel-Concrete-Steel Sandwich Construction "Volume 1: General Principles and Rules for Basic Elements" - The Steel Construction Institute

VTT analysed the different SC beam constructions on the basis of the design standards and documents listed above. The design of SC beam at VTT was proposed (shown in Figure 5) to make use of a top and a bottom steel plate, NELSON headed stud (Appendix III) and a shear bar embedded in concrete core. [4]

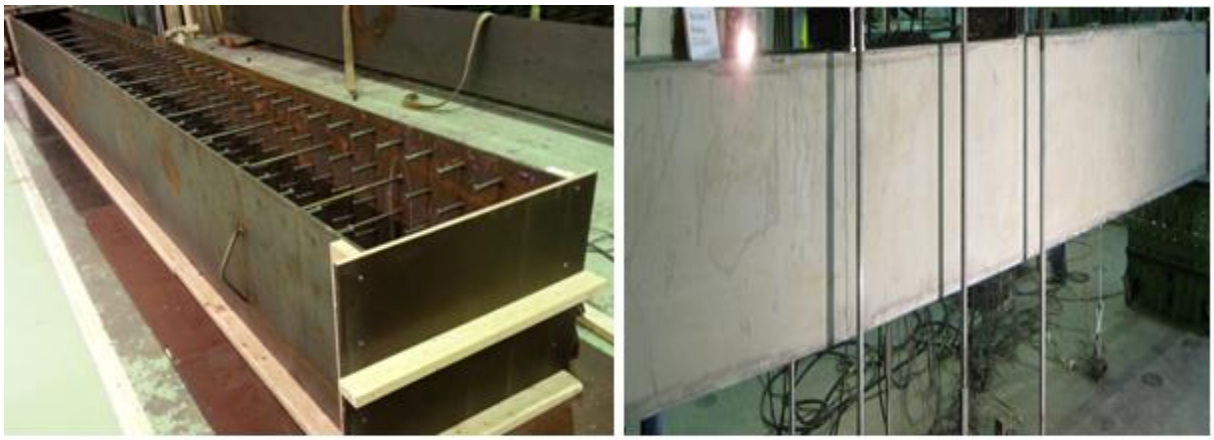

Figure 5: (a) Steel frame and (b) after concreting of SC beam [17]

2.2 Strength of SC beam

In the strength analyses of SC beam, the cross-section is simultaneously subject to bending moment and shear force. For structural integrity, the beam should satisfy the condition [18]

$$\left(\frac{V_{sd}}{V_{pl,Rd}}\right)^2 + \left(\frac{M_{sd}}{M_{pl,Rd}}\right)^2 \leq 1, \tag{2.1}$$

where V_{sd} is the design shear force, M_{sd} is the design bending moment, $V_{pl,Rd}$ is the design plastic shear resistance in the absence of moment, and $M_{pl,Rd}$ is the design plastic moment resistance in the absence of shear.

2.2.1 Moment resistance of SC beam

The moment resistance of SC beam is calculated on the basis of plastic approach because it has fewer assumptions than the elastic approach. [19] The design plastic moment resistance $M_{pl,Rd}$ of SC beam is calculated by taking moments about the centre of the compression steel plate and is given by [18]

$$M_{pl,Rd} = N_{c,Rd}\left(\frac{h_c + t_c}{2}\right) + N_{cu,Rd}\left(\frac{h_c}{2} - \frac{\lambda}{2}x\right) + N_{t,Rd}\left(\frac{h_c + t_t}{2}\right), \quad (2.2)$$

where $N_{c,Rd}$ is the compression force in steel plate, $N_{cu,Rd}$ is the nominal compressive force in concrete, $N_{t,Rd}$ is the tension force in steel plate, t_t is the thickness of the tension steel plate, t_c is the thickness of the compression steel plate, h_c is the depth of concrete core, λ is a coefficient, and x is the plastic neutral axis position. The plastic neutral axis position x can be calculated by equating nominal compressive force in concrete $N_{cu,Rd}$, compression force in steel plate $N_{c,Rd}$, and tension force in steel plate $N_{t,Rd}$. The equations for the different forces and plastic neutral axis position are given by [18][20]

$$N_{cu,Rd} = \frac{\eta f_{ck}\, b\lambda\, x}{\gamma_C}, \quad (2.3)$$

$$N_{c,Rd} = \frac{b t_c f_{ysc}}{\gamma_\alpha}, \quad (2.4)$$

$$N_{t,Rd} = \frac{b t_t f_{ysc}}{\gamma_\alpha}, \quad (2.5)$$

$$x = \frac{\gamma_C}{\gamma_\alpha}\frac{1}{\eta\lambda}\frac{f_{ysc}\,(t_t - t_c)}{f_{ck}}, \quad (2.6)$$

where f_{ck} is the characteristics cylinder compressive strength of the concrete, f_{ysc} is the yield stress of the compression/ tension steel plate, b is the width of the SC section, η is a factor, γ_α is a safety factor ($\gamma_\alpha = 1$ in all cases), and γ_C is also a safety factor ($\gamma_C = 1$).

2.2.2 Shear resistance strength of SC beam

The shear force causes longitudinal and transverse shear stress components in SC beam. Shear stress can lead to the failure of shear connectors during the transfer of longitudinal forces from steel plate to concrete and yielding of shear connectors due to a transverse shear failure. [21] The transverse shear resistance capacity of SC beam consists of two parts: shear resistance provided by concrete acting with steel plates, and shear resistance provided by shear connectors. The design plastic shear resistance strength $V_{pl,Rd}$ is expressed as [18]

$$V_{pl,Rd} = V_{Rd,c} + V_s\,, \tag{2.7}$$

where $V_{Rd,c}$ is the shear resistance provided by concrete, and V_s is the shear resistance provided by shear connectors. According to Eurocode 2, the design shear resistance of a concrete without shear reinforcement is given by [18]

$$V_{Rd,c} = \left[C_{Rd,c}k(100\rho f_{ck})^{1/3} + k_1\sigma_{cp}\right]b_w h_c\,, \tag{2.8}$$

where $C_{Rd,c} = 0.18/\gamma_c$ for normal weight concrete, γ_c is the partial safety factor, $k = 1 + \sqrt{200/h_c} \leq 2$ with h_c in mm, h_c is the depth of concrete core, $\rho = A_{sl}/b_w h_c$, A_{sl} is the cross section area of tensile reinforcement, b_w is the smallest width of the cross section, f_{ck} is the characteristics cylinder compressive strength of the concrete, $k_1 = 0.15$, and σ_{cp} is the shear strength of concrete. The shear contribution by mechanical shear connectors is given by [18]

$$V_s = \frac{n_0 F_t h_c}{S_s}, \tag{2.9}$$

where n_0 is the number of shear connectors either in top plate or in bottom plate across the width of the section, F_t is the tensile strength of the connectors, h_c is the depth of concrete core, and S_s is the spacing of the connectors.

2.3 Rigidity of SC beam

The deflection of SC beam caused by bending moments and shear force may be restricted for various reasons. If the height of the beam is not small compared to the length, shear force may give a significant contribution to deflection. Bond strength between steel plates and concrete core significantly influences the bending stiffness of SC beam. The total deflection of the beam δ_T consists of bending, shear and slip components i.e [22]

$$\delta_T = \delta_m + \delta_v + \delta_{SL}\,, \tag{2.10}$$

where δ_m is bending deflection, δ_v is shear deflection, and δ_{SL} is slip deflection defined according to Wright and Oduyemi's model [23] assuming zero slip at the top plate. The detailed formulae to calculate the slip deflection is given in Appendix IV. The bending deflection δ_m for a SC beam due to a point load F at a mid-span is [22][24]

$$\delta_m = \frac{FL^3}{6EI_{eq}}\left[\frac{3a}{4L} - \left(\frac{a}{L}\right)^3\right], \tag{2.11}$$

where L is the length of the beam, EI_{eq} is the bending rigidity, a is the distance of point load from the beam end. The shear deflection δ_v for a SC beam due to point load F at a mid-span is [22][25]

$$\delta_v = \frac{Fa}{2S}, \tag{2.12}$$

where S is the shear stiffness of the beam (Appendix IV) and a is the distance of point load from the end of the beam.

2.4 De-bonding resistance strength of SC beam

De-bonding is possible due to insufficient number of shear connectors. Hence, the total de-bonding resistance strength of the shear connectors is calculated on the basis of the number of studs and tie-bars between plates and concrete. The resistance of the connectors $P_{c,Rd}$ to the shear forces transferred by the steel plates is limited to 0.8 times the design shear resistance of the welded stud connectors P_{Rd} (when attached to compression plate) and 0.6 times the design shear resistance of the welded stud connectors P_{Rd} (when attached to tension plate). According to Eurocode 4, the equations to determine the design shear resistance of welded stud connectors is [26]

$$P_{Rd} = min\left(\frac{0.8\, f_u \pi\, d^2}{4\,\gamma_v}, \frac{0.29\,\alpha\, d^2\,(\sqrt{f_{ck}\, E_{cm}})}{\gamma_v}\right), \tag{2.13}$$

where f_u is the ultimate stress of the stud, d is the diameter of the shank of the studs, α is a factor (coefficient), f_{ck} is the characteristic compressive cylinder strength of concrete, E_{cm} is the elastic modulus of concrete, and γ_v is a safety factor ($\gamma_v = 1$). The coefficient α can be chosen as

$$\alpha = \begin{cases} 0.2\left(\frac{h_{sc}}{d} + 1\right) & \text{for } 3 \leq h_{stud}/d_{stud} \leq 4, \\ 1 & \text{for } h_{stud}/d_{stud} > 4, \end{cases} \tag{2.14}$$

where d_{stud} is the diameter of the studs and h_{stud} is the overall nominal height of the stud.

3 Failure modes of SC element

According to Oduyemi et al. [3], SC elements can fail under static loading due to at least one of the failure modes listed below.

a) Flexural failure
b) Shear failure
c) Horizontal slip failure

These failure modes observed experimentally are outcome of various local failure mechanisms. In flexural failure, yielding of steel plates and flexural cracks (smeared vertical hair cracks) in concrete core are the common failure mechanisms. Shear failure is characterised by diagonal shear cracks developed in concrete core from the bottom steel plate to the vicinity of applied load. Apart from these failure modes, end slip/ de-bonding between steel plates and concrete core may occur due to failure of shear connectors. The buckling of compression steel plate may also occur due to combined effects of normal stress and shear stress. Figure 6 illustrates schematically different failure mechanisms of the SC beam.

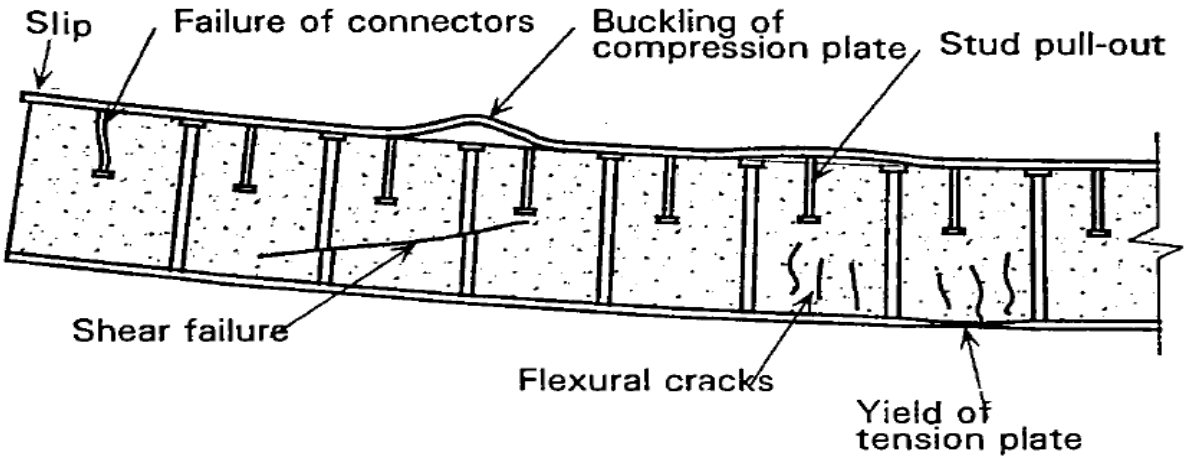

Figure 6: Typical failure mechanisms of SC element [3]

3.1 Flexural failure

Flexural failure is common failure mode in a 4-point bending test. Failure in SC beam is initiated by tension yielding of the steel plate followed the crushing of concrete in compression. For these failure mechanisms, the maximum compression strain in concrete needs to be smaller than the failure strain of steel plate (i.e. yield strain of steel). Positive bending moment produces compression stress above the neutral axis and tensile stress below the neutral axis (Figure 7(a)). As the steel plate at the top surface is subjected to high compression stress, buckling of compression steel plate may occur after yielding of tension steel plate.[3][9]

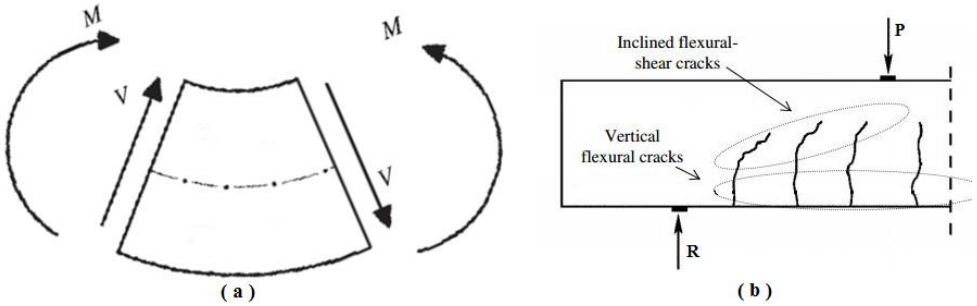

Figure 7: (a) Stress components in SC beam and (b) Concrete cracks during loading

Concrete is assumed not to take any tension but it is good at resisting compression. Therefore, smeared vertical hair cracks are developed in the concrete due to tension in the beginning of the deformation. When the deformation increases, the cracks gradually tend to incline and become flexural-shear cracks (Figure 7(b)).

3.2 Shear failure

Shear failure in SC beam occurs near a support where shear stress components are high. Although shear connectors play an important role to resist a sudden occurrence of shear failure, there is no fully convincing method for predicting the horizontal shear failure. Vertical shear failure has two principal failure mechanisms i.e. diagonal tension and diagonal compression. In the diagonal tension failure, an inclined shear crack is developed which split the beam into two pieces. Crushing of concrete occurs due to diagonal compression. [27] The

schematic representation of diagonal compression and diagonal tension vertical failure mode are shown in Figure 8 (b) and (c) respectively.

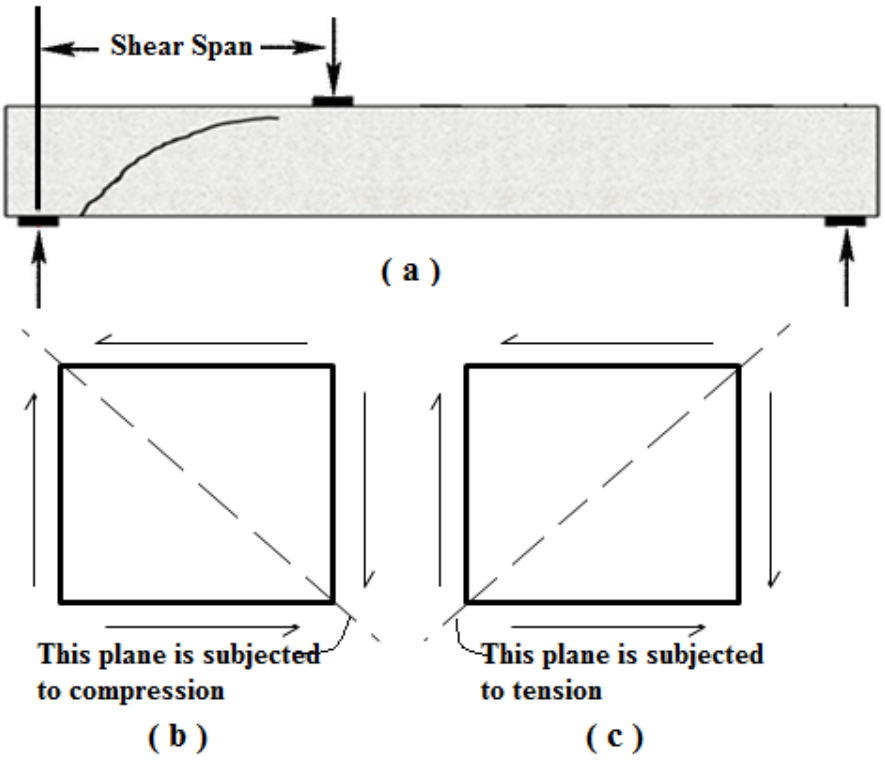

Figure 8: (a) Vertical shear failure (b) diagonal compression failure mechanisms (c) diagonal tension failure mechanisms

Vertical shear cracks shown in Figure 8(a) can be either web-shear cracks or flexural-shear cracks. Web shear cracks occur from an interior point of concrete core when the principle tensile stress components exceed the tensile strength of the concrete. Flexural-shear cracks occur after the inclination of flexural cracks. These cracks develop when the combined shear and tensile stress exceeds the tensile strength of the concrete. [27] After the failure of concrete core, a tie bar may yield due to stress concentrating in shear connectors.

3.3 De-bonding failure

De-bonding failure between steel parts and concrete of SC beam occurs in the high stress concentration regions, which are often associated with material discontinuities and presence of cracks. Propagation path of de-bonding depends on the elastic properties, strength of the

bond, substrate materials, and their interface fracture properties. De-bonding failure can occur due to flexure-shear crack, flexural crack, plate end shear failure, and shear failure. It has either plate-end de-bonding mode or intermediate crack induced de-bonding mode. A plate-end de-bonding initiates at the ends of the beam and propagates in the direction of increasing moment illustrated in Figure 9(a). An intermediate crack induced de-bonding initiates at flexural-shear crack region within the shear span and propagates towards the plate end in the direction of decreasing moment shown in Figure 9(b). De-bonding failure weakens the bonding strength between steel plate and concrete core and may produce an end slip. [3][28]

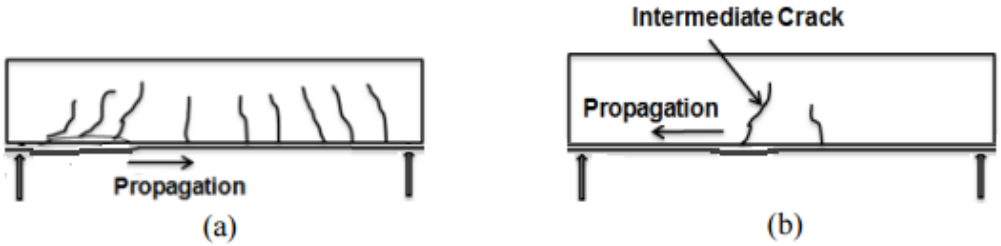

Figure 9: (a) Plate-end de-bonding (b) Intermediate crack induced de-bonding

4 SC beam model

This chapter describes the SC beam model, structural parts and their parameters, material models, and the contact model as well as the loading and boundary conditions. The geometrical parameters of rectangular SC beam shown in Figure 10 are length (L), width (W), height (H), shear tie distance (S_{tie}) in longitudinal direction, stud spacing in longitudinal direction (S_{stud_long}), and stud/ tie bar spacing in transversal direction (S_{stud_trans}).

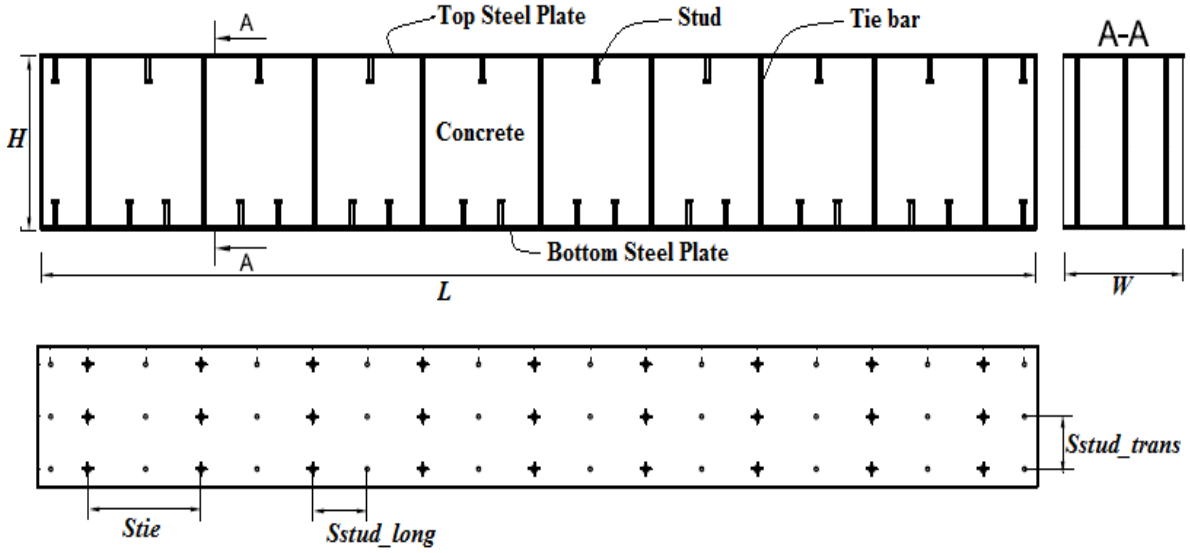

Figure 10: Front, side (section) and top projections of a SC beam

The structural parts of SC beam are core, top and bottom plate, tie bar, and stud (Figure 10). The core is made from concrete and it has length (same as beam's length), width (same as beam's width), and height (h_c) equals height of the beam minus total thickness of top and bottom steel plate as the geometric parameters. The geometric parameters of steel plate are length (same as beam's length), width (same as beam's width) and thickness (t_{sp}). The geometric parameters of a tie bar are diameter (d_{tie}) and length (L_{tie}) (same as the height of concrete core). Stud is the fourth structural part having diameter (d_{stud}) and length (L_{stud}) as the geometric parameters.

4.1 Material models

Bottom steel plate is made from structural steel S355 while top plate is made from either S355 steel or stainless steel. The quality of stainless steel is austenitic grade 1.4307. Shear bar is manufactured from either S355 steel or from Gr 8.8 steel. Studs are made from structural steel S235-J2G3+C450, a special grade used for NELSON stud. The concrete has nominal C30/37 grade. [17] All these materials are considered as isotropic. The stress strain relationship is given by [29]

$$\sigma = D^{el} : \varepsilon^{el}, \tag{4.1}$$

where D^{el} is the elasticity tensor which depends on Young's modulus E and Poisson's ratio v and ε^{el} denotes the elastic part of the strain which is assumed to be small. The material models of steel and concrete are described as follows.

4.1.1 Isotropic elasto-plasticity with hardening

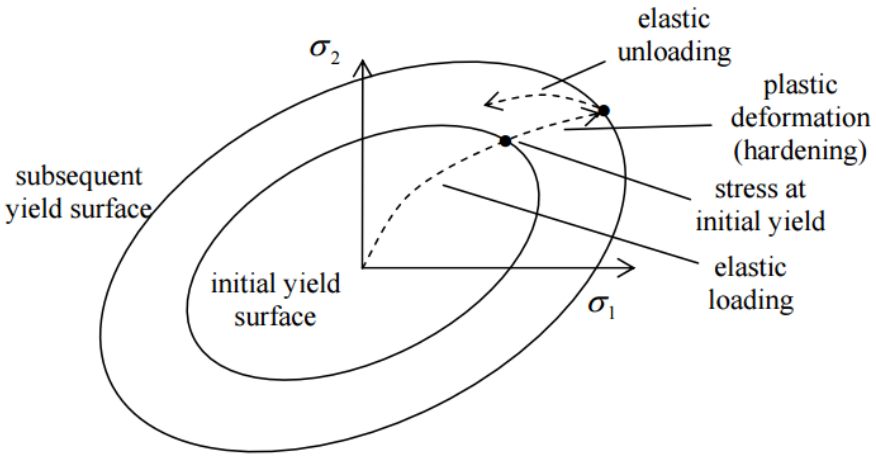

Figure 11: Isotropic hardening

Structural steel S355 exhibits an ideal stress-strain curve in which a plastic plateau is developed after yielding. The material behaves initially elastic (according to Eq. 4.1) followed by strain softening and then changes into plastic. The yield criterion of steel is based on von Mises stress measure whose yield surface is illustrated in Figure 11. The relation between stress σ and elastic strain ε^{el} by Hooke's law is [29]

$$\sigma = D^{el}: \varepsilon^{el} = D^{el}: (\varepsilon - \varepsilon^{pl}), \tag{4.2}$$

where ε is the total strain and ε^{pl} is the plastic strain. The yield function for isotropic hardening material is [29]

$$F(\sigma) = \sigma^0(\varepsilon^{pl}), \tag{4.3}$$

where σ^0 is the equivalent stress which is given by

$$\sigma^0 \dot{\varepsilon}^{pl} = \sigma: \dot{\varepsilon}^{pl}. \tag{4.4}$$

The plastic strain increment $d\varepsilon^{pl}$ according to the flow rule is given by [29]

$$d\varepsilon^{pl} = d\lambda \frac{dg}{d\sigma}, \tag{4.5}$$

where λ is non-negative plastic multiplier, and g is the plastic potential.

4.1.2 Ramberg-Osgood model

The stress-strain behaviour of stainless steel is different from that of S355. Strain hardening of stainless steel takes place at significantly higher ranges than low carbon steel without clear demarcation of the yielding point. The grade of stainless steel affects the degree of roundness of the stress strain curve, and austenitic grade exhibits the maximum non-linearity and strain hardening. Ramberg-Osgood model with Hill's modification illustrates the stress-strain relationship of stainless steel with minimum number of required parameters. According to this model, the offset yield stress of stainless steel is assumed to be 0.2% proof stress. Strain hardening behaviour of the steel depends on Ramberg-Osgood constant (*n*). When stress level is higher than 0.2% proof stress, plastic strain gradually becomes greater than the elastic strain. [30] In multiaxial case, the Ramberg-Osgood model is [29]

$$E\varepsilon = (1 + \upsilon)s - (1 - 2\upsilon)pI + \frac{3}{2}\alpha \left(\frac{q}{\sigma_0}\right)^{n-1} s, \tag{4.6}$$

where ε is strain tensor, E is Young's modulus, υ is Poisson's ratio, s is the stress deviator, p is the equivalent hydrostatic stress, I is the identity tensor, α is the yield offset, q is the Mises equivalent stress, and n is the hardening constant.

4.1.3 Damage plasticity model

Concrete contains a large number of micro cracks which are developed due to segregation, thermal expansion, shrinkage, or loading. Micro cracks affect considerably the mechanical behaviour during loading and contribute to generate the quasi-brittle behaviour of concrete. The nonlinear (quasi-brittle) behaviour of concrete can be analysed by smeared cracking approach or by damage plasticity approach [29]. The crack initiation process at any location occurs in smeared crack concrete approach when stress reaches one of the failure regions either in the biaxial tension region or in a combined tension-compression region. This approach is proposed for a relatively monotonic loading and for a material which exhibits either compressive crushing or tensile cracking. Cracking is assumed to be the most important aspect of this approach and the representation of cracking and post-cracking anisotropic behaviour dominates the analysis. Plastic straining in compression is controlled by a compression yield surface. [29]

Concrete damage plasticity approach is a modification of the Drucker–Prager strength hypothesis developed by Lubliner et al., 1989 and elaborated by Lee & Fenves, 1998 [29]. It describes the complex nonlinear behaviour of concrete. This model provides general capability for an analysis of concrete structure under different loading condition which is characterised by a yield criterion, flow rule, and a hardening/softening function [31][32]. Initially, stiffness degradation of concrete is isotropic and it is defined by damage variables. Strain rate decomposition is given by [29]

$$\dot{\varepsilon} = \dot{\varepsilon}^{el} + \dot{\varepsilon}^{pl}, \tag{4.7}$$

where $\dot{\varepsilon}$ is the total strain rate, $\dot{\varepsilon}^{el}$ is the elastic strain rate , and $\dot{\varepsilon}^{pl}$ is the plastic strain rate. The stress strain relationship is [29][32]

$$\sigma = (1-d)D_0^{el}:(\varepsilon - \varepsilon^{pl}) = D^{el}:(\varepsilon - \varepsilon^{pl}), \tag{4.8}$$

where D_0^{el} is the initial (undamaged) elastic stiffness of the material, $D^{el} = (1-d)D_0^{el}$ is the degraded elastic stiffness, and d is the scalar stiffness degradation variable having the range from zero (undamaged material) to 1 (fully damaged material). The effective stress tensor $\bar{\sigma}$ is defined as [29][32]

$$\bar{\sigma} \stackrel{\text{def}}{=} D_0^{el} : (\varepsilon - \varepsilon^{pl}). \tag{4.9}$$

Cauchy stress tensor σ, effective stress tensor $\bar{\sigma}$, and the degradation variable d are related by [29][32]

$$\sigma = (1-d)\bar{\sigma}\,. \tag{4.10}$$

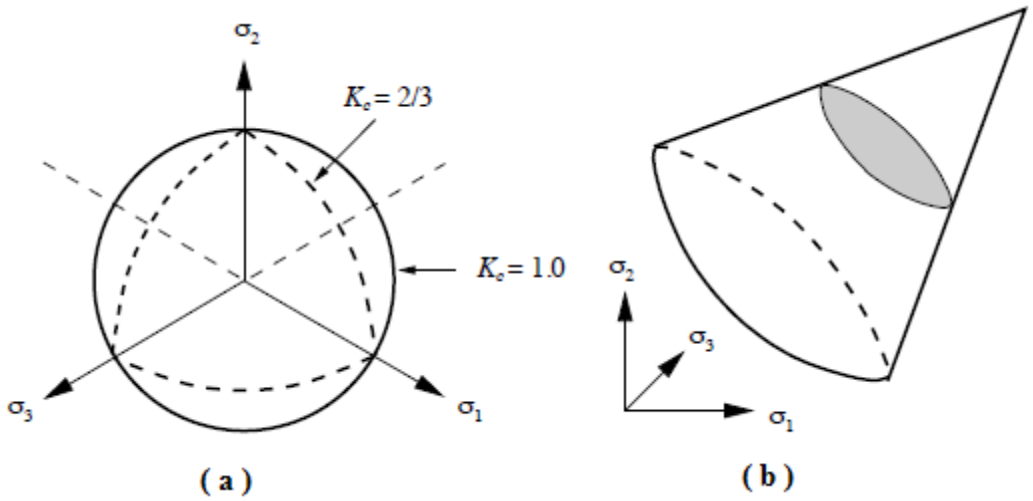

Figure 12: Yield surface in (a) deviatoric plane (b) three dimensions [33]

A yield surface is a surface in the stress space enclosing the volume of the elastic region. This means that the state of stress inside the surface is elastic, while stress states on the surface have reached the yield point. The yield criterion described by Lubliner et al. (1989) and modified by Lee and Fenves (1998) to account for different evolution of strength under tension and compression is given by [29][32]

$$F = \frac{1}{1-\alpha}(\bar{q} - 3\alpha\bar{p} + \beta\langle\bar{\sigma}_{max}\rangle - \gamma\langle-\bar{\sigma}_{max}\rangle) - \bar{\sigma}_c \leq 0, \tag{4.11}$$

where $\bar{p}$ is the effective hydrostatic pressure, $\bar{q}$ is the von Mises stress measure, $\bar{\sigma}_{max}$ is the maximum eigenvalue of effective stress, ε^{pl} is the plastic strain, ε_c^{pl} is the plastic strain in compression, $\bar{\sigma}_c$ is the principal effective stress in compression, and α and γ are dimensionless material constants. A function β is given by

$$\beta = \frac{\overline{\sigma}_c}{\overline{\sigma}_t}(1-\alpha) - (1+\alpha), \tag{4.12}$$

where $\overline{\sigma}_c$ is the effective compressive cohesive stress and $\overline{\sigma}_t$ is the effective tensile cohesive stress. These material constants mainly depend upon ratio of the strength in the biaxial state to the strength in the uniaxial state (f_{b0} / f_{c0}) and ratio of the distances between the hydrostatic axis and respectively the compression meridian and the tension meridian in the deviatoric cross section (K_c). The flow rule for damage-plasticity model is given by [29]

$$\dot{\varepsilon}^{pl} = \dot{\lambda}\frac{dG(\bar{\sigma})}{d\bar{\sigma}}, \tag{4.13}$$

where λ is non-negative plastic multiplier, and G is the flow potential. The flow potential is the Drucker-Prager hyperbolic function and it is given by [29][32]

$$G = \sqrt{(\epsilon\sigma_{t0}\tan\psi)^2 + \bar{q}^2} - \bar{p}\tan\psi, \tag{4.14}$$

where ψ is the dilatation angle, σ_{t0} is the uniaxial tensile stress at failure, ϵ is the eccentricity that defines the rate at which the function approaches the asymptote.

Dilation angle is defined as the angle of inclination of the failure surface towards the hydrostatic axis. It is also described as concrete internal friction angle. The value of dilation angle is ranges from 36^0 to 40^0 for normal concrete C30/37. Eccentricity improves the hyperbolic form of plastic potential surface. It is calculated as the ratio of tensile strength to compressive strength. [32][33] The nature of stress-strain curve for uniaxial compression of concrete is illustrated in Figure 13(a).

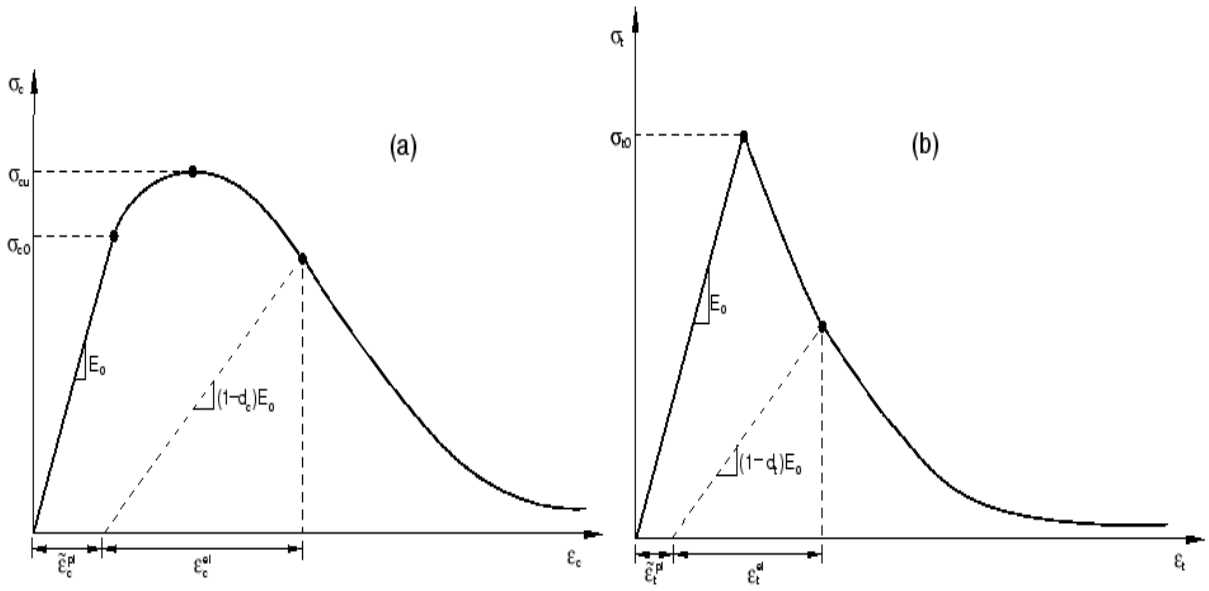

Figure 13: Stress-strain curve of concrete for uniaxial load in (a) compression (b) tension [29]

Uniaxial compression stress σ_c and the effective stress tensor $\bar{\sigma}_c$ are related by [29]

$$\sigma_c = (1 - d_c)\bar{\sigma}_c = (1 - d_c)E_0(\varepsilon_c - \hat{\varepsilon}_c^{pl}), \tag{4.15}$$

where d_c is the degradation variable in compression, E_0 is the initial modulus of elasticity of concrete, ε_c is the total compressive strain, $\hat{\varepsilon}_c^{pl}$ is the compressive plastic strain, $\hat{\varepsilon}_c^{el}$ is the compressive elastic strain, and σ_{cu} is the uniaxial ultimate compression stress.

The stress-strain relationship for uniaxial tension behaviour of concrete is illustrated in Figure 13(b). It is seldom determined through a direct tension test because of the difficulties involved in its execution and the large scatter of the results. Tension behaviour of concrete can be described on the basis of different ways. Wang and Hsu [34] defines tension stiffness behaviour of concrete on the basis of stress σ_t versus cracking strain $\hat{\varepsilon}_t^{ck}$. According to them, tension behaviour of concrete is given by

$$\sigma_t = \begin{cases} E_0\, \varepsilon_{tot} & \text{if } \varepsilon_{tot} \leq \hat{\varepsilon}_t^{ck} \\ f_{ctm}\left(\dfrac{\hat{\varepsilon}_t^{ck}}{\varepsilon_{tot}}\right)^{0.4} & \text{if } \varepsilon_{tot} > \hat{\varepsilon}_t^{ck}, \end{cases} \tag{4.16}$$

where σ_t is the tensile stress applied in concrete, E_0 is the modulus of elasticity of concrete, ε_{tot} is the total tensile strain of concrete, $\hat{\varepsilon}_t^{ck}$ is the cracking strain of concrete, and f_{ctm} is the mean concrete tensile strength.

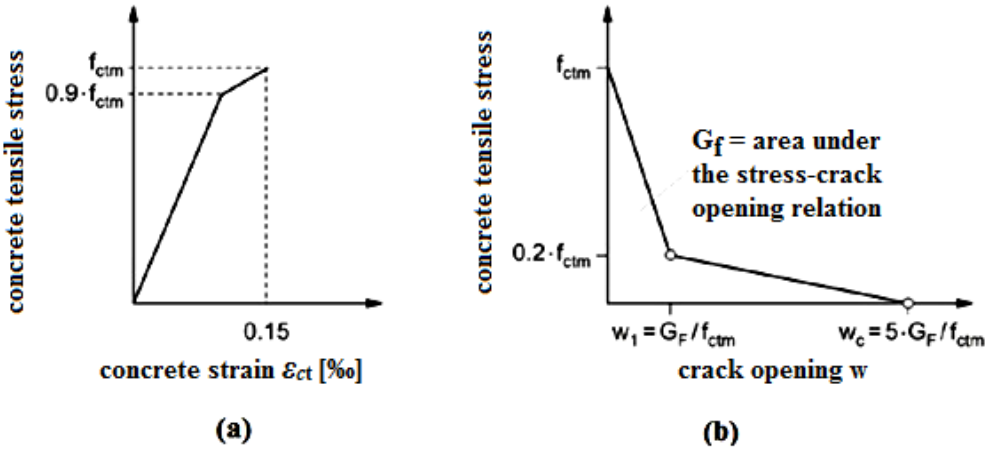

Figure 14: Uniaxial tension behaviour of concrete (a) pre-cracking stress-strain relationship (b) post-cracking stress-crack displacement relationship [35]

Tension stiffness can also be expressed in terms of fracture energy (G_f) cracking criterion based on Hillerborg's (1976) fracture energy proposal [29]. Tension behaviour of concrete based on this proposal is illustrated in Figure 14(a) and (b). The equation for the tensile stress-crack opening relationship of concrete is [35]

$$\sigma_{ct} = \begin{cases} f_{ctm}\left(1.0 - 0.8\,\dfrac{w}{w_1}\right) & \text{for } w \le w_1 \\ f_{ctm}\left(0.25 - 0.05\,\dfrac{w}{w_1}\right) & \text{for } w_1 < w \le w_c\,, \end{cases} \tag{4.17}$$

where σ_{ct} is the uniaxial tensile stress in concrete, f_{ctm} is the mean value of axial tensile strength of concrete in MPa, w is the crack opening in mm, $w_1 = G_F/f_{ctm}$ in mm when $\sigma_{ct} = 0.20\,f_{ctm}$, $w_c = 5\,G_F/f_{ctm}$ in mm when $\sigma_{ct} = 0$, and G_F is the fracture energy in N/mm.

Concrete degradation variable d defines the damage of concrete in SC beam ranging from zero (undamaged material) to one (fully damage material). Damage associated with the failure modes of the concrete (cracking and crushing) results in a reduction in the elastic stiffness. The stiffness degradation is isotropic in nature. The degradation variables are computed by using the following expression as [29]

$$d = 1 - \frac{\sigma_{tk}}{\sigma_{tk.max}}, \tag{4.18}$$

where d is the damage variable, σ_{tk} is the true compression or tension stress, and $\sigma_{tk.max}$ is the maximum true compression or tension stress.

4.2 Interaction models of the structural parts

The composite action of concrete and steel in SC beam relies on the bond between these two materials. Part surfaces are not perfectly smooth and even highly polished surfaces possess some degree of roughness. Surface roughness has a significant effect on how loads are transmitted at the contact interfaces.[4] Structural parts of SC beam interact at their geometrical boundaries, referred to as mating faces. To model the behaviour of contact surfaces, it is important to model both the structural parts and their interactions with each other and their surroundings properly. Contact interactions of structural parts are defined by specifying surface pairings and self-contact surfaces. Contact interface mechanics of SC beam consists of two components: normal interaction and tangential interaction.[16]

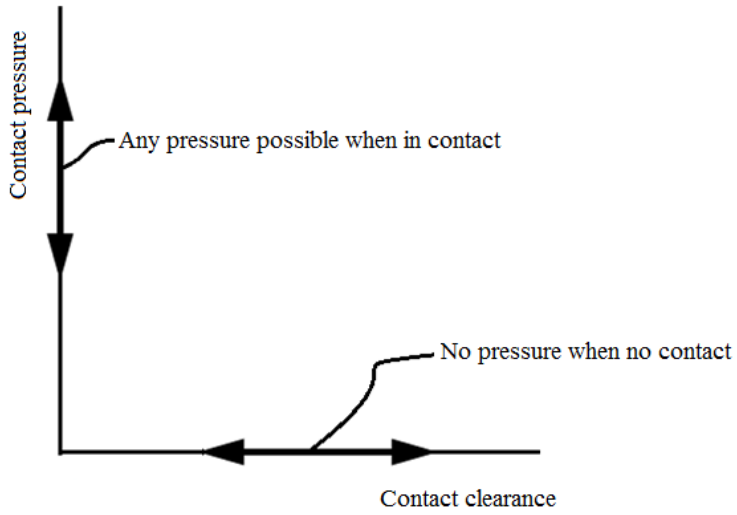

Figure 15: Contact pressure-clearance relationship

In normal interaction, contact pressure is acting perpendicular to the contacting surfaces. The relationship of contact pressure p and clearance h between two surfaces at a point illustrated

in Figure 15 can be described as $p = 0$ for $h < 0$ (open) and $h = 0$ for $p > 0$ (closed). The contact constraint can be enforced with a Lagrange multiplier representing the contact pressure in a mixed formulation. The change in contact pressure that occurs when a contact condition changes from "open" (a positive clearance) to "closed" (clearance equal to zero) is sudden. This model is known as "Hard contact" normal interaction model.[29]

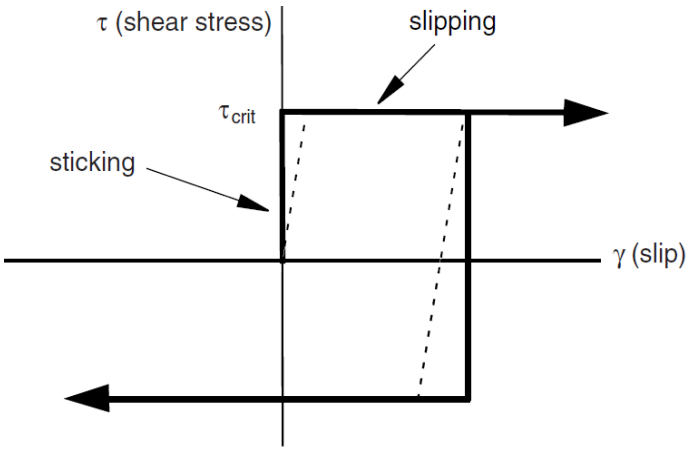

Figure 16: Coulomb friction model

Tangential behaviour of contact interface is associated with surface friction between contact parts. Coulomb friction model shown in Figure 16 can describe the interaction of contacting surfaces, which is based on classic laws of friction. The model is used for non-lubricated contacts as well as boundary- and mixed-lubricated contacts. Interacting surfaces allow separating but not permitting to penetrate each other. The tangential motion is zero until the surface traction reaches a critical shear stress value which depends on the normal contact pressure is given by [29]

$$\tau_{crit} = \mu p, \tag{4.19}$$

where μ is the friction coefficient and p is the normal contact pressure between the two surfaces. If the idle friction model does not model the slip conditions accurately, an allowable "elastic slip" shown by dotted line in Figure 16 may be introduced [29]. The "elastic slip" is the small amount of relative motion between the surfaces that occurs when the surfaces are sticking.

4.3 Loading and boundary conditions

The 4-point bending test is performed with the intention of obtaining flexural failure. In this test, there are 2 loading points and 2 supports. The 3-point bending test is carried out with the intention to obtain a shear failure. For this test, there is one loading point and 2 supports. The schematic representation of 4-point bending test and 3-point bending test are shown in Figure 17 and Figure 18 respectively. The parameters of load and support conditions are loading distance from left end (L_L), support distance from the end (L_S), and distance between the two loading points (L_M).

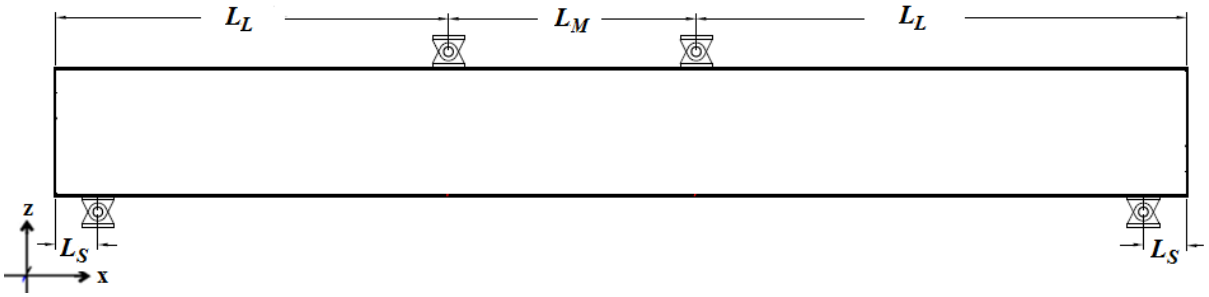

Figure 17: Load and support arrangement of a 4-point bending test

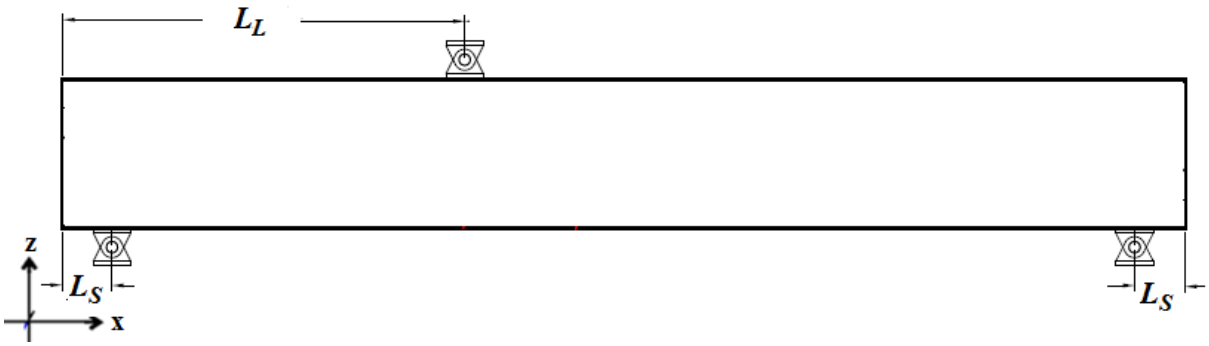

Figure 18: Load and support arrangement of a 3-point bending test

4.4 SC beam specimens

Six differently configured SC beams are used to study failure modes. The varied geometric parameters among the beam specimens include thickness of steel plates, tie bar diameters, shear reinforcement ratios, and overall dimensions. Table 1 shows the dimensions of SC beam specimens.

Table 1: Dimensions of SC beams [17]

Specimens	Length (L), m	Height (H), mm	Width (W), mm	Shear tie distance (S_{tie}) mm	Stud spacing in longitudinal (S_{stud_long}) and transversal (S_{stud_trans}) directions (mm/mm)	
					Top	Bottom
S1	9.54	800	640	600	300/240	200/240
S2	9.54	800	640	600	300/240	200/240
S3	8.34	800	800	600	200/160	200/160
S4	8.34	800	800	600	200/160	200/160
S5	8.34	800	800	1000	250/160	200/160
S6	8.34	800	800	600	200/160	200/160

The front view and side view of specimens S1 and S2 with dimensions are shown in Figure 19(a) and (b) respectively. The ratio of distances between stud and thickness of compression steel plate is high i.e. S_{stud}/t_c equals 30 in these specimens. S1 and S2 are identical in geometrical parameters. Detail drawing with dimensions and section views of these specimens are given in Appendix I.

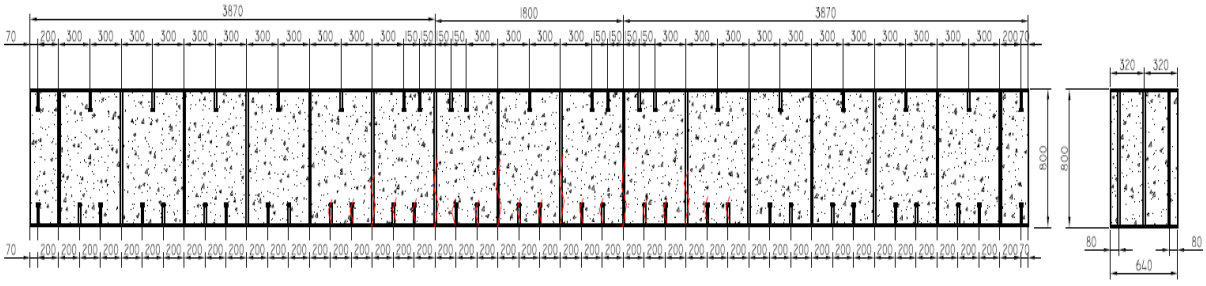

(a) (b)

Figure 19: Drawing of specimens S1 and S2 [4]

In Figure 20(a) and (b), the front view and side view of S3, S4 and S6 with dimensions are shown respectively. Shear reinforcements are conservatively spaced i.e. distances between tie bars equals to 600mm. The ratio of distances between tie bars and height of the SC beam is 0.75. This ratio satisfies the shear reinforcement distribution limit (maximum 0.75 times height of SC beams) according to EN 1992-1-1: Eurocode 2 (Clause 9.2.1 and Clause 9.2.2).

S3 and S4 have identical geometric parameters except the diameter of shear bar. S3 has tie bars while specimen S4 has threaded bars. There are differences of arrangement of tie bars and stud along transverse direction of S6 with respect to S3 and S4. Detail drawing with dimensions and section views of these specimens are also given in Appendix I.

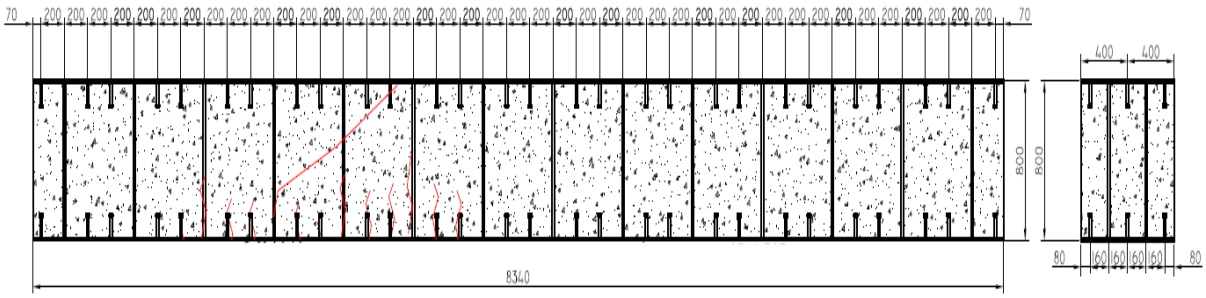

(a) (b)

Figure 20: Drawing of specimens S3, S4 and S6 [4]

Figure 21(a) and (b) illustrate the front view and side view of specimen S5. In this specimen, shear reinforcements are very rarely spaced i.e. distance between tie bars is 1000 mm. S5 has 0.064% minimum shear reinforcing ratio. Both shear reinforcement distribution limit (maximum 0.75 times height of SC beams) and the minimum shear reinforcing ratio (minimum 0.11%) according to EN 1992-1-1: Eurocode 2 (Clause 9.2.1 and Clause 9.2.2) are violated in this specimen. Detail drawing with dimensions and section views of this specimen are also given in Appendix I.

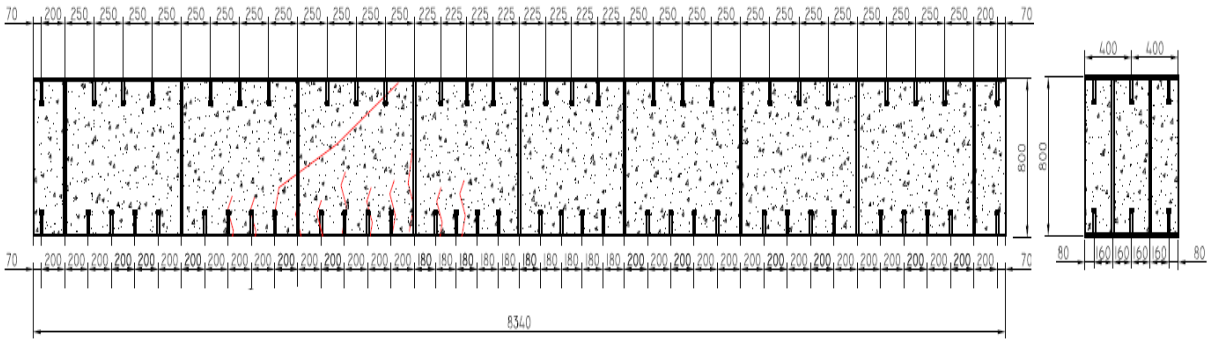

(a) (b)

Figure 21: Drawing of specimen S5 [4]

The major structural parts parameters of SC beam are thickness of steel plates, diameter of shear bar, stud length and stud diameter. These parameters are tabulated in Table 2.

Table 2: Parameters of structural parts of SC beam [17]

Specimens	Steel plate Thickness (t_{sp}) mm		Tie bar diameter (d_{tie}) mm	Stud diameter (d_{stud}) mm	Stud length (L_{stud}) mm
	Top	Bottom			
S1	10	15	24	19	125
S2	10	15	24	19	125
S3	15	15	18	19	125
S4	15	15	M16	19	125
S5	12	12	18	19	125
S6	12	12	18	19	125

The first two specimens (S1 and S2) are configured to a 4-point bending test and the remaining specimens (S3 –S6) are configured to a 3-point bending test. In Table 3, the dimension of supports and loading arrangement designed for the tests are listed. The rotation is restrained in the *y* and *z* direction and the translation in *z* direction. The distance of the supports from the end is 270mm in all specimens. Hydraulic actuators are used to apply the load incrementally during the test in vertical downward direction. The load cells are used to measure the applied load. Initially, the loading process starts with slow loading, complete unloading, and then the test is subjected to loading until up to the maximum displacement of the actuator. The distance of loading point from the end is 3870 mm in 4-point bending test and 3270 mm in 3-point bending tests.

Table 3: Position of supports and load during test [17]

Specimens	Total Bending points		Support distance from end (Ls), mm	Loading distance from left end (L_L), mm	Distance between two loads (L_M), mm
	No. of Supports	No. of loading			
S1 and S2	2	2	270	3870	1800
S3, S4, S5, and S6	2	1	270	3270	-

5 Abaqus Implementation

Finite element method (FEM) is a robust numerical technique to obtain approximate solutions of mathematical models. The domain is discretised into subdomains called elements, and the solution is sought in terms of discrete values of field variables. The advantages of discretising whole domain into subdomains include accurate representation of complex geometry and capture of local effects. The application areas of FEM ranges from stress analysis of solids to fluid dynamic problems, and from thermal problems to the analysis of electromagnetic phenomena. [16]

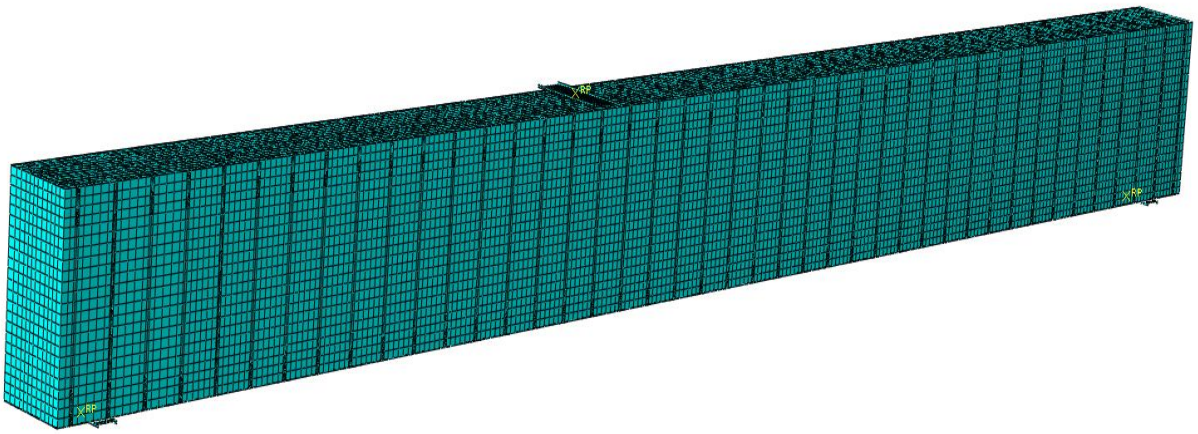

Figure 22: A finite element representation of SC beam

SC beams are characterised by quasi-brittle behaviour of material, multiple failure modes, and numerous surface to surface contacts. Consequently, structural analysis of SC beam requires non-linear analysis [16]. Commercial FE software Abaqus/Explicit is used for the non-linear quasi-static analysis. In Figure 22, a finite element model of SC beam created in Abaqus/CAE is illustrated.

A Plug-In named ‘SC Beam’ developed by Donnadieu [16] and further improved in this thesis is used to generate the FE model. It executes Python scripts as well as GUI toolkit, and provides general user interface to create a customized FE model [29]. As a benefit, the modelling cost and time is reduced significantly. All the data needed for the plug-in are input in SI units. [29] The geometry, material properties, loads and support arrangement, as well as

mesh and job properties can input through the Plug-In's user interface. The remaining properties of the model are constant therefore they are defined in python scripts.

5.1 Geometry

The geometry of the specimens listed in Table 1 and Table 2 are input in the user interface of the Plug-in illustrated in Figure 23.

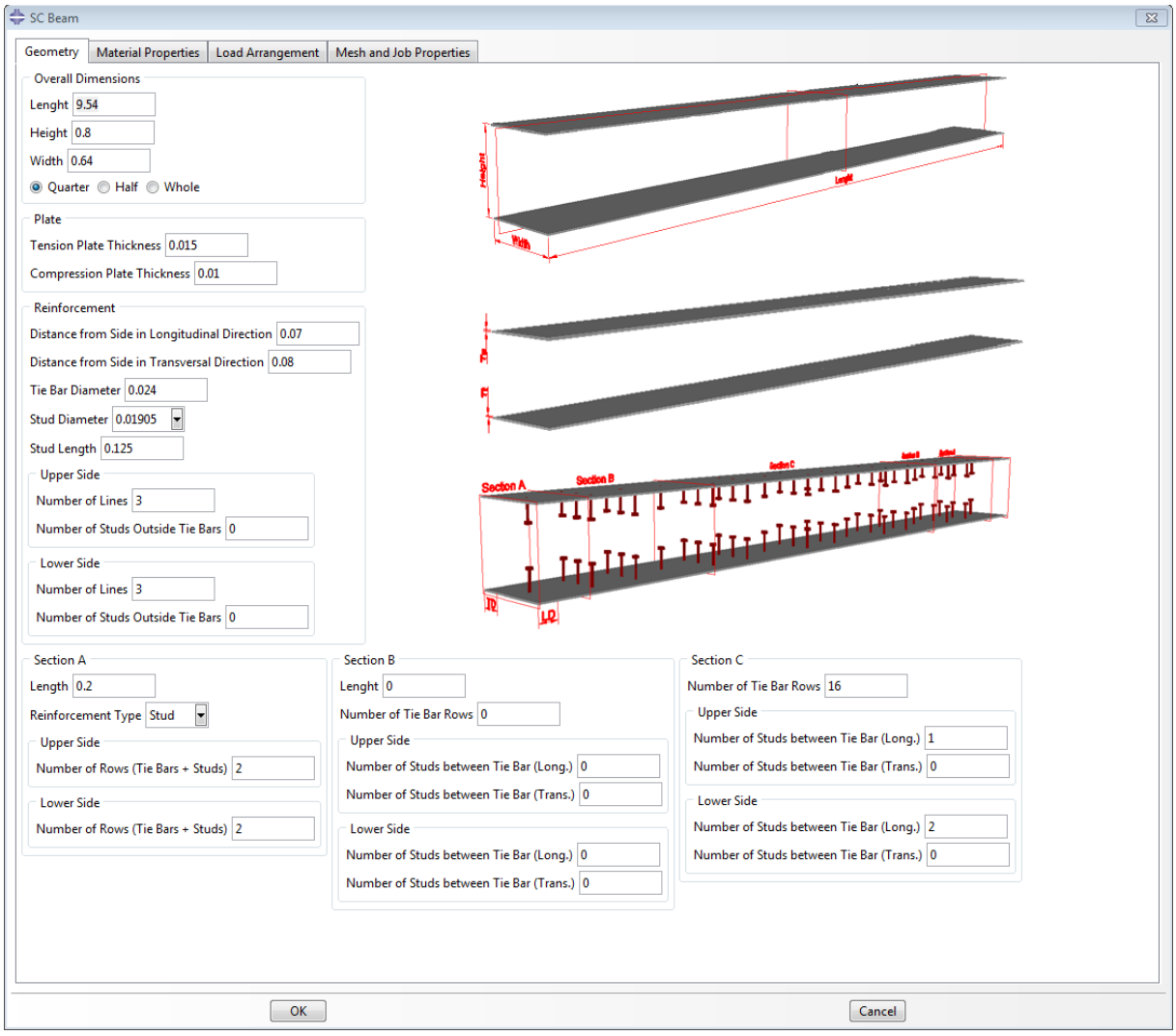

Figure 23: User interface of 'SC beam' Plug-In (geometry)

Mirror symmetry technique is opted to reduce the number of elements and degree of freedoms and thereby the computational works. This technique defines the symmetry about a particular plane or multiple planes in which geometry, loading conditions, supports, and material

properties are identical among sections. Single plane symmetry reduces a model into a half while double planes reduce a model into a quarter of the original size. [29]

Specimen S1 and S2 are symmetric in both longitudinal and transverse planes. In addition, support and loading conditions are also symmetric with respect to these planes. Hence, the model of theses specimens is quarter of the original size. A quarter size model is illustrated in Figure 24.

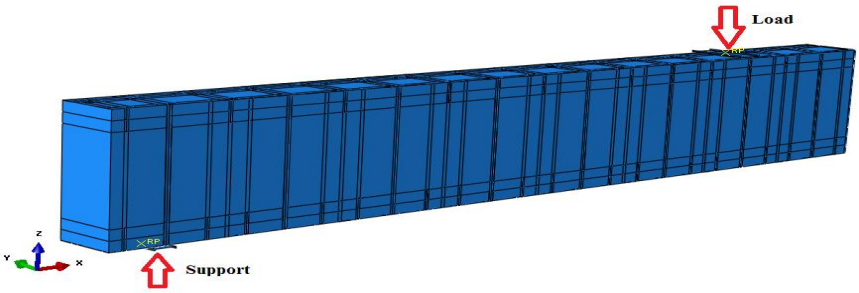

Figure 24: A quarter size model of SC beam

Geometries and supports of specimen S3, S4, S5, and S6 are symmetric with respect to the longitudinal and transverse planes. However, the loading condition is only symmetric with respect to the longitudinal plane. Therefore, the model of these specimens is half of the original size. In Figure 25, a half size model is shown.

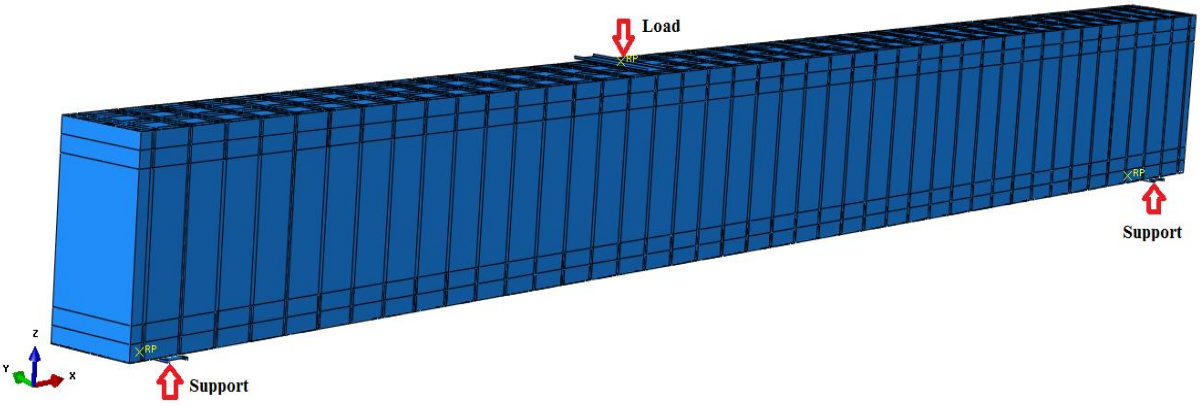

Figure 25: A half size model of SC beam

The structural parts of SC beam are modelled by using pre-defined element in library of Abaqus/Explicit FE software. Each element is characterized by attributes such as family, number of nodes, integration method, formulation, and degree of freedoms (DOFs). Concrete,

stud, and tie bar are modelled using continuum solid element C3D8R. Steel plate is modelled by using shell element S4R. Supports as well as load are modelled by using rigid element R3D4.[29]

5.2 Material properties

The mechanical properties of steel include modulus of elasticity (E_s) 200 GPa, Poisson's ratio (υ) 0.3, and density (ϱ) 7850 kg/m^3. In addition, the ultimate elongation of steel is taken to be at least 15%. Similarly, the mechanical properties of concrete include modulus of elasticity (E_{cm}) 33 GPa, Poisson's ratio (υ) 0.2, density (ϱ) 2400 kg/m^3, and strain at peak compression stress (ε_{c1}) 2.2‰. Material properties of structural parts of SC beam are tabulated in Table 4. The mean value of five samples for each specimen tested in the VTT lab is presented in the table. Mean value of concrete cylinder compressive strength (f_{cm}) and mean value of axial tensile strength of concrete (f_{ctm}) are estimated based on characteristic compressive cube strength of concrete ($f_{ck,cube}$) determined from the experiment.

Table 4: Material properties of structural parts of SC beam

Specimens	Bottom Plate			Top Plate			Tie Bar		Stud		Concrete		
	Yield stress (MPa)	Ultimate stress (MPa)	Ultimate strain (%)	Yield stress (MPa)	Ultimate stress (MPa)	Ultimate strain (%)	Yield stress (MPa)	Ultimate stress (MPa)	Yield stress (MPa)	Ultimate stress (MPa)	$f_{ck,cube}$ (MPa)	f_{cm} (MPa)	f_{ctm} (MPa)
S1	396	550	26	376	531	26	386	541	399	499	37.3	37.9	2.9
S2				309	610	58					36.7	37.5	2.9
S3				396	550	26	624	673			38.1	38.5	2.9
S4							932	1026			43.6	42.7	3.2
S5	429	557	24	429	557	24	624	673			39.5	38.6	3.0
S6											37.7	38.2	2.9

These material properties are input in the user interface of the Plug-in illustrated in Figure 26.

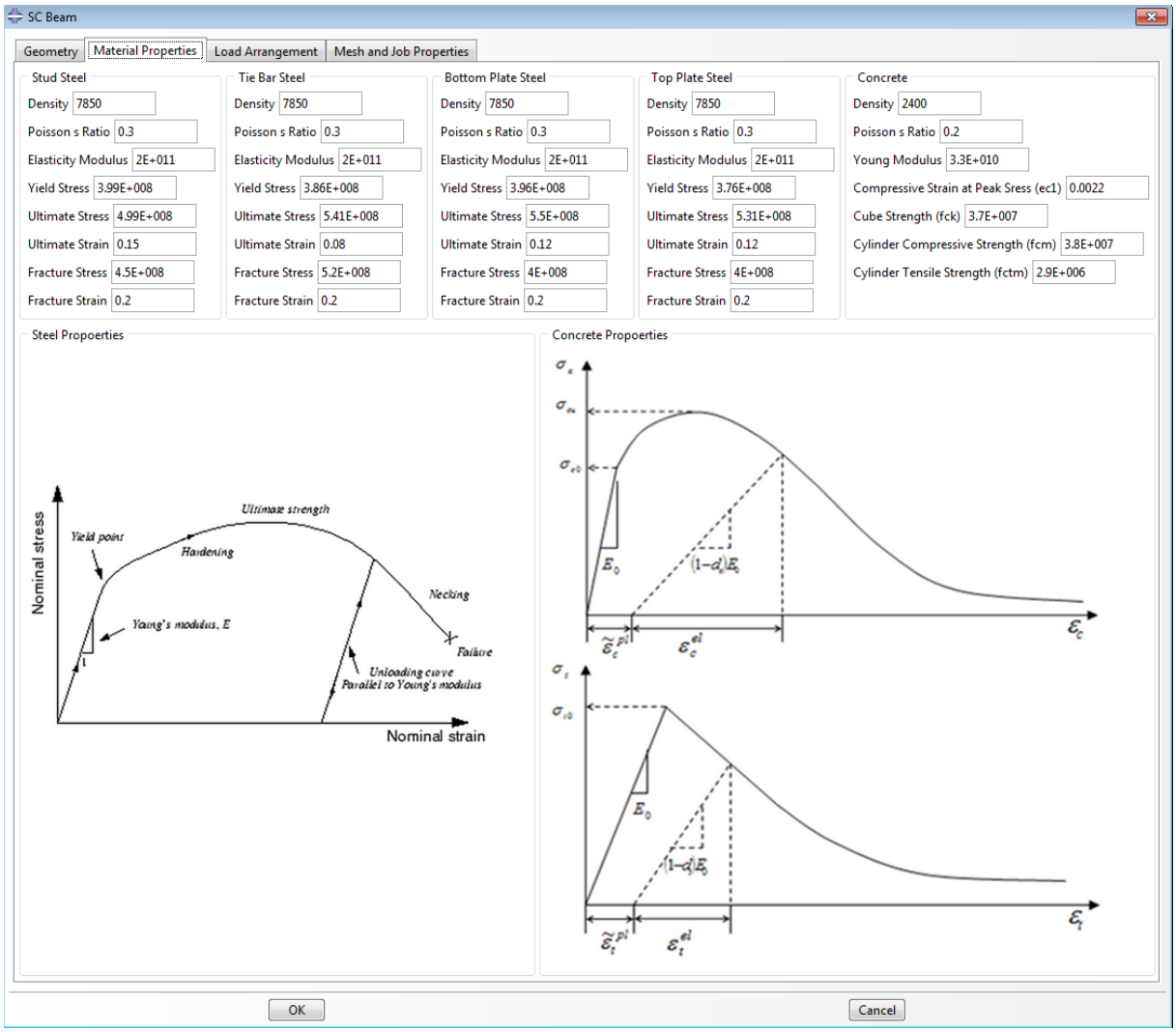

Figure 26: User interface of ‘SC beam’ Plug-In (material properties)

Structural steel S355 is modelled as elasto-plastic material with isotropic hardening behaviour. The characteristic stress strain relation (uniaxial) for structural steel S355 is illustrated in Figure 27. There are some variations in material properties of NELSON studs (manufactured from S235-J2G3+C450 steel) and tie bars (manufactured from S355 steel or Gr 8.8 steel) compared to steel plates. However, material properties of these structural parts of SC beam are also modelled according to isotropic elasto-plastic strain hardening model.

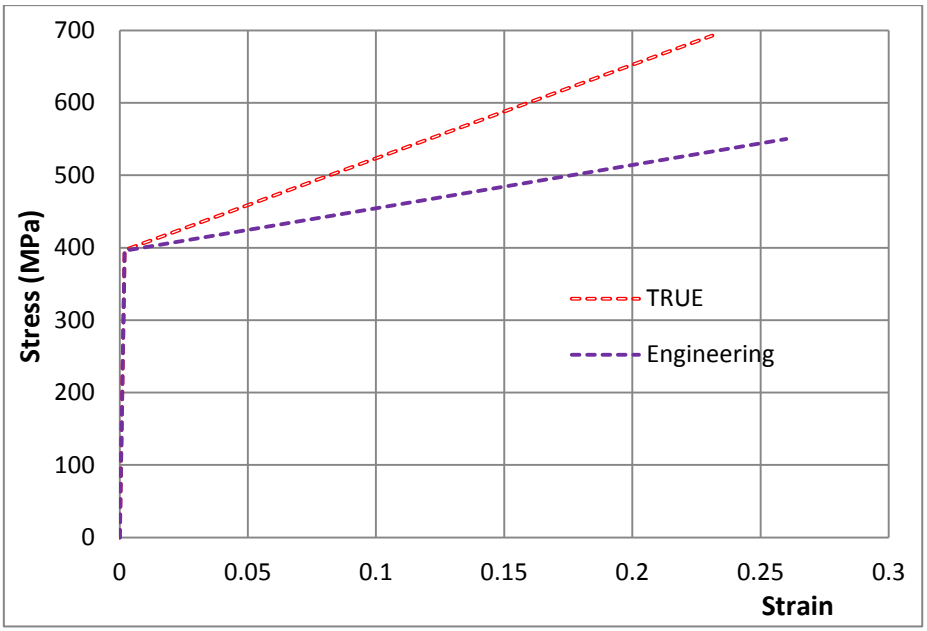

Figure 27: Characteristic stress strain relation for isotropic hardening material

Although stainless steel is also modelled as elasto-plastic material with isotropic hardening model, the stress-strain behaviour of stainless steel is different from that of structural steel S355. Therefore, the material behaviour of stainless steel is based on Ramberg-Osgood model modified by Hill. The stress strain relation (uniaxial) of stainless steel obtained according to Ramberg-Osgood model is shown in Figure 28.

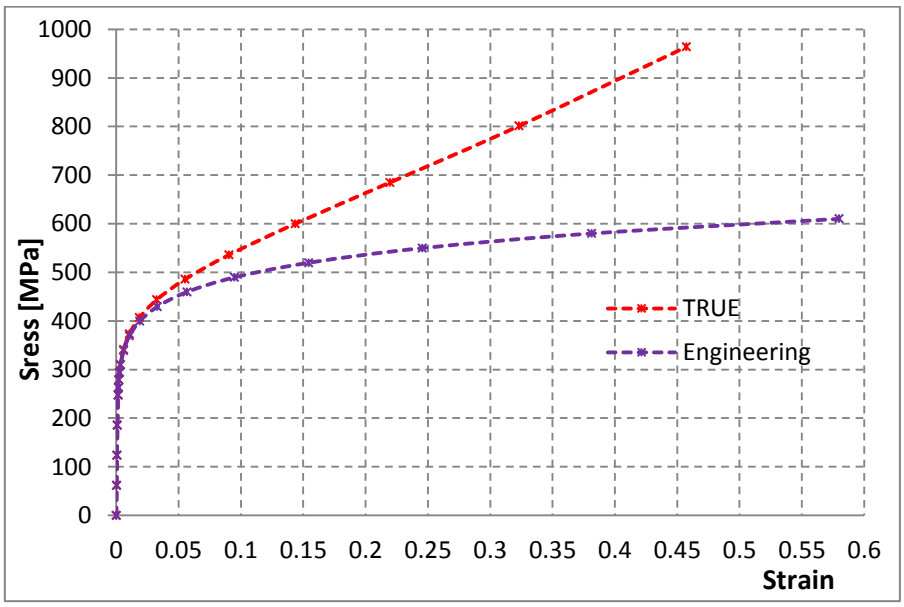

Figure 28: Characteristic stress strain relation for the austenitic grade 1.4307

In concrete damage plasticity (CDP) model, dilation angle, eccentricity, ratio of the biaxial stress f_{b0} to the uniaxial stress f_{c0}, deviatoric factor K_c, and viscosity coefficient are collectively known as plasticity parameters which are listed in Table 5. These parameters are based on Abaqus manual [29], Jankowiak et al. (2005) [32], and Kmiecik et al. (2011) [33]. The magnitude of degradation variables of concrete is input ranging from zero (undamaged material) to one (fully damage material).

Table 5: Plasticity parameters used in concrete damage plasticity model

Dilation Angle	Eccentricity	f_{b0}/f_{c0}	K_c	Viscosity coefficient
40	0.1	1.16	0.6666	0

Eurocode 2 is opted to replicate the uniaxial compression behaviour of concrete illustrated in Figure 29 because it requires fewer parameters than other approaches. According to EN 1992-1-1: Eurocode 2 clause 3.1.4, elastic modulus of concrete at the origin (E_c) can be approximated as 1.05 times E_{cm}. This approximation does not create precisely the curve between elastic and plastic region. Hence, the elastic nature of concrete is used only between origin and the first increment corresponding to a very small compressive strain ε_c value 0.00005.

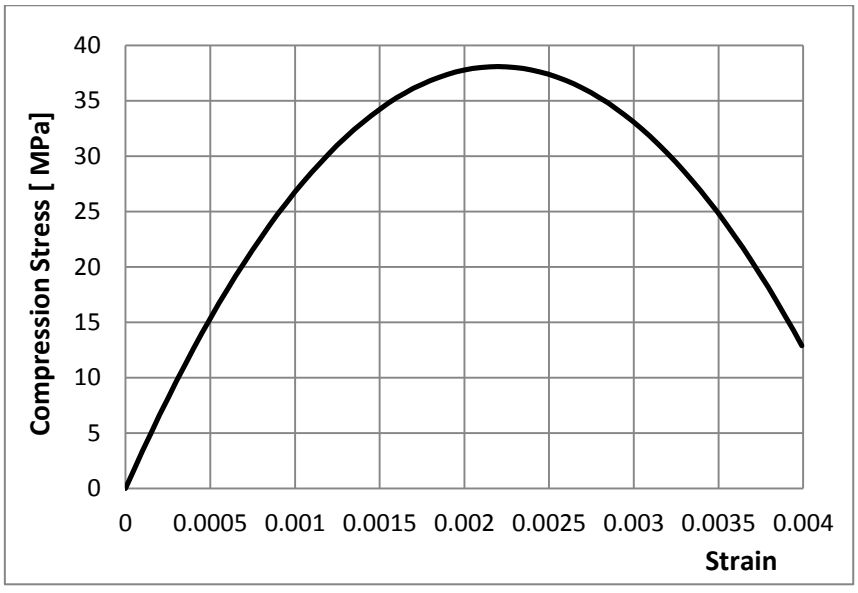

Figure 29: Stress-stain curve of concrete in uniaxial compression

The rest of the values of the compression curve are evaluated according to following equations. [18]

$$\sigma_c = f_{cm}\,\frac{k\eta - \eta^2}{1 + (k-2)\eta} \quad for\ \ 0 < |\varepsilon_c| < |\varepsilon_{cu1}|\,, \tag{5.1}$$

$$\eta\ = \frac{\varepsilon_c}{\varepsilon_{c1}}, \tag{5.2}$$

$$k = 1.05\,E_{cm}\,\frac{|\varepsilon_{c1}|}{f_{cm}}, \tag{5.3}$$

where σ_c is the uniaxial compressive stress in the concrete, f_{cm} is the mean value of concrete cylinder compressive strength, η is the ratio between compressive strain ε_c and compressive strain at peak strain ε_{c1}, ε_{cu1} is the crushing strain, and E_{cm} is the modulus of elasticity of concrete.

The uniaxial tension behaviour of concrete is based on fracture energy cracking criterion according to Hillerborg's (1976) fracture energy proposal [29]. Fracture energy (G_f) is defined as the energy required to propagate a tensile crack of concrete of unit area. It depends primarily on the water-cement ratio, the maximum aggregate size and the age of concrete for normal concrete C30/37. Fracture energy is determined according to International Federation of Structural Concrete (*fib*- Fédération internationale du béton) model code for concrete structures 2010 [35] and expressed as follow in equation (24).

$$G_f = 73\,f_{cm}^{0.18} \tag{5.4}$$

where G_f is fracture energy in N/m and f_{cm} is mean value of concrete cylinder compressive strength in MPa. According to above mentioned equation, the total fracture energy for normal concrete C30/37 with 38 MPa mean value of concrete cylinder compressive strength is 140.5 N/m. Based on this fracture energy, crack opening displacements at 20% and 1% of concrete tensile strength (σ_{ct}) are calculated. The crack opening displacement $w_1 = G_F/f_{ctm}$ when $\sigma_{ct} = 0.20\,f_{ctm}$ and crack opening displacement $w_c = 5\,G_F/f_{ctm}$ when $\sigma_{ct} = 0.01\,f_{ctm}$ where f_{ctm} is mean value of concrete cylinder tensile strength.

The uniaxial concrete tension curve according to fracture energy cracking criterion is illustrated in Figure 30. The crack opening displacement in *x*-axis versus concrete tensile stress in *y*-axis is plotted in this curve.

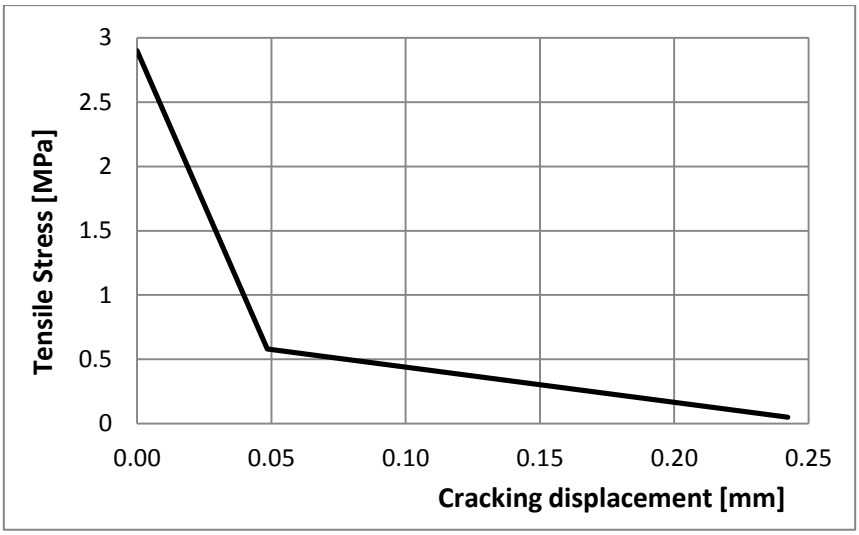

Figure 30: Stress-cracking displacement relationship of concrete in uniaxial tension

Initially, uniaxial tension behaviour of concrete was modelled according to Wang and Hsu approach [34]. The experimental tension cracks of concrete were not correctly replicated by this model (shown in Figure 31(a)). In the final model, the tension behaviour of concrete is modelled according to fracture energy cracking criterion [35]. This criterion was found to replicate the experimental behaviour better. The tension cracks obtained from finite element analysis according to fracture energy cracking criterion are shown in Figure 31(b).

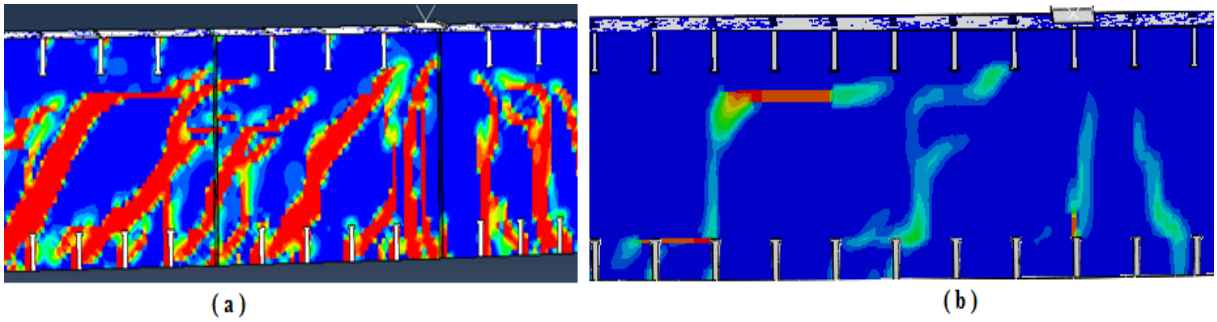

Figure 31: Tension cracks in concrete according to (a) Wang and Hsu model (b) Fracture energy criterion

5.3 Assembly and meshing

FE model of SC beam is generated by assembling different parts. The part instances of the model are steel plate, concrete, tie bar, stud, load, and support. The assembled model consists

of dependent part instances and has global co-ordinate system. Each instance is placed within the assembly by translation and/or rotation with respect to global origin.

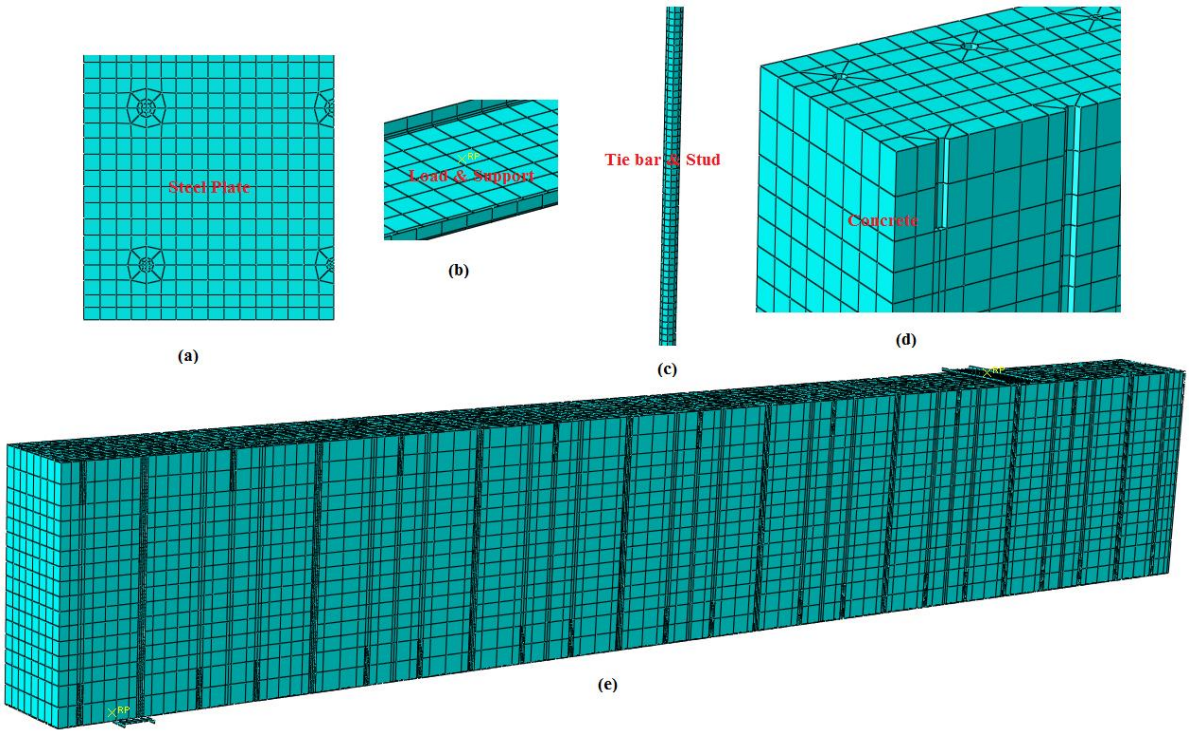

Figure 32: Mesh of FE model (for 4-point bending test)

Different seed size of mesh is selected for part instances in order to balance the computing accuracy and efficiency. The mesh of FE model designed for a flexural failure (first two specimens) including closed-up view of mesh of part instances is illustrated in Figure 32. For these models, plates and concrete instances have global seed size of mesh at least 2 times of the diameter of stud. Seed size of mesh in load and support instances is equivalent to diameter of stud while seed size of mesh in stud and tie bar is half of the diameter of stud. The mesh of FE model designed for a shear failure (remaining specimens) is illustrated in Figure 33. The global seed size of mesh in the plate instance is approximately 2 times the diameter of tie bar. The seed size in other part instances such as concrete, supports, and loading plate (rigid plate where load is applied) is approximately 1.5 times the diameter of tie bar. The seed size of mesh in part instances tie and stud is half of the diameter of tie bar. The mesh size of the curved elements is controlled by deviation factor set to 0.1. The deviation factor is a measure of how much the element edges deviate from the target geometry. The minimum size control of the mesh is the global seed size divided by 10.

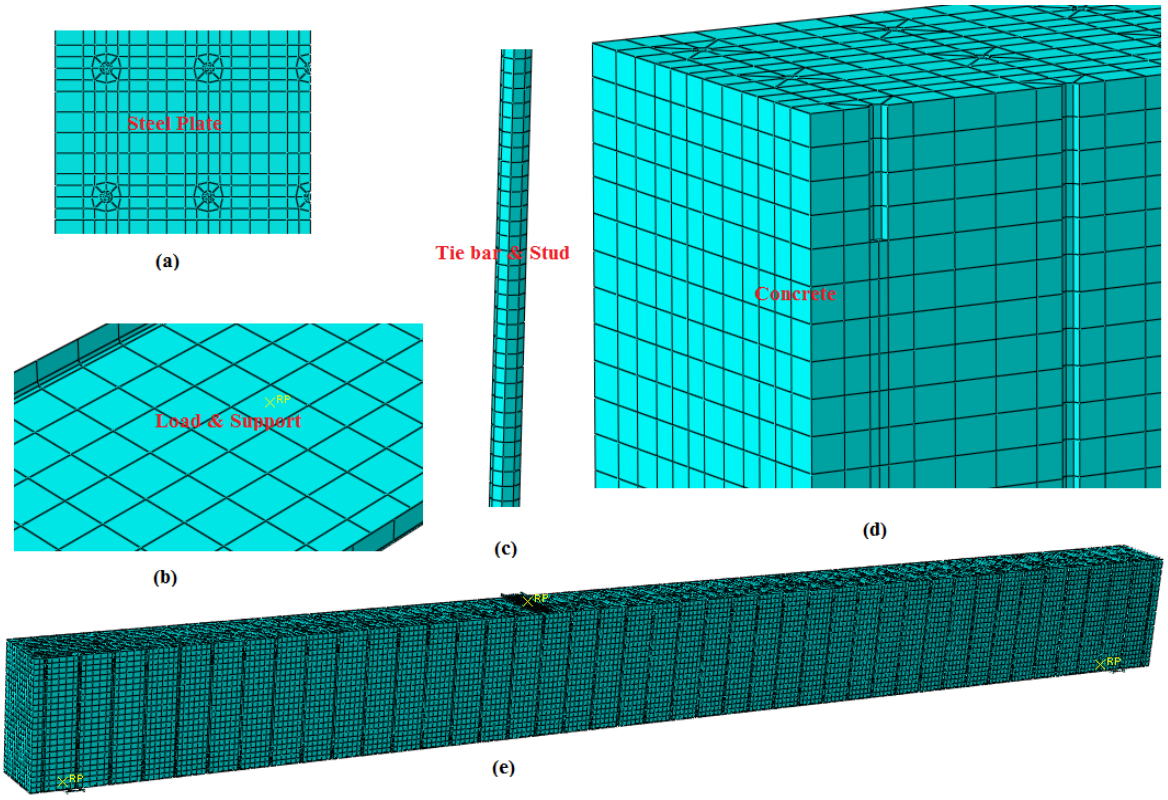

Figure 33: Mesh of FE model (for 3-point bending test)

5.4 Step, loading, constraint, and boundary condition

The step module includes defining the analysis steps, specifying output requests, and specifying analysis controls. The 'Initial' step is created by default and a dynamic/explicit step named 'Applied load' is created for the quasi-static analysis. Time period valued 10s, automatic time incrementation, and mass scaling for whole model with 0.0001 target time increment are the properties of 'Applied Load' step.

Supports are applied in the 'Initial' step with restrained rotation in the *y* and *z* direction and restrained translation in *z* direction which define the boundary conditions of the model. Based on the symmetry technique described in the beginning of this chapter, symmetries are created in the model. Both *x* and *y* symmetries are defined in the model of first two specimens while only *x* symmetry is defined the model of remaining specimens. Spatially distributed quantities such as stress, strain, displacement, reaction forces, and damage fracture properties are defined in field output request. Quantities that characterize the whole model or a region of the

model such as elastic strain energy, energy dissipated plastically etc. are defined in history output requests.

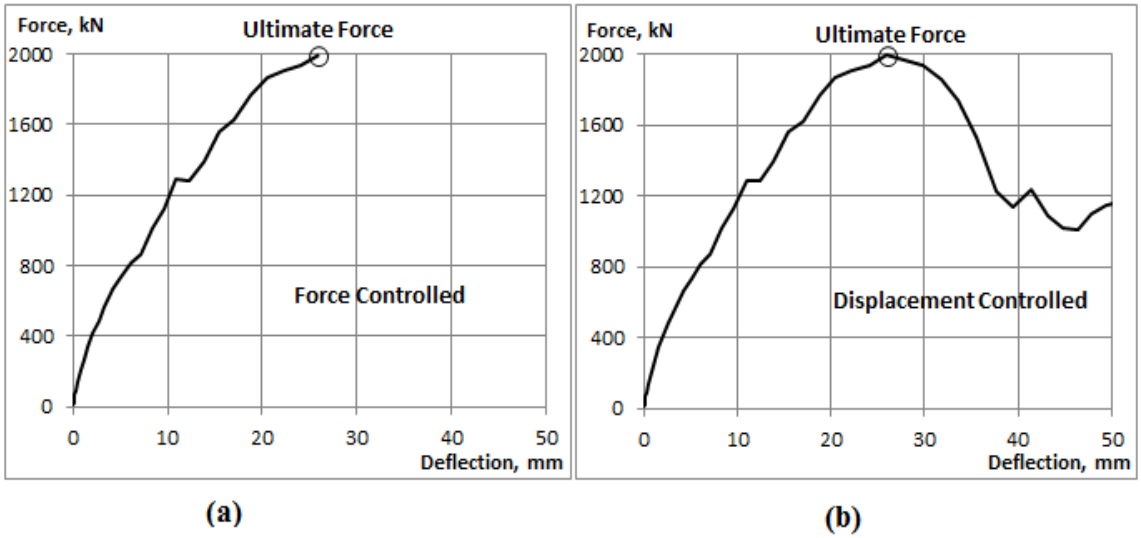

Figure 34: Schematic representation of force versus deflection curve with (a) force-control (b) displacement-control methods

Load can be applied by different methods such as force-control and displacement control. The schematic representation of force versus deflection curves based on force-control and displacement control methods are shown in Figure 34(a) and (b) respectively. As also the post-failure behaviour of SC beams is of interest, displacement-control method is selected to apply the load in FE analysis. In this method, an imposed displacement is defined in boundary conditions (BCs) type displacement/rotation. The displacement is applied in the negative *z*-direction with magnitude ranges from 0.005 m to 0.01 m depending on the type of bending test. A smooth amplitude step is created to apply the displacement load during displacement controlled loading.

The interaction at the interface between concrete and steel plate, loading cell and top steel face plate, bottom steel face plate and supports, as well as shear connectors and concrete core is simulated by the general contact with "hard formulation" in the normal direction and "penalty friction formulation" in the tangential direction. The hard formulation means that the contact pressure is transferred once two interaction surfaces are contacted whilst no contact pressure is transferred when they are separated. The penalty friction formulation permits relative slip between two interacting surfaces and the friction force between the surfaces is

proportional to the defined friction coefficient. This formulation allows separating interacting surfaces but not permits penetrating each other. Friction coefficient is set to 0.2 because it provides similar end slip of FE model compared to experiment. According to push-out tests, the shear stress limit is taken as 0.625 MPa and elastic slip stiffness is taken as 1222 N/m^3. It is also assumed that there is no tensile contact force between steel plate and concrete core. Tie constraint is created between inner surface of loading plate and outer surface of top steel plate, end surface of stud and inner surface of top / bottom steel plate, end surface of shear bars and inner surface of steel plates, headed surface of stud and adjacent concrete section, and inner surface of support plates and outer surface of bottom plate. A self-weight of SC beams is input with gravity load 9.81 m/s^2 in vertical downward (-*z*) direction in the model.

5.5 Post processing

After completing the pre-processing phase, the job is created and submitted for analysis. The results of the analysis are obtained in *.odb* file. The different model shapes such as undeformed, deformed, contours etc. and results information are obtained from output database using the visualization module. The quality of analysis results and the sources of convergence problems are obtained by using visual diagnostics tool. The field output requests or history outputs requests can be achieved in nodal point, in elements or in whole model based upon the specific output request. All of these requests can be plotted in Abaqus viewport using plotting tools, and data exported to Microsoft Excel using Excel utility option.

6 Results of the experiment

The results obtained from the 4-point bending test and the 3-point bending test of SC beam are summarised in this chapter. The results of the experiment for each SC specimen in terms of failure modes and the ultimate force are presented.

SC beam of 4-point bending test is shown in Figure 35. Arrows indicate the direction of applied loads and reaction forces. Yellow rectangle indicates the measurement region of expected bending failure under a constant bending moment. The top surface of the SC beam is under compression and bottom surface is under tension.

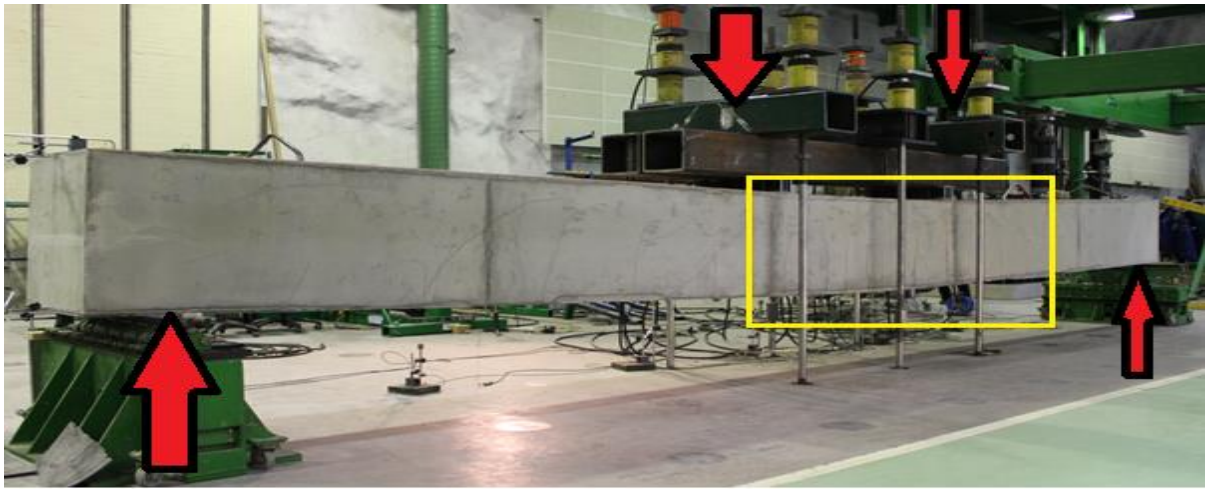

Figure 35: Bending test specimen illustrating applied loads (downward arrows), reaction forces (upward arrows), and measurement region (yellow rectangle) [17]

Specimens (S1 and S2) fail due to yielding of the tensile plate closely followed by buckling of the compression plate. The buckling failure of SC beam seems to be driven by the collapse of the compression zone of the beam followed by concrete crushing. In Figure 36, the buckled steel plate marked by red circle of specimen S1 is illustrated [17].

Figure 36: Buckled specimen S1 (a) full specimen (c) close-up view of buckling [17]

Shear failure seems more dangerous than a flexural failure and, therefore shear reinforcement is designed conservatively in specimens (S3 - S6). SC beam of a 3-point bending test is shown in Figure 37. Arrows indicate the direction of applied load and reaction forces. Yellow rectangle indicates the measurement region of expected shear failure.

Figure 37: Shear test specimen illustrating applied load (downward arrow), reaction forces (upward arrows), and measurement region (yellow rectangle) [17]

Concrete is stronger in compression than in tension. Therefore, the tendency of cracking development due to tension is faster than the crushing development due to compression. [8] Figure 38 shows the vertical shear cracks developed in specimen S3 during the test.

Figure 38: Vertical shear cracks developed in specimen S3 [17]

Table 6 summarizes the ultimate loads and failure modes of SC beams obtained from experiment. Specimen S1 and S2 fail due to yielding of the tensile plate closely followed by buckling of the compression plate while the other specimens fail due to vertical shear failure of concrete.

Table 6: Ultimate load and failure modes obtained from experiments [17]

Specimens	Ultimate load (kN)	Failure modes
S1	1528	Yielding of the tensile plate closely followed by buckling of the compression plate
S2	1690	Yielding of the tensile plate closely followed by buckling of the compression plate
S3	1932	Vertical shear failure
S4	1735	Vertical shear failure
S5	860	Vertical shear failure
S6	1334	Vertical shear failure

7 Validation of SC model

In this section, FE results are validated against experimental results. Models of S1–S6 are the replications of SC beam specimens S1–S6 respectively. The results obtained from FE analysis are presented for each model. The results include failure modes, ultimate force, mid-point deflection, end slips, and strains.

7.1 Model S1

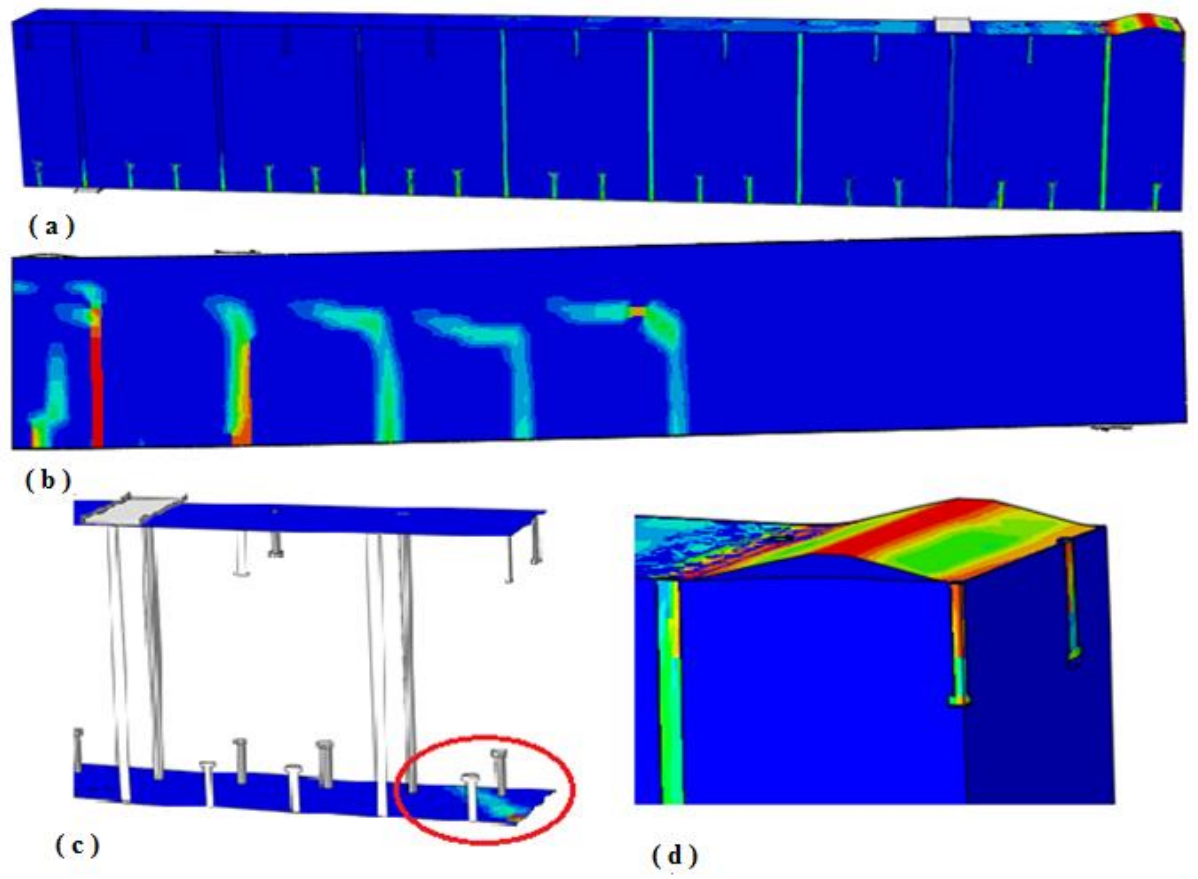

Figure 39: Failure mechanisms of model S1 (a) buckling (b) cracks in the outer face (mirror view) (c) bottom plate yielding (d) close-up view of buckling

Model S1 are in good agreement with the failure modes of specimen S1 observed during experiment. The tension (bottom) steel plate starts to yield (marked by red circle in Figure 39(c)) at force 1460 kN and 33 mm mid-point deflection. Simultaneously, the flexural cracks expand and shear cracks start to develop. The plasticity in the tension steel plate rapidly

increases beyond the ultimate force 1639 kN (57 mm deflection of model S1). At force 1610 kN and 84 mm deflection of the model, the buckling occurs at compression (upper) steel plate. After the bucking, the force bearing capacity of the model is reduces. The failure mechanisms of the model and specimen are yielding of the tensile plate closely followed by buckling of the compression plate at the ultimate force.

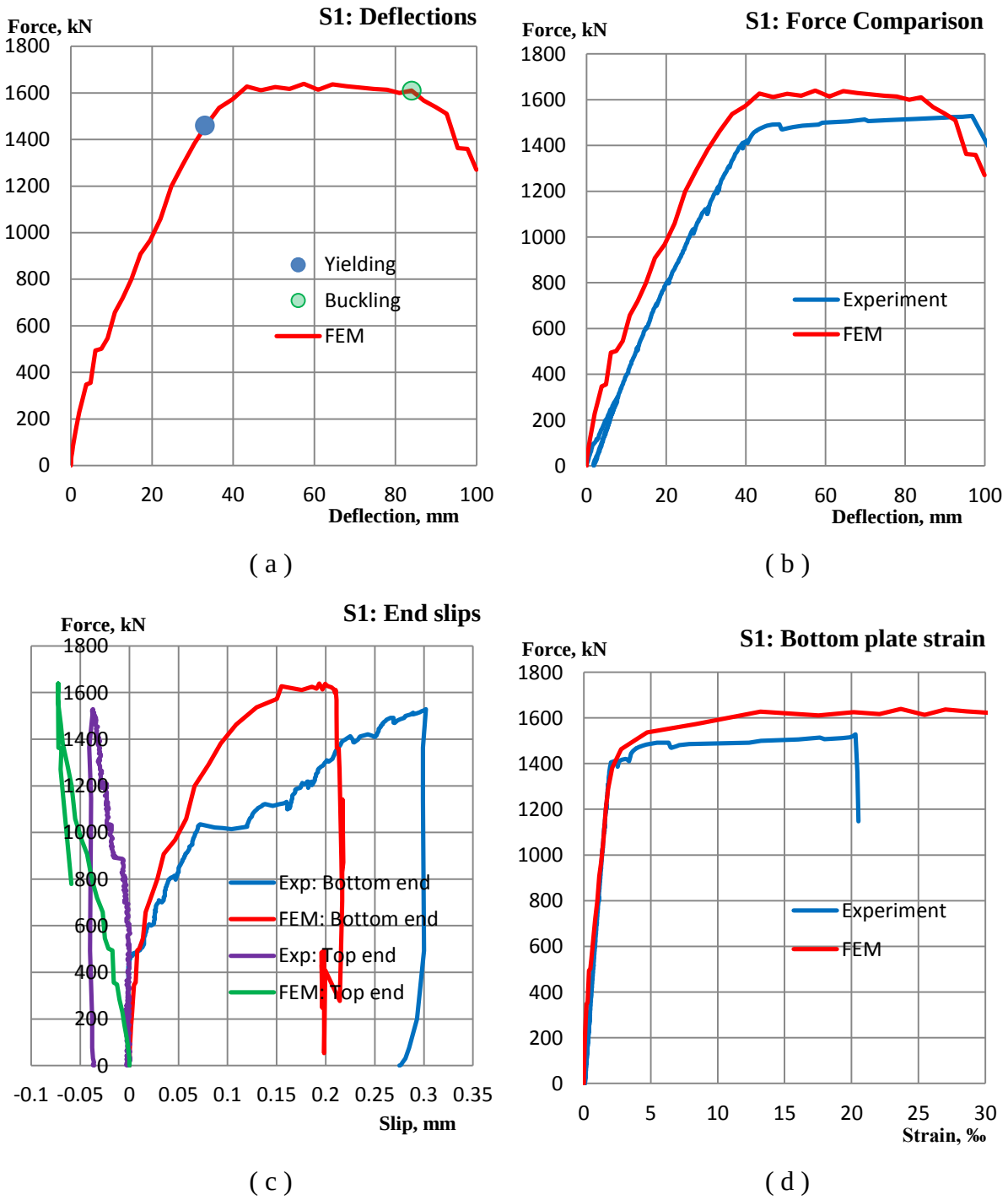

Figure 40: Results for model S1 (a) force versus displacement (b) comparison of force versus displacement (c) comparison of end slips (d) comparison of bottom plate strain

In Figure 40(a), the FE result of load versus deflection of model S1 is graphically represented. Force-displacement relationship is linear until force of 1500 kN and deflection 35 mm. Just before this force level (marked by blue dot in Figure 40(a)), yielding at the tension (bottom) steel plate occurs. The ultimate force of model S1 is 1639 kN at 57 mm deflection. Buckling at compression (top) plate occurs at 1610 kN with 84 mm deflection marked by green dot in this figure. Deflection of the model between yielding of the bottom plate and buckling at top plate is increased rapidly from 35 mm to 84 mm. While deflection of model S1 doubles, the magnitude of force is increased by around 100 kN (i.e. 9%) between these failure modes.

The force-displacement plot obtained by model and experiment are compared in Figure 40(b). The experiment data contains loading, unloading and reloading phases, and therefore there are discontinuities in the beginning of the graph. Compared to experiment, the result of model S1 appears to be little stiff. Force-displacement relationship is linear until the bottom plate yielding in model as well as in experiment. The rapid growth of deflection is observed between the yielding of tension steel plate and buckling of compression steel plate in both methods. The graph also reveals that the force level after buckling of compression steel plate is dramatically decreased in experiment as well as in model. In experiment, the ultimate force is 1528 kN while in model 1639 kN which is around 7% higher than the value of experiment.

Figure 40(c) compares slips between steel plate and concrete at the beam end. The bonding between bottom plate and concrete seems to be stronger in model than in experiment. While bonding between top plate and concrete seems to be just opposite. The maximum slip in the bottom end is 0.22 mm and in top end it is 0.06 mm in the model. In experiment, maximum bottom end slip is 0.3 mm and top end slip is 0.04 mm. Figure 40(d) illustrates strain in the bottom plate. Until 1400 kN, the tensile strain is linear. After that, strain grows rapidly until buckling of the compression steel plate in experiment as well as in model. There is 21‰ bottom strain in experiment and 27‰ bottom strain in model at the moment of buckling.

7.2 Model S2

The results obtained from FE analysis of model S2 are in agreement with the failure modes of specimen S2 observed during experiment. The tension (bottom) steel plate starts to yield at

force level 1460 kN with 33 mm deflection of the model (marked by red circle in Figure 41(c)). Instantaneously, the bending cracks expand and shear cracks start to develop in the model. The model carries ultimate force 1684 kN at 95 mm deflection of the mid-point. Beyond ultimate force, the top plate buckling occurs at force level 1520 kN and 106 mm mid-point deflection. After buckling, the load bearing capacity of the SC beam is deteriorated. The failure mechanisms of the model and specimen are yielding of the tensile plate closely followed by buckling of the compression plate at the ultimate force.

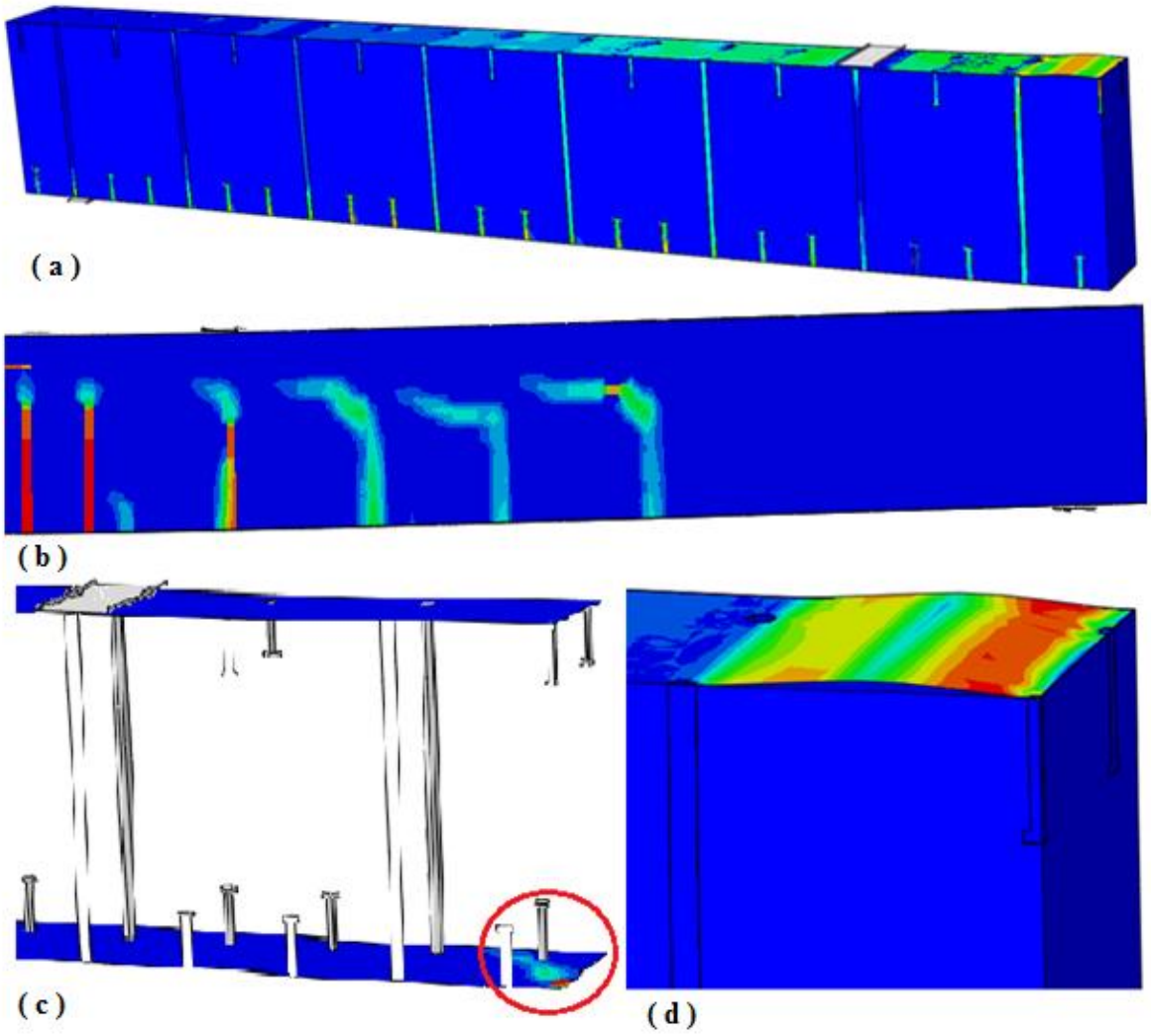

Figure 41: Failure mechanisms of model S2 (a) buckling (b) cracks in the outer face (mirror view) (c) bottom plate yielding (d) close-up view of buckling

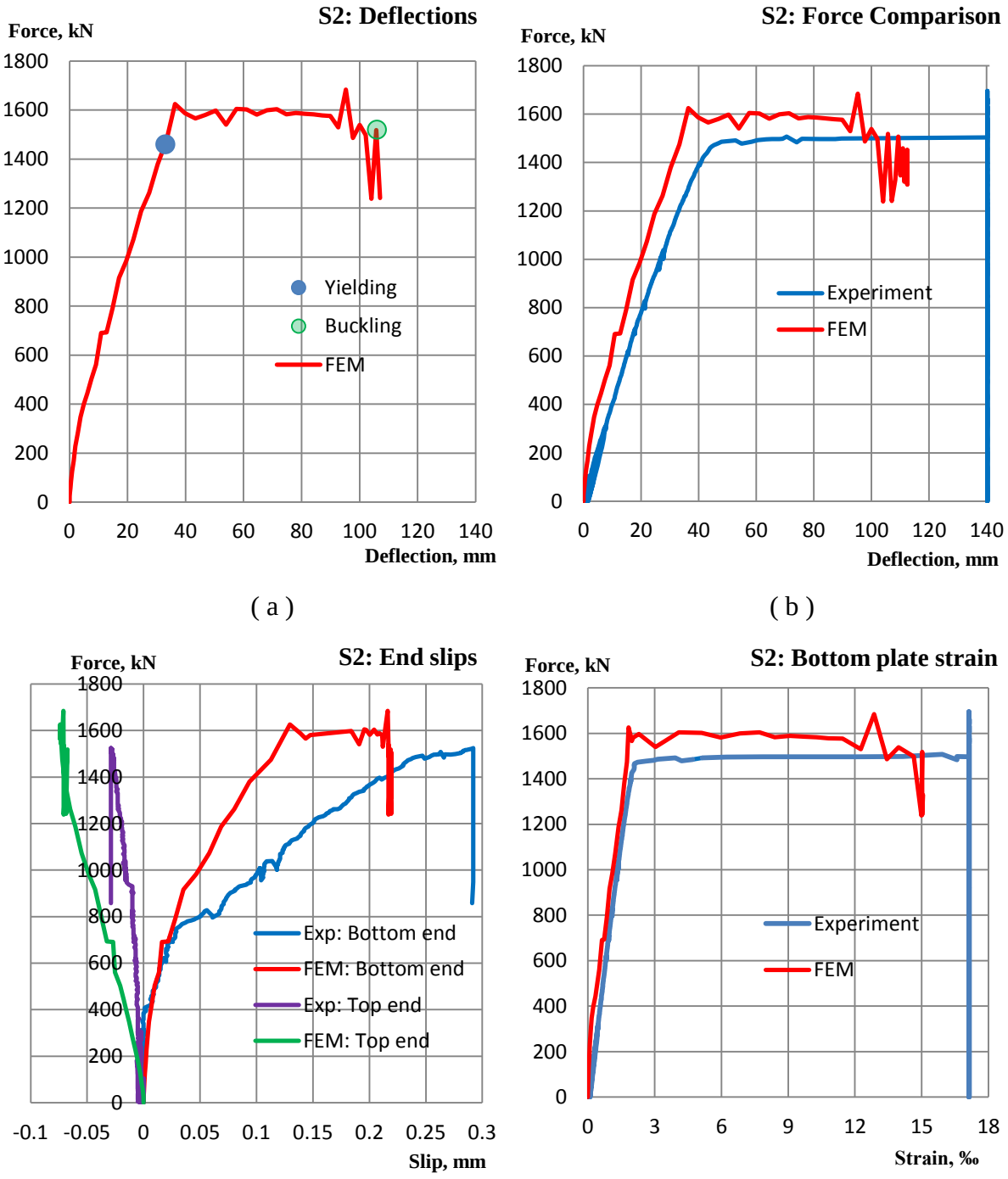

Figure 42: Results for model S2 (a) force versus displacement (b) comparison of force versus displacement (c) comparison of end slips (d) comparison of bottom plate strain

Figure 42(a) shows the force-displacement curve of model S2. Force-displacement relationship is linear until the force 1460 kN and deflection 33 mm. At this force level (marked by blue dot in Figure 42(a)), yielding at the tension (bottom) steel plate occurs. The ultimate force is 1684 kN at 95 mm deflection of the model. Buckling of compression (top)

steel plate occurs at force 1520 kN with 106 mm deflection illustrated in the Figure 42(a) by green dot. Also in this model, the deflection increases rapidly from 33 mm to 106 mm between failure modes i.e. yielding of the tension plate and buckling of the top plate. Although the magnitude of deflection increases more than three times between these failure modes, magnitude of force increases only about 200 kN (i.e. 14%).

Figure 42(b) compares force-displacement relationship. Likewise specimen S1, plot of specimen S2 has discontinuities because of loading, unloading and reloading phases of the experiment data. Model S2 also seems to be stiffer than the specimen. The curve is linear until tensile plate yielding. Compared to model S1, the top plate buckling occurs quite late in model and also in the experiment. The graph reveals that the force level after buckling of the top plate decreases dramatically in experiment as well as in FE analysis. The ultimate force obtained from the FE analysis is almost equal to the ultimate force obtained from the experiment i.e. 1684 kN in FE analysis and 1690 kN in experiment.

The comparison of slips between steel plate and concrete at the beam end is shown in Figure 42(c). The connection of bottom end between steel plate and concrete seems to be stronger in model S2 than in the experiment. In contrast, more slip occurs at the top end in FE analysis than in experiment. The maximum slip of the model at the bottom end is 0.23 mm and at the top end is 0.06 mm. While in experiment, there is 0.29 mm slip at the bottom end and 0.04 mm slip at the top end. In Figure 42(d), force-bottom plate strain relationship is compared. Tensile strain growth is linear until 1460 kN. After that, the growth of the strain occurs rapidly until buckling of top steel plate in experiment as well as in FE analysis. There is more than 16‰ bottom plate strain in experiment and about 15‰ bottom plate strain in FE analysis when the top plate buckles.

7.3 Model S3

The failure modes of model S3 obtained from FE analysis are shown in Figure 43. The model fails due to vertical shear failure which also occurred in specimen S3 during the experiment. Flexural cracks (in Figure 43(b)) are developed in the beginning of FE analysis in the model and they are expanded into shear cracks after the force 1265 kN and 11 mm deflection of the

model. Vertical shear cracks generated in the mid-face and in the outer face in the model are illustrated in the Figure 43(a) and (d) respectively. The tie bar (second from the loading point and marked in red rectangle in the Figure 43(c)) starts to yield at the ultimate force level 2039 kN and 34 mm beam deflection. After that, the force bearing capacity of the model is weakened. The model and specimen fail due to vertical failure. The failure mechanisms are vertical shear cracks followed by yielding of tie bar. The patterns of vertical shear cracks in FE analysis and those in experiment are similar.

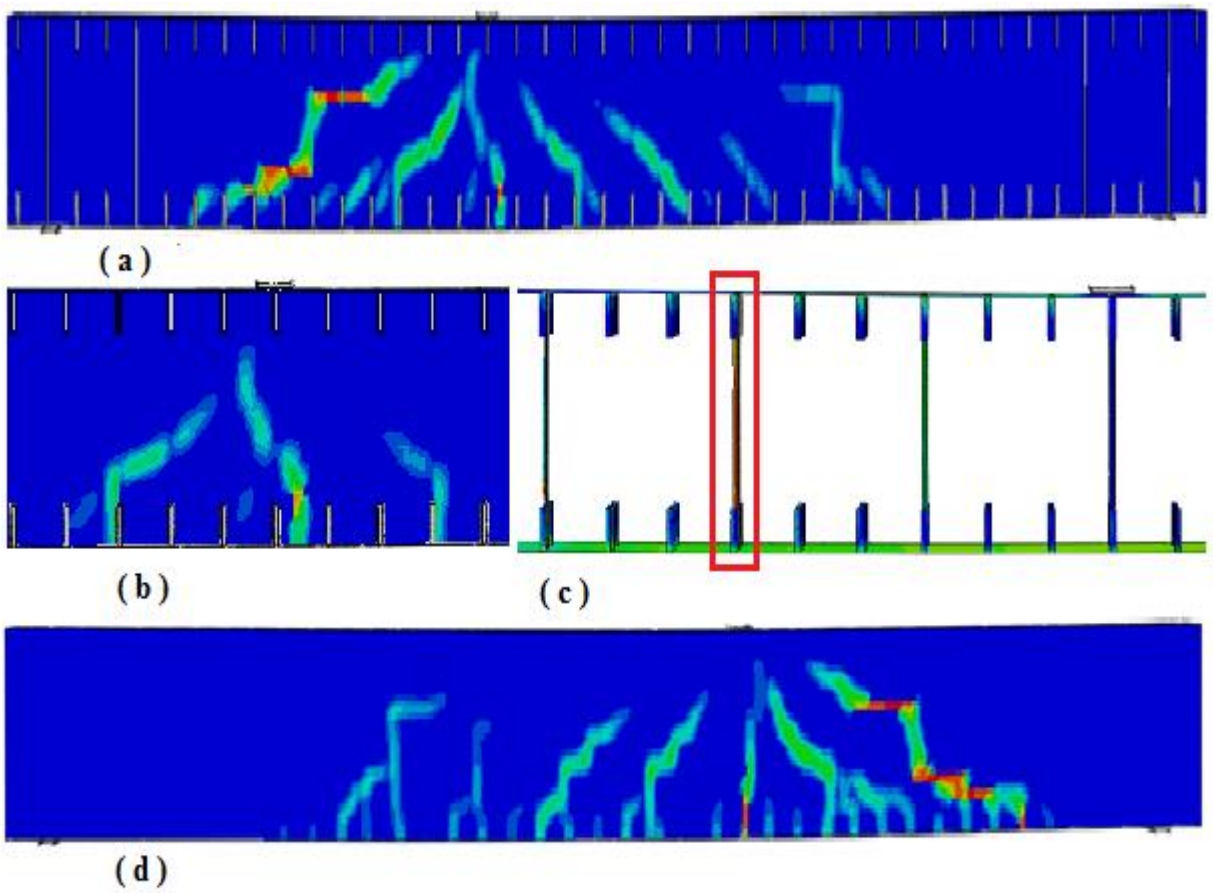

Figure 43: Failure mechanisms of model S3 (a) shear cracks (b) initiation of bending cracks (c) tie bar yielding at the ultimate force (d) shear cracks at the ultimate load in outer face (mirror view)

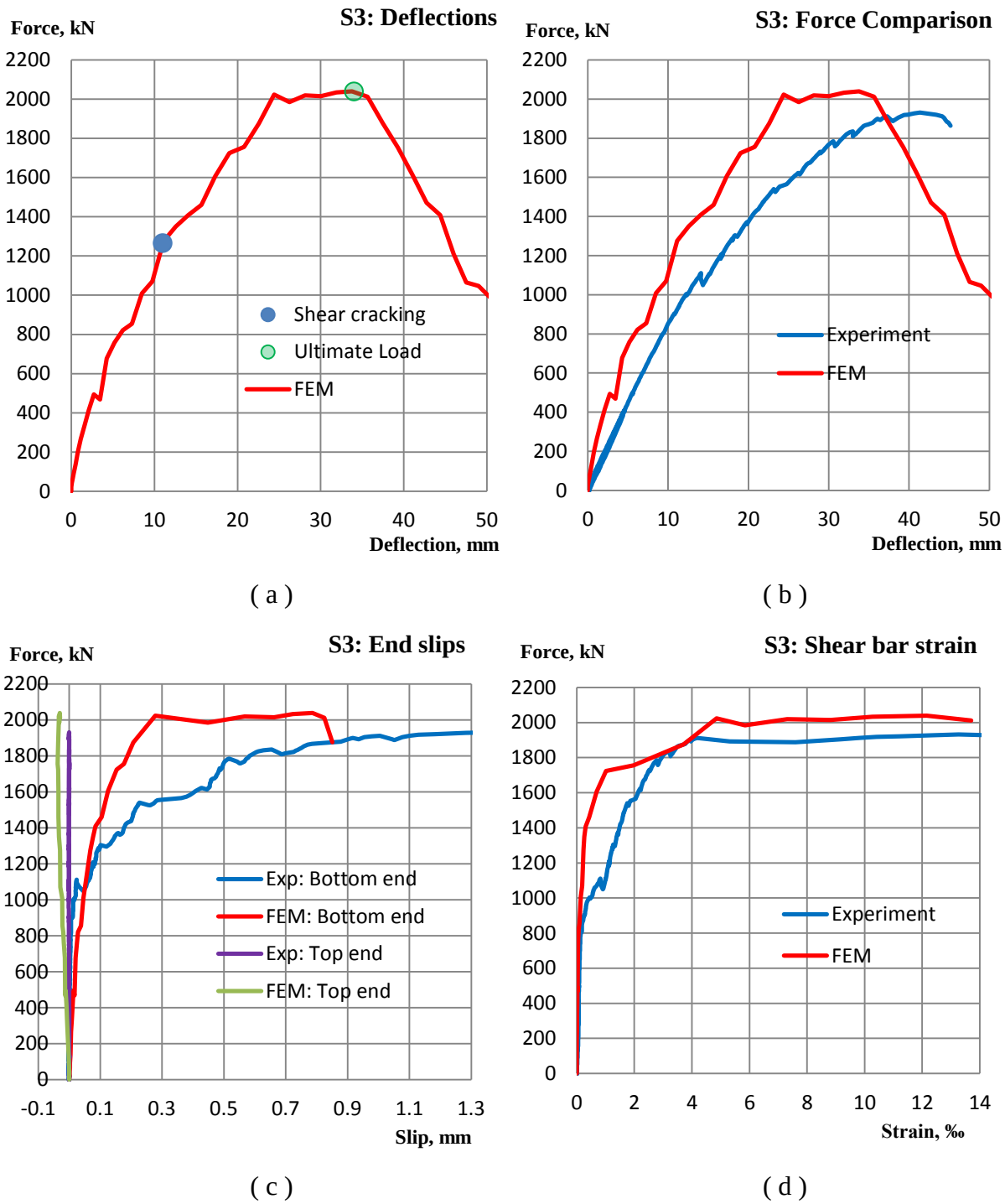

Figure 44: Results for model S3 (a) force versus displacement (b) comparison of force versus displacement (c) comparison of end slips (d) comparison of shear bar strain

In Figure 44, the results for model S3 are compared with those for specimen for S3. Figure 44(a) shows the force-displacement relationship of the model. Initiation of shear cracks occurs in the model at force 1265 kN with 11 mm deflection of the beam indicated by a blue dot. The ultimate force 2039 kN of model S3 is marked by green dot in Figure 44(a). The

comparison of force versus displacement curve between experiment and model is illustrated in Figure 44(b). The graphs are quite linear until force around 1200 kN and 10 mm beam deflection. After that, deflection of the beam grows rapidly and reaches 34 mm in model and 41 mm in experiment at the ultimate force. Model S3 also seems stiffer (Figure 44(b)) than the specimen. The ultimate force of model S3 is 2039 kN which is about 6% higher than the ultimate force obtained experimentally.

Figure 44(c) shows comparison of end slips between steel plate and concrete. Slips remain negligible (less than 0.1 mm) up to the force 1400 kN. After that, the slip at the bottom end is increases significantly in model S3. At the ultimate force, the bottom end slip is 0.8 mm in model and 1.38 mm in experiment. Similarly at the top end, the end slip is 0.03 mm in model and 0.01 mm in experiment at the ultimate force. The results verify that the magnitudes of end slips obtained from FE analysis are comparable with the slips recorded during the experiment. The comparison of strain in tie bar is shown in Figure 44(d). Strain increases linearly until force level 1400 kN and then, it becomes non-linear. At the ultimate force, the tie bar strain of the model is 12 ‰ while 13‰ in the specimen during experiment. The growth patterns of tie bar strain are quite similar.

7.4 Model S4

Figure 45 illustrates failure modes of model S4. Flexural crack initiation is due to normal stress in the model. After force 1000 kN, the flexural cracks expand and transform into shear cracks shown in Figure 45(b). The shear cracks in the mid-face and in the outer face, illustrated in Figure 45(a) and (d) respectively, occur at the ultimate force 1785 kN. At the ultimate force, the tie bar (first from the loading point) marked by red rectangle in Figure 45(c) yields and the load bearing capacity of the model is deteriorated rapidly. Model S4 fails due to vertical shear cracks followed by yielding of shear reinforcements. Vertical failure is the failure mode for model and specimen. The failure mechanisms are vertical shear cracks followed by yielding of tie bar. Cracks in the model are similar with specimen S4 observed in experiment.

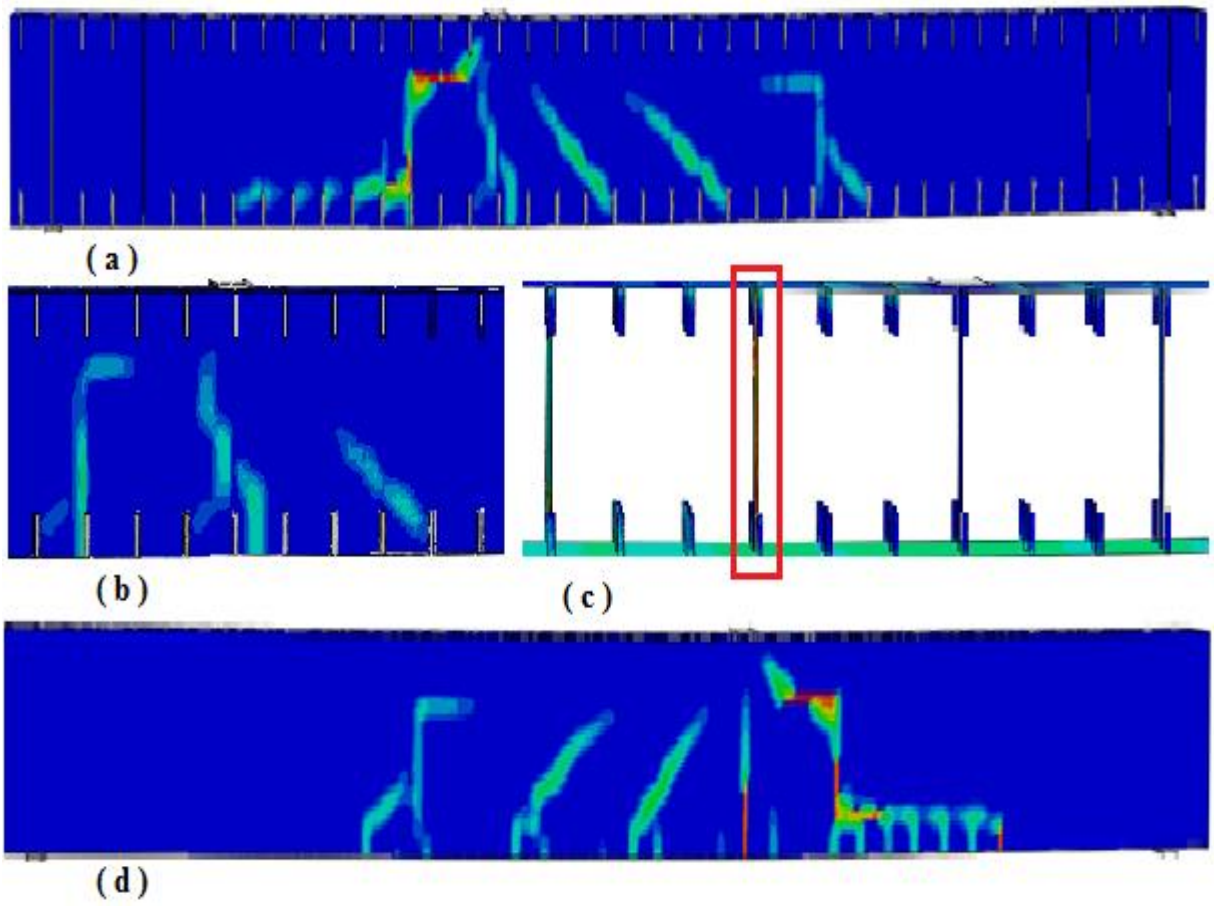

Figure 45: Failure mechanisms of model S4 (a) shear cracks (b) initiation of bending cracks (c) tie bar yielding at the ultimate force (d) shear cracks at the ultimate load in outer face (mirror view)

The results of model S4 and specimen S4 are compared in Figure 46. The force level at which shear cracks start to develop (i.e. 1000 kN) and ultimate force (i.e. 1785 kN) are marked by blue and green dots respectively in Figure 46(a). The force-displacement relationship is linear up to 1000 kN with less than 10 mm deflection of the model. After that, the deflection of model S4 increases rapidly and reaches 35 mm at the ultimate force. Experiment data of specimen S4 contains loading, unloading and reloading phases and, therefore there are discontinuities at the beginning of the curve shown Figure 46(b). Model S4 seems to be stiffer than specimen S4. The ultimate force is 1785 kN at 35 mm deflection for model S4 which is 3% higher than the ultimate force for specimen S4.

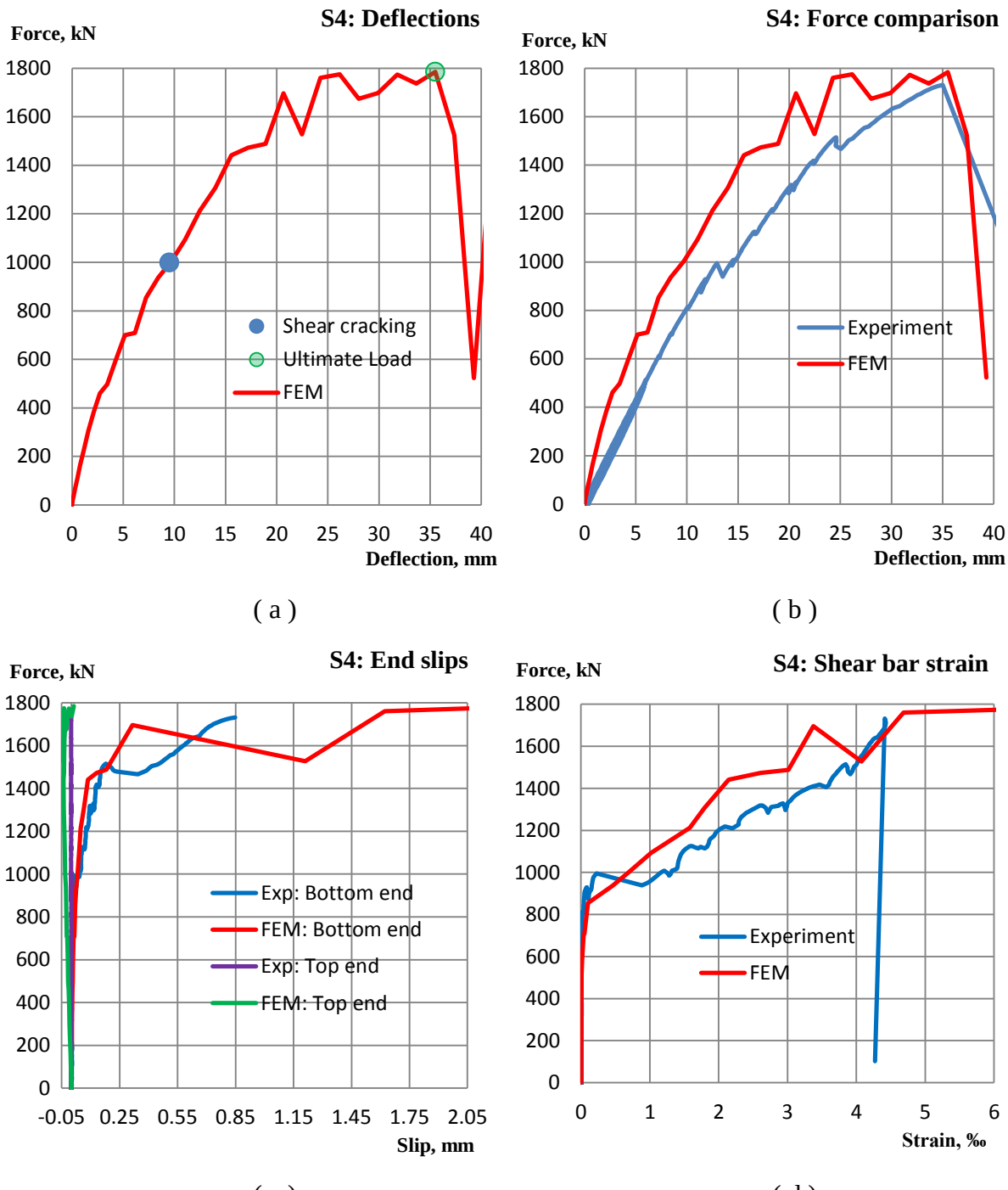

Figure 46: Results for model S4 (a) force versus displacement (b) comparison of force versus displacement (c) comparison of end slips (d) comparison of shear bar strain

Comparison of slips between steel plate and concrete at the end are illustrated in Figure 46(c). In bottom, the end slip is 2.1 mm in model S4 and 0.85 mm in specimen S4. In top, the end slip is 0.04 mm in the model and 0.01 mm in the specimen. Shear bar strains of the model and specimen are compared in Figure 46(d). At the ultimate force 1785 kN, the maximum strain at

shear bar in the model is 6 ‰ and 4.5‰ in the specimen. The growth patterns of tie bar strain are quite similar.

7.5 Model S5

The failures mechanisms of model S5 are illustrated in Figure 47. The model fails due to shear cracking followed by yielding of shear bars which also occurred in specimen S5 during experiment. Flexural cracks (illustrated in Figure 47(b)) initiate the failure in the model and specimen. At force 890 kN and 11 mm beam deflection, flexural cracks transform into shear cracks. Vertical shear cracks occurred in the mid-face and in the outer face are illustrated in Figure 47(a) and (d), respectively. The shear bar (first from the loading point) marked by red rectangle in Figure 47(c) yields at the ultimate force 1475 kN. After that, load bearing capacity of the model is declined significantly deteriorated. The failure mechanisms of the model and specimen are vertical shear cracks followed by yielding of shear bar.

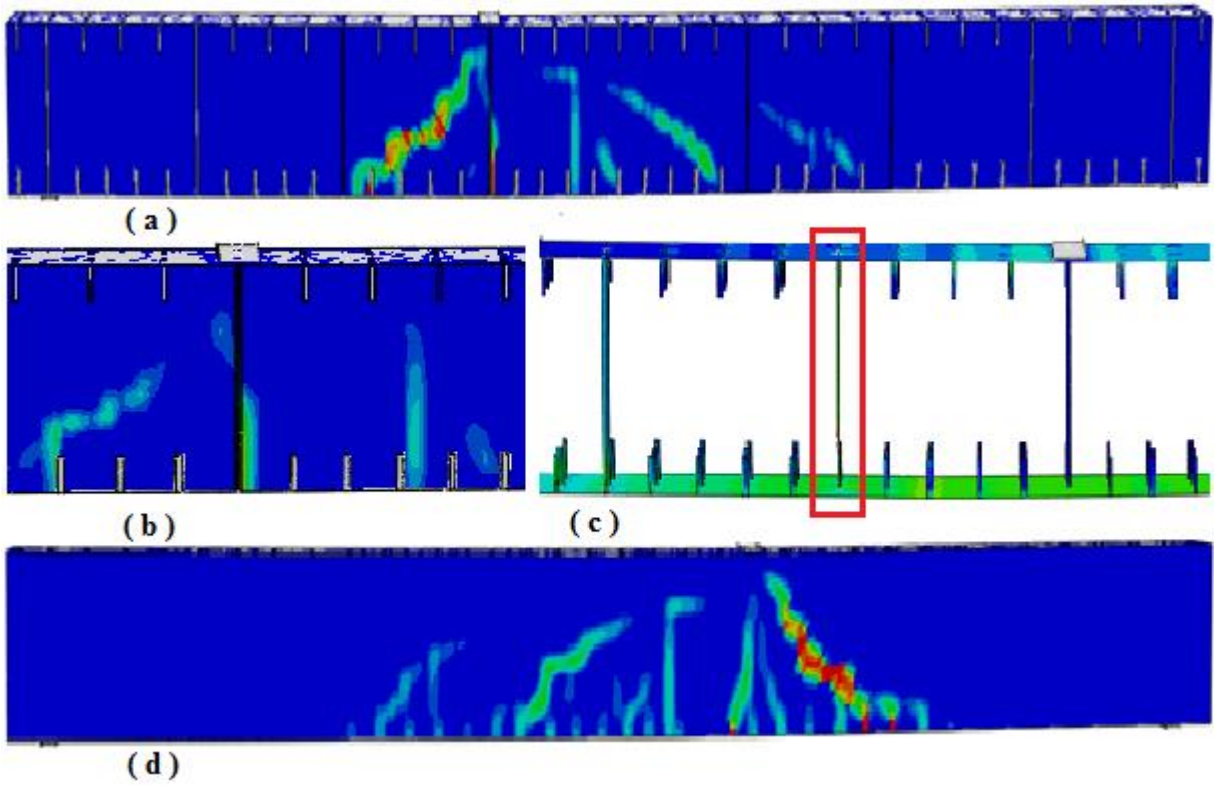

Figure 47: Failure mechanisms of model S5 (a) shear cracks (b) initiation of bending cracks (c) tie bar yielding at the ultimate force (d) shear cracks at the ultimate load in outer face (mirror view)

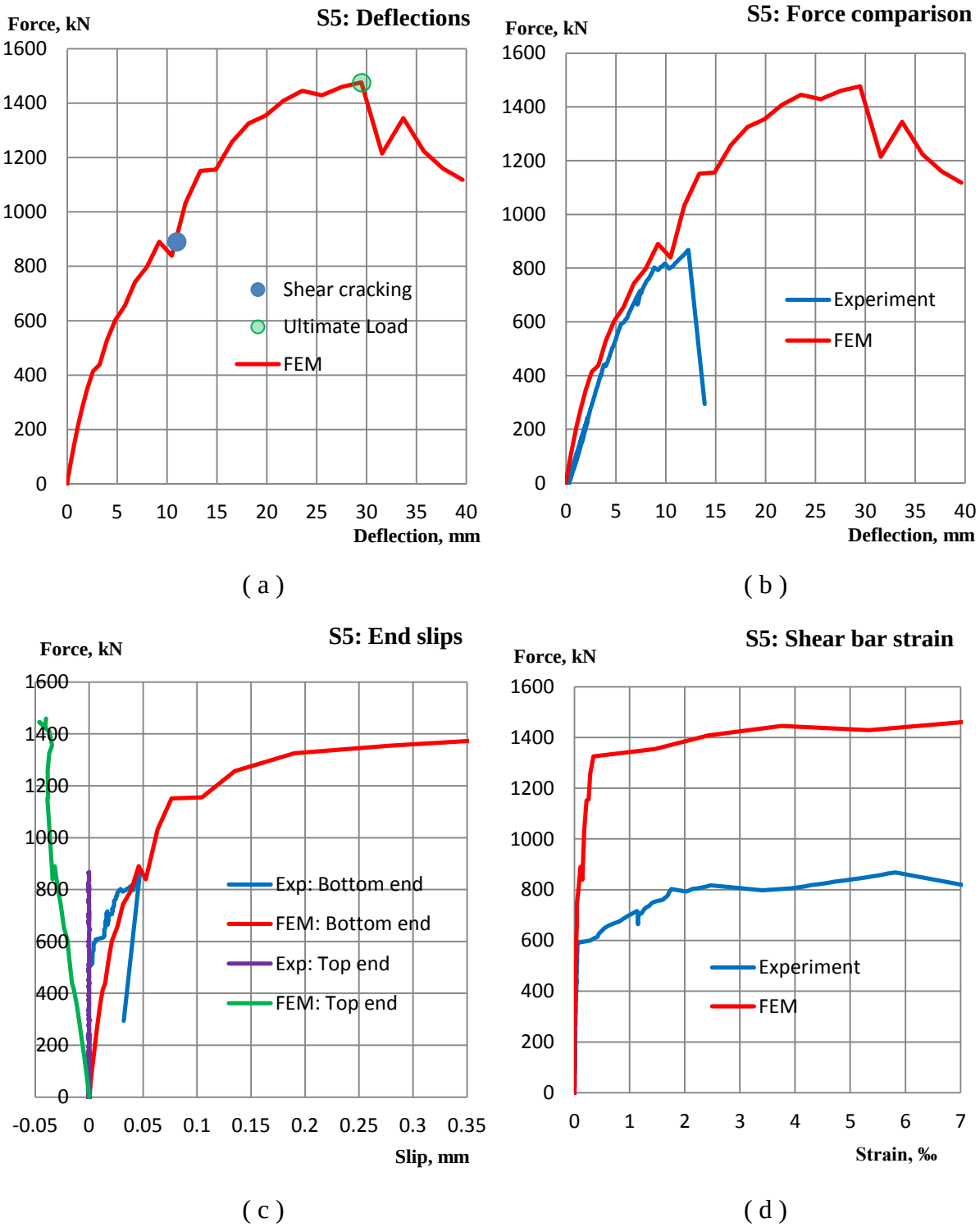

Figure 48: Results for model S5 (a) force versus displacement (b) comparison of force versus displacement (c) comparison of end slips (d) comparison of shear bar strain

The results for model S5 and specimen S5 are compared in Figure 48. Figure 48(a) illustrates the force-displacement relationship of the model. The mid-span deflection increases linearly until force level 890 kN and 9 mm deflection of the beam. After that, deflection of the beam

increases rapidly and model S5 deflects 29 mm at ultimate force of 1475 kN. Shear cracks initiation load and the ultimate load are marked with blue and green dots in Figure 48(a). The force-displacement of the model and specimen are compared in Figure 48(b). This model seems to be much stiffer than the specimen. The reasons behind the stiffness of the model are not recognized yet. The ultimate force for the model is more than 70% higher than the ultimate force for specimen S5.

The comparison of result for the end slip between steel plate and concrete in Figure 48(c) shows that the end slips at bottom in FE analysis is too large for the model. At the ultimate force, the bottom end slip is 3.0 mm in the model S5 but only 0.05 mm in the specimen. Similarly in the top end, the end slip is 0.04 mm in the model and 0.01 mm in the specimen. Figure 48(d) compares shear bar strain for the model and specimen. The strain in the shear bar is linearly increasing until the force level 600 kN. At the ultimate force, the strain at the shear bar in model S5 is 8‰ while the strain at the shear bar in specimen is 6‰.

7.6 Model S6

The failure mechanisms of model S6 are shown in Figure 49. In the model, failure initiates from flexural cracks. When load level reaches 869 kN with 9.5 mm mid-span deflection, the flexural cracks (illustrated in Figure 49(b)) start to change into shear cracks. The model deflects 28 mm at the ultimate force 1575 kN. Figure 49(a) and (d) illustrate shear cracks developed in the mid-face and in the outer face, respectively. Although model S6 is designed to study both vertical and horizontal shear cracks, it fails by vertical cracking followed by yielding in tie bars (first from the loading point and marked with a red rectangle in Figure 49(c)). The failure mechanisms of the model and specimen are vertical shear cracks followed by yielding of shear bar. The vertical shear crack patterns obtained from FE analysis and experiment are similar.

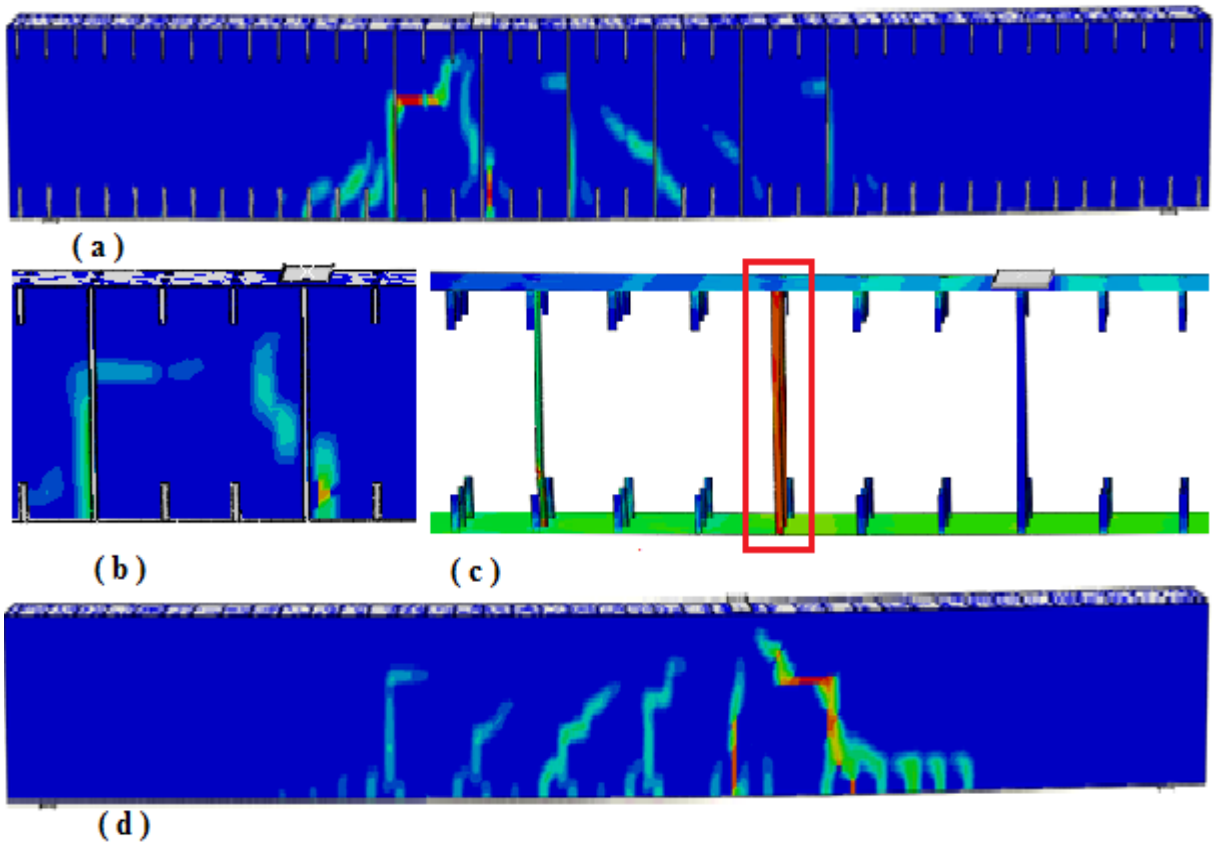

Figure 49: Failure mechanisms of model S6 (a) shear cracks (b) initiation of bending cracks (c) tie bar yielding at the ultimate force (d) shear cracks at the ultimate load in outer face (mirror view)

The results of model S6 and specimen S6 are compared in Figure 50. Force-displacement relationship of the model is illustrated in Figure 50(a). Blue and green dots represent the load levels where shear cracks start to develop and the ultimate force, respectively. The force-displacement relationship is linear until the load level 600 kN with 6 mm deflection of the model. After that, deflection increases rapidly and has the value 28 mm at the ultimate force. Force-displacement relationship of the model and specimen S6 are similar. Also here, experimental data contains the loading, unloading and reloading phases and there are discontinuities in the displacement-load relationship in Figure 50(b). Model S6 seems to be somewhat stiffer than the specimen. The ultimate force for model S6 is 1575 kN which is 18% higher than the ultimate force for specimen S6.

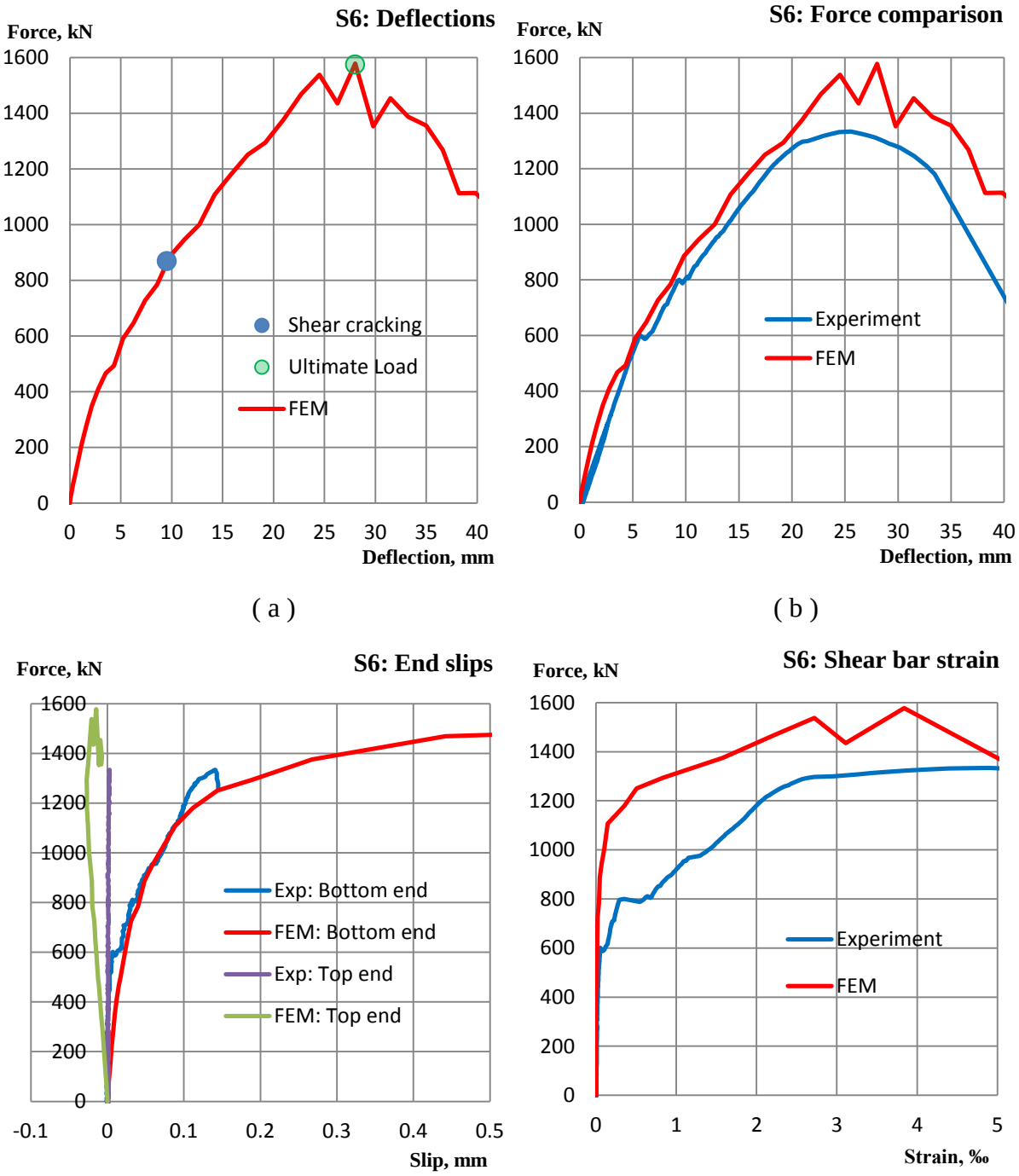

Figure 50: Results for model S6 (a) force versus displacement (b) comparison of force versus displacement (c) comparison of end slips (d) comparison of shear bar strain

Figure 50(c) compares the end slips between steel plate and concrete at the beam end. Slips remain negligible (less than 0.1 mm) up to the force level 1000 kN in model S6. After that, the slip increases significantly at the bottom end. At the ultimate force, the bottom end slip is 2.3 mm in the model and 0.15 mm in the specimen. Similarly in the top end, the end slip is

0.02 mm in the model and 0.01 mm in the speceimen. Figure 50(d) compares the strain in the shear bar. Strain grows linearly until force level reaches 1200 kN. At the ultimate load, the strain at tie bar is 4‰ in model S6 and 5‰ in the specimen.

7.7 Summary of the results

Table 7 summarizes the results (load bearing capacity and failure modes) for SC beams obtained from finite element analysis and experiment. All models fail due to similar failure modes observed in experiment. Model S1 and S2 failed due to yielding of tension (bottom) steel plate followed by buckling in compression (top) steel plate. Model S3, S4, S5 and S6 failed due to vertical shear cracks followed by yielding of shear reinforcements. All models seem to be stiffer than the specimen. In summary, models S1-S4 reproduce the outcomes (failure modes, ultimate load, end slips, and plates or tie bar strain) of the experiments within reasonable accuracy. Although failure modes of model S5 and S6 correspond to experiment results, the load bearing capacities are not predicted correctly.

Table 7: Comparison of load bearing capacity and failure modes

Specimen	Experiment	Model	Difference Experiment vs. Model (%)	Failure Modes
	Ultimate Force (kN)	Ultimate Force (kN)		
S1	1528	1639	7	Flexural failure
S2	1690	1684	-1	Flexural failure
S3	1932	2039	6	Vertical shear failure
S4	1735	1785	3	Vertical shear failure
S5	860	1475	71	Vertical shear failure
S6	1334	1575	18	Vertical shear failure

The ultimate force of model (model S1- S4) is fairly equal. The error of the ultimate force between the model and experiments is ranging from -1% to 7%. Specimen S5 has maximum varying results i.e. FEM has more than 71% higher ultimate force than experiment. Model S5

failed due to vertical shear cracks followed by yielding of tie bars despite the huge error in load bearing capacity. The reasons behind for this are not identified yet. The ultimate force of model S6 is 18% higher than load bearing capacity obtained experimentally. The results verified that model can predict failure mechanisms and load bearing capacity of SC beam, except for severely unreinforced specimen.

8 Effects of parameters

A parametric study with some values of the geometric and material parameters was performed to get a picture about the most important parameters affecting failure mechanisms of a SC beam. The load bearing capacity in flexural failure is directly influenced by parameters of steel. Therefore, the most important parameters for this mode include steel plate thickness, stud arrangement, height of SC beam, and material parameters of the steel plates. Shear reinforcement spacing and tie bar diameter are the most important parameters in shear failure. Shear failure is also influenced by material parameters of tie bar and the height of SC beam. The parameters considered in this study are given in Table 8 and their effects on failure modes of SC beams are described in the following subheadings.

Table 8: Parameters considered for the analysis

Parameter	Values
Height of beam (in mm)	500, 800, and 1200 [mm]
Steel plate thickness	10, 12, and 15 [mm]
Stud diameter (in mm)	16 and 19 [mm]
Stud length (in mm)	50, 100, and 125 [mm]
Shear connectors	Stud and Tie bar, Only Tie bar
Plate material	Carbon-steel, Stainless steel
Tie bar material	Carbon-steel, Gr 8.8 steel

8.1 Effect of plate material on failure in 4-point bending

This is interpreted based on the results obtained from model S1 and S2. Compression plate of model S1 is made from structural steel S355 while compression plate in model S2 is made of stainless steel. Both models have same failure modes with a only difference of magnitude of ultimate load and mid-point deflection. Yielding of tension (bottom) steel plate occurred first and was followed by buckling of compression (top) steel plate. Buckling of the steel plate occurred at 1639 kN load with 84 mm mid-point deflection of the model 1 while compression plate of the model 2 buckled at 1684 kN load and 106 mm mid-point deflection of beam. The results indicate that there are not any significant effects of material parameters of steel plate

on failure modes of SC beams. This may mean that the arrangement and mechanical properties of shear connectors overshadow the material properties of steel plate.

8.2 Effect of beam height on failure in 4-point bending

The effect of beam height in 4-point bending is studied with varying steel plate thickness, height of SC beam, and stud arrangement. The thickness of compression (top) steel plate is 12 mm and the tensile (bottom) steel plate is 12 mm. 500 mm, 800 mm, and 1200 mm beam height are taken into account for analysis purpose. Studs are placed in every 200 mm distance in longitudinal direction in top and bottom surfaces and the other geometric and material parameters are same as in model S1.

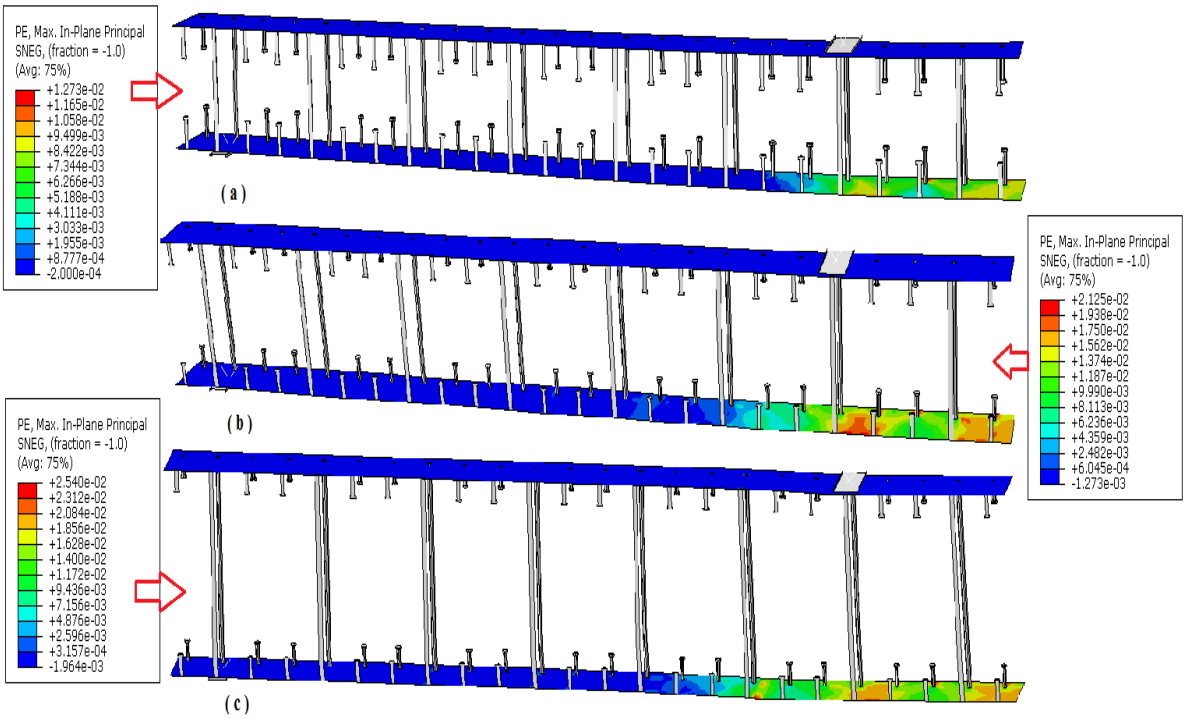

Figure 51: Plastic strain in steel frame of specimen (a) height 500 mm (b) height 800 mm (c) height 1200 mm

The results with different beam heights are illustrated in Figure 51(a), (b), and (c). All three specimens failed due to yielding of tension (bottom) steel plate. There is maximum 1.3% plastic strain at the ultimate force 918 kN for model with height of 500 mm, maximum 2.1% plastic strain at the ultimate force 1526 kN for model with height of 800 mm, and maximum

2.5% plastic strain at the ultimate force 2348 kN for model with height of 1200 mm. It is concluded (based on these models and model S1) that there is a linear dependence of load bearing capacity and yielding of tension steel plate with respect to beam height.

8.3 Effect of stud length on failure in 4-point bending

Stud length is also playing a role in failure of SC beam. To analyse the effects of stud length on failure modes in bending, SC beam model was used with decreasing the stud length from 125 mm to 50 mm. Other geometric and material parameters were being the same as with model S1.

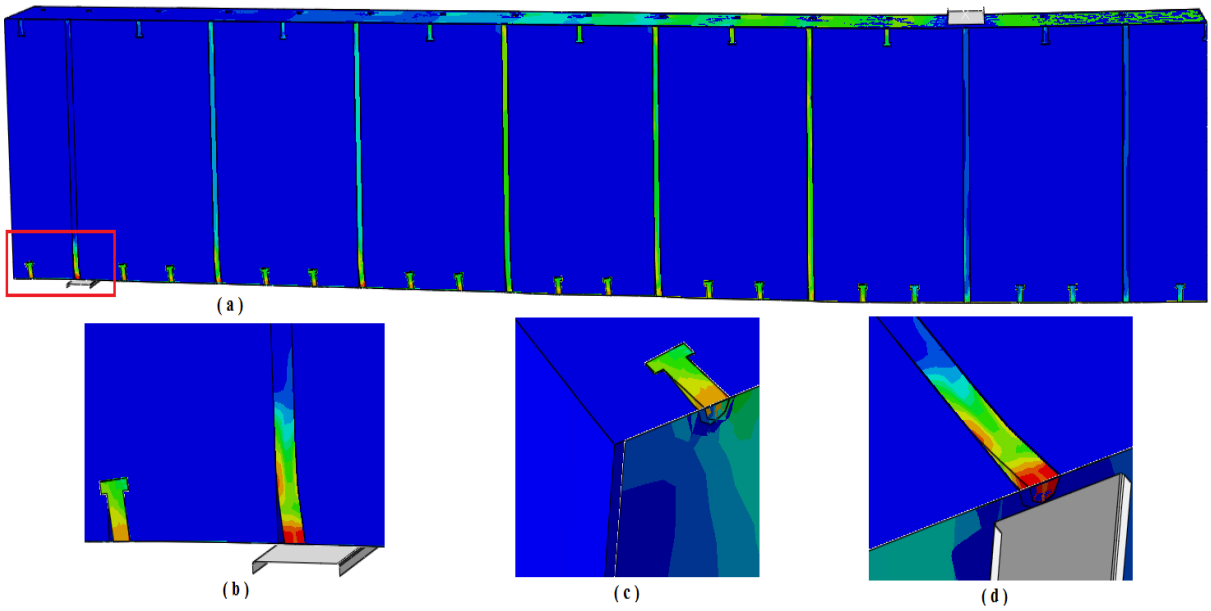

Figure 52: Effect of stud length on failure mechanisms

The effects of stud length on failure modes in bending are illustrated in Figure 52. The FE analysis shows that there is a significant increase of end slip in decrease of stud length. The most vulnerable slippage zone is marked by red rectangle in Figure 52(a) and magnified views are shown in Figure 52(b), (c), and (d). At the ultimate force 1748 kN, there is 2 mm bottom end slip between concrete and steel plate in this model while model S1 has less than 0.3 mm bottom end slip.

8.4 Effect of studs on failure in 3-point bending

To study the effect of studs on failure in three point bending, studs were omitted (stud length zero) and all the parameters were being the same as in model S3. The results obtained from FE analysis of the model is shown in Figure 53. The flexural cracks are initially developed in the model. As the growth of flexural cracks continues, there is also significant increase in end slip between concrete and steel plates. At the ultimate force 885 kN, the model fails due to combined effects of flexural cracks and end slips.

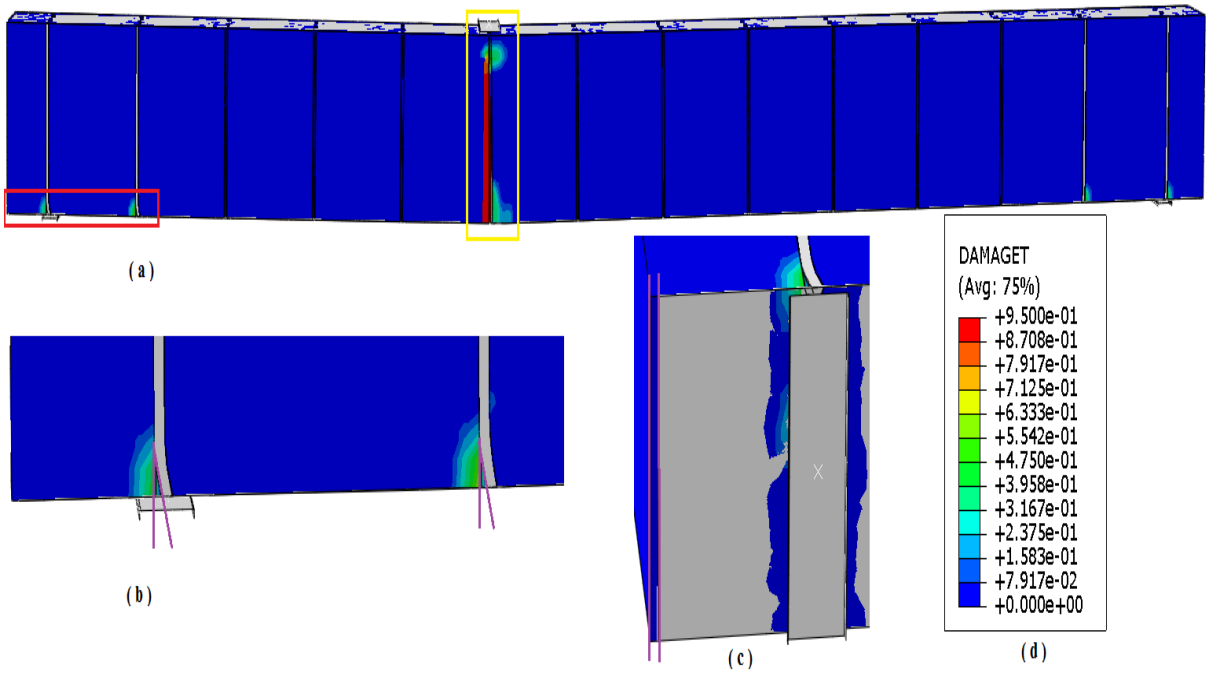

Figure 53: Failure mechanisms without stud

The flexural cracking zone is marked by yellow rectangle and most affected slippage zone is marked by red rectangle in Figure 53(a). At the ultimate force, the maximal damage of concrete due to tension is 95%. Slip between tie bar and concrete as well as the end slip between concrete and steel plate are illustrated in Figure 53(b) and (c), respectively. The slip between concrete and the bottom steel plate is 13 mm at the ultimate force.

8.5 Effect of tie-stud arrangement on failure in 3-point bending

To study the effects of tie-stud arrangement in 3-point bending, spacing of tie bars along longitudinal direction, stud diameter, and stud length were varied geometric parameters of SC beam. The remaining geometric and material parameters were same as in model S3. Tie bars were placed in 400 mm distance along the longitudinal direction in contrast to the 600 mm distance in model S3. Therefore, studs remain in 200 mm interval and there is only one stud between the tie bars in the longitudinal direction.

In the first specimen, the diameter of stud is 19 mm and length is 125 mm. Results for this model are illustrated in Figure 54. Tensile concrete cracks are shown in Figure 54(a) and yielded tie bar marked by red rectangle is shown in Figure 54(b). At the ultimate load 1978 kN, the model fails due to shear cracking of concrete and yielding of tie bars. There is 0.35 mm of end slip between concrete and bottom steel plate (Figure 54(c)) at the ultimate force.

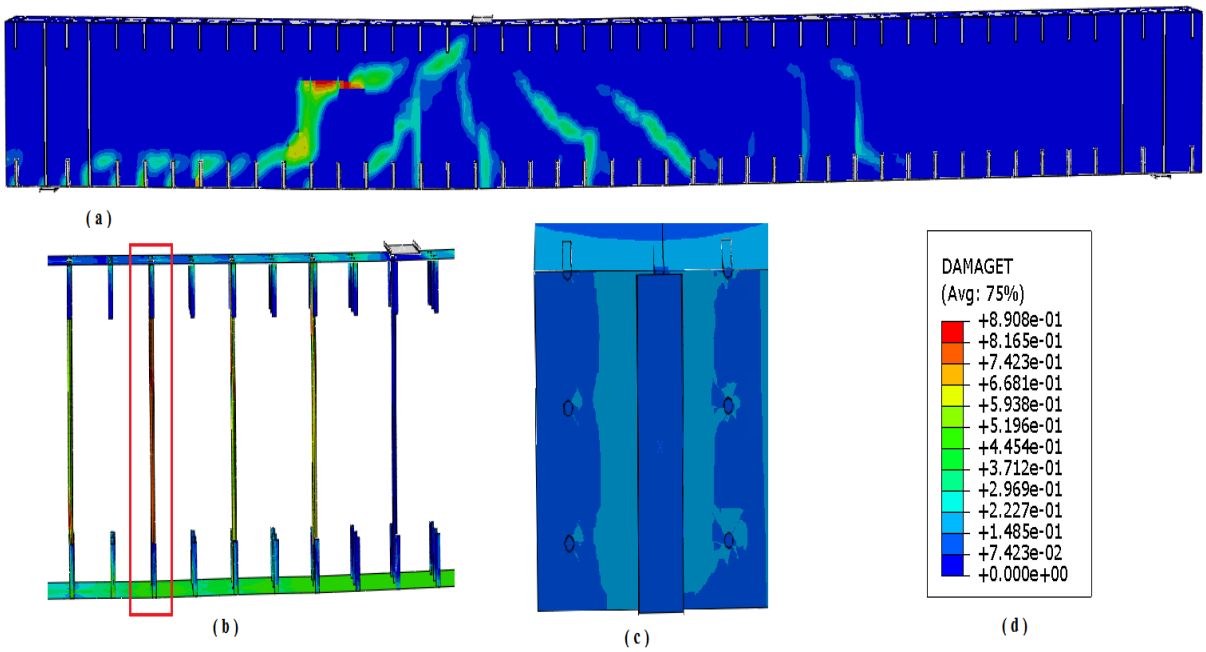

Figure 54: Failure mechanisms (stud diameter 19 mm and length 125 mm)

The second specimen has 16 mm stud's diameter and 100 mm stud's length. The results for this model are illustrated in Figure 55. Concrete tensile cracks, yielded tie bar marked by red rectangle, and end slip between concrete and bottom steel plate marked by dashed orange line

are shown in Figure 55(a), (b), and (c), respectively. The model failed at the ultimate force 1784 kN by combined vertical shear cracks and yielding of tie bars. At the ultimate force, end slip between concrete and the bottom steel plate is 3.5 mm.

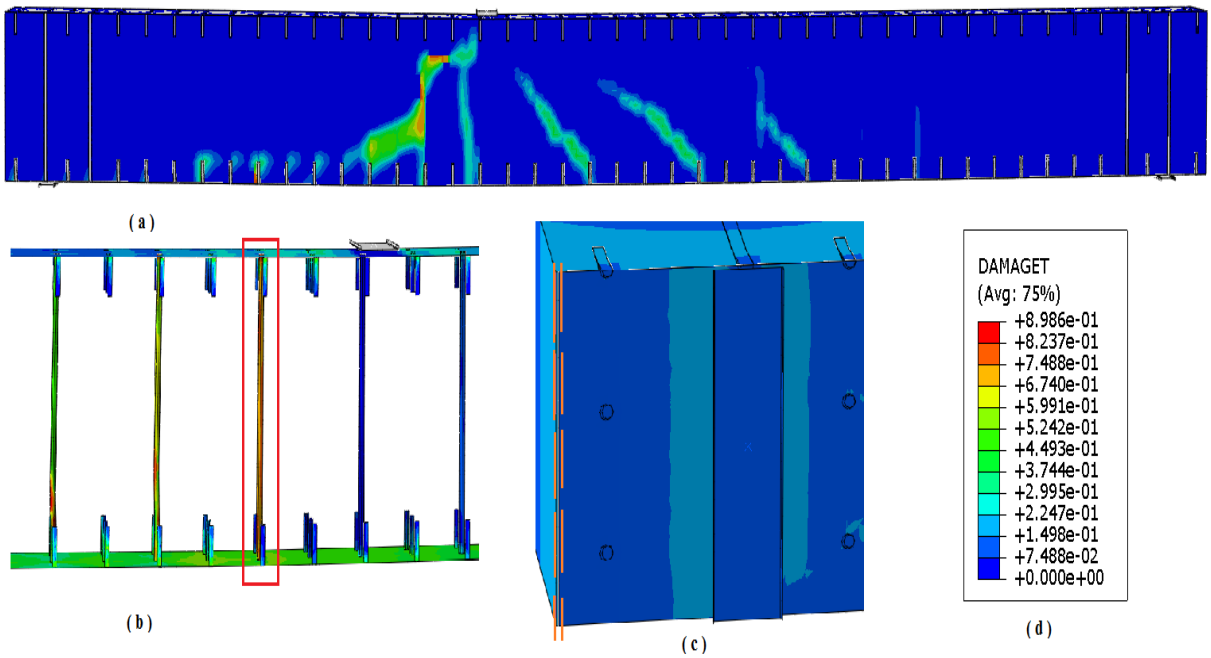

Figure 55: Failure mechanisms (stud diameter 16 mm and length 100 mm)

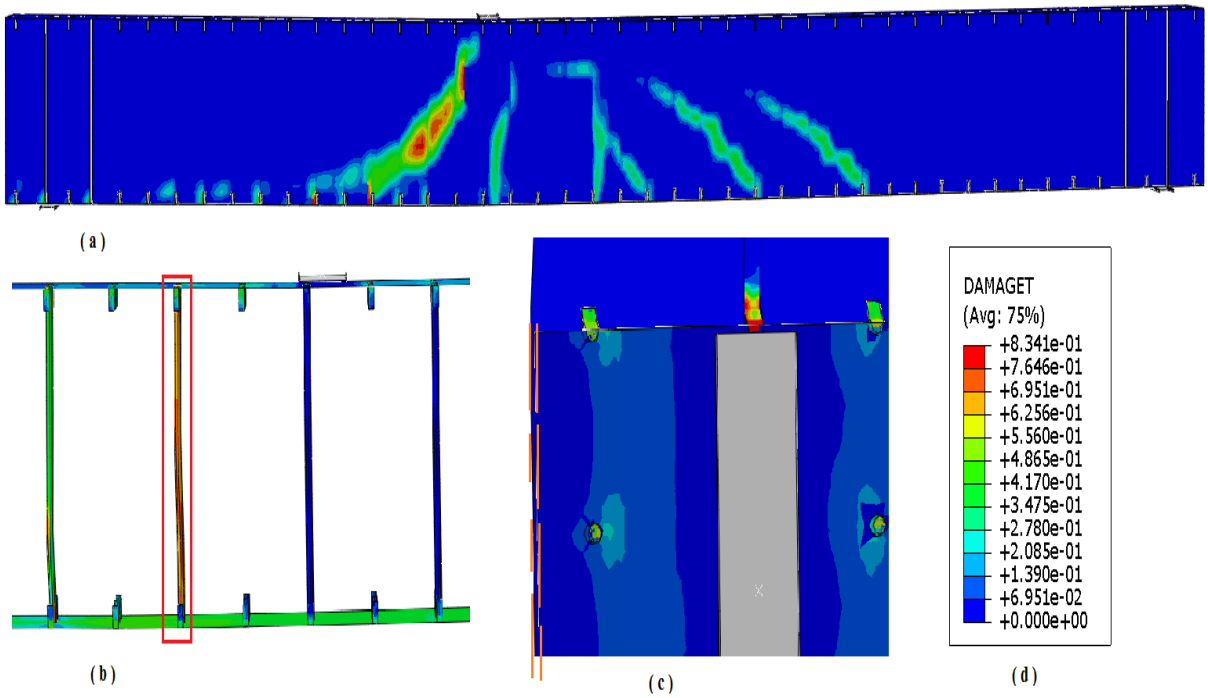

Figure 56: Failure mechanisms (stud diameter 16 mm and length 50 mm)

The third specimen to study effects of stud has 16 mm stud diameter and 50 mm stud length. The failure modes of this model are illustrated in Figure 56. At the ultimate force 1788 kN, the failure mechanisms are vertical shear cracks in the concrete, yielding of tie bars, and end slip between concrete and the bottom steel plate. Yielded tie bar is shown in Figure 56(b) by red rectangle and the end slip of the beam is shown in Figure 56(c) by dashed orange line. There is a 4 mm end slip between concrete and the bottom plate at the ultimate load.

The specimens illustrated in figure 50-52 fails at the ultimate force due to shear cracking of concrete followed by yielding of tie bars. Narrowly spaced tie bars neither significantly affects the failure modes nor the magnitude of the ultimate force of shear specimens. The stud diameter and length significantly influence end slip between concrete and the bottom steel plate. With decreasing diameter and length of stud, there is a significant increase in the end slip. Based on the results, it is concluded that the geometric parameters of studs directly influence the failure modes of SC beams such as shear crack on concrete, yielding of shear reinforcements, and slip between concrete and steel plate at the beam end.

8.6 Effect of beam height on failure in 3-point bending

The beam height of SC beams is varied from 500 mm to 1200 mm. The diameter of tie bars is 20 mm. In this SC model, there are two kinds of stud parameters (19 mm diameter and 125 mm length or 16 mm diameter and 50 mm length). The remaining geometric and material parameters are same as the parameters of model S3.

The first specimen has beam height 1200 mm, stud diameter of 19 mm and stud length of 125 mm. The results are shown in Figure 57. Flexural cracks initiating the failure gradually expand into shear cracks. The model fails at the ultimate force 2550 kN because of shear cracking in concrete followed by yielding of tie bar. Vertical shear cracks and yielded tie bar (marked by red rectangle) at the ultimate force are illustrated in Figure 57(a) and (b) respectively. End slip between concrete and the bottom steel plate is 0.6 mm which is shown in Figure 57(c).

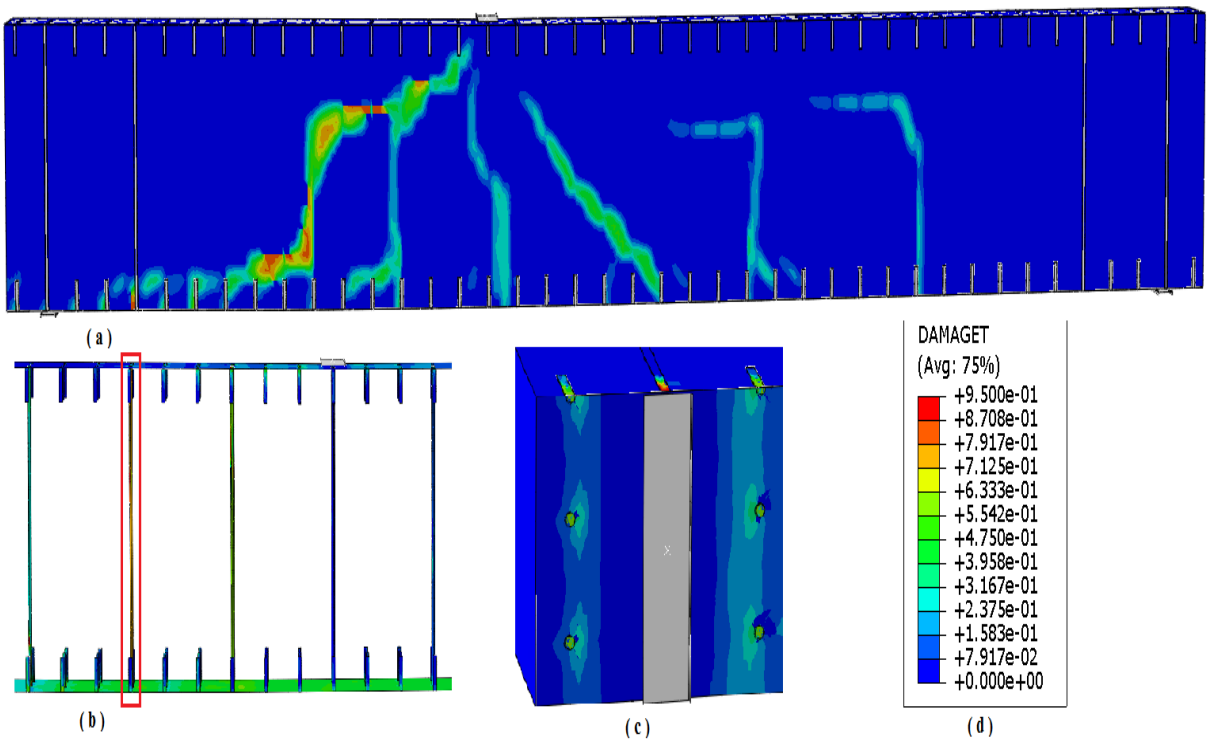

Figure 57: Failure mechanisms (beam height 1200 mm, long stud)

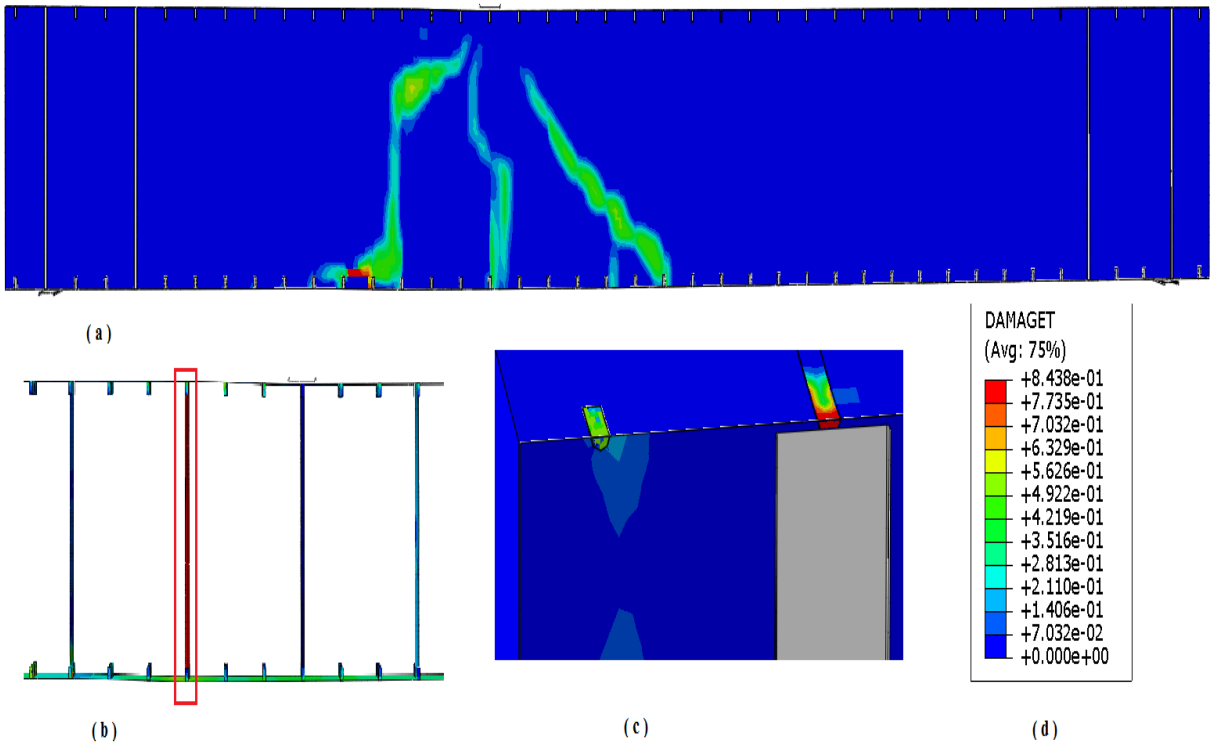

Figure 58: Failure mechanisms (beam height 1200 mm, short stud)

The second specimen also has beam height 1200 mm while stud diameter is 16 mm and stud length is 50 mm. Failure modes are shown in Figure 58. Failure is due to the combined effects

of shear cracks, yielding of tie bars, and end slip between concrete and the bottom plate. Shear cracks and yielded tie bar (marked by red rectangle) at the ultimate force 2279 kN are illustrated in Figure 58(a) and (b) respectively. The end slips between concrete and the bottom steel plate (illustrated in Figure 58(c)) is 0.5 mm at the ultimate force.

The third specimen is 500 mm high. Stud diameter is 19 mm and length is 125 mm. The results are shown in Figure 59. Failure mechanisms at the ultimate force 1191 kN are similar with the previous models described in this section. Failure at the ultimate force is due to shear cracks in concrete and yielding of tie bars. Vertical shear cracks and yielded tie bar (marked by red rectangle) at the ultimate force are illustrated in Figure 59(a) and (b) respectively. The end slip between concrete and the bottom steel plate (illustrated in Figure 59(c)) is 1.5 mm at the ultimate force.

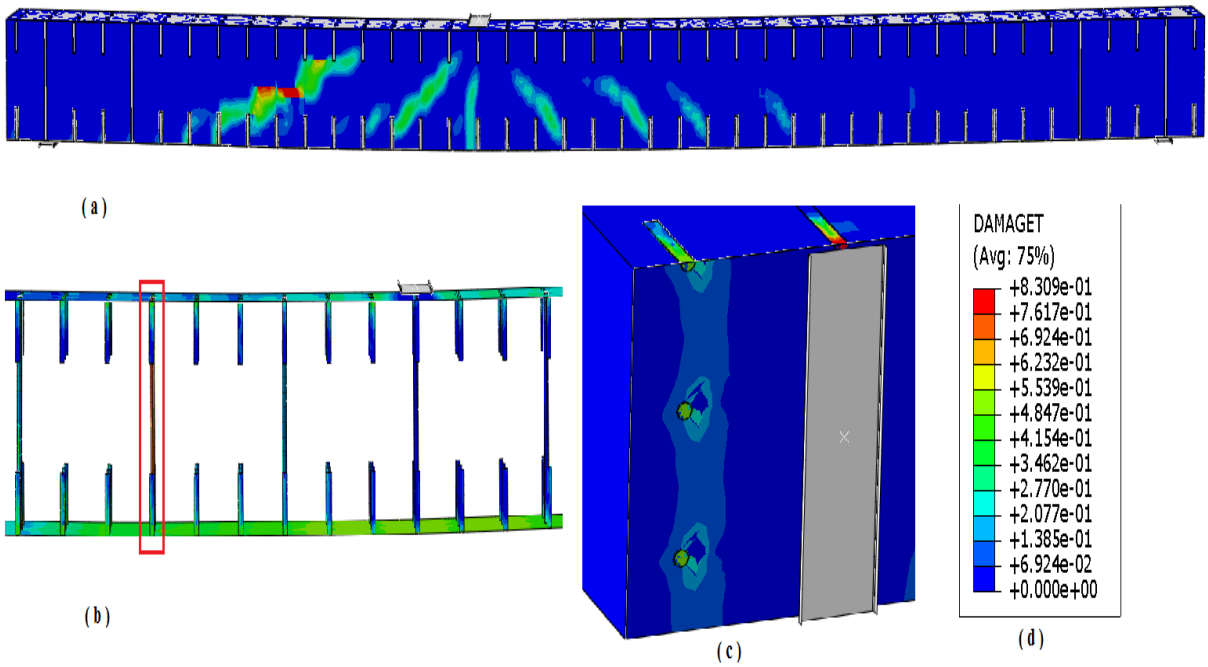

Figure 59: Failure mechanisms (beam height 500 mm, long stud)

Failure modes are similar, although the beam height of SC beams is varied from 500 mm to 1200 mm. It seems that SC beams fail because of shear cracks in concrete and tie bar yielding irrespective of beam height in three point bending.

8.7 Effect of tie bar on failure in 3-point bending

The effects of tie bar parameters on failure in three point bending was assessed by comparing the results for model S3, model S4 and parametric studies of shear specimens. In specimen S3, shear bars were made from S355 steel and welded to the inner surfaces of steel plates and embedded in concrete. In Specimen S4, threaded Gr 8.8 steel bars were fastened between steel plates and embedded in concrete. Although the magnitudes of ultimate force are different between these two specimens, failure mechanisms in both cases are same. It seems that the failure mechanisms are identical with different material parameters of tie bars although the magnitudes of ultimate force may be different.

9 Conclusions

In this thesis, SC beam model was formulated and implemented in Abaqus/Explicit, FE results were validated against experiment results and the effects of geometric and material parameters on failure modes were studied. Commercial FE software Abaqus/Explicit was used to analyse the failure modes of SC beams. To reduce computational works, mirror symmetric technique was applied to create a quarter and a half model of the original size of the beam. The modelling cost and time in this research was reduced significantly by using Plug-In. According to simulation and experiment results, the most common failure modes of SC elements were flexural failure, shear failure, and de-bonding between concrete and steel plate.

Material models played a crucial role in achieving convincing results. Structural steel S355, steel S235-J2G3+C450, and grade 8.8 steel were modelled according to isotropic elasto-plastic with strain hardening approach. Ramberg-Osgood model with Hill's modification described the material properties of stainless steel. The non-linear behaviour of concrete was analysed according to damage plasticity approach. Behaviour of concrete is significantly different in tensile and compression regimes. Therefore, the material property of concrete in compression was modelled according to EN 1992-1-1: Eurocode 2 clause 3.1.4, and in tension according to fracture energy cracking criterion.

A quasi-static method was used in the FE analysis. Load was applied by displacement control method. General contact interactions between surfaces were created in the FE analysis. Surfaces of part instances in the model were connected together by tie constraints. Supports were created in the 'Initial' step with specific degree of freedoms (rotation was restrained in the *y* and *z* direction and the translation in *z* direction) while load was created in the 'Applied load' step.

The models were validated against experiment results by considering somewhat different geometries and loading conditions. The results by models and experiment were similar. Specimen S1 and S2 failed due to yielding of tensile (bottom) steel plate followed by buckling of compression (top) steel plate. The remaining specimen S3-S6 failed due to shear cracking in concrete followed by yielding of shear bars. With specimen S1 and S2, the

ultimate force for the model and experiment agreed fairly well. The difference is ranging from -1% to 7%. The ultimate force predicted by the model was 6% and 3% higher than the experiment one in specimen S3 and S4, respectively. The ultimate force predicted by the model was more than 70% higher than that of the experiment in specimen S5. The ultimate force predicted by the model was more than 18% higher than experiment in specimen S6. The exact reasons behind the significant difference in the ultimate force have not been identified yet.

The predicted end slips at the top of all models were higher than in experiments. Predicted end slips at the bottom in model S1, S2, and S3 were lower and those of S4, S5, and S6 were higher than given by experiment. Although magnitude of strain (both steel plate and tie bar) was higher in model than in the experiment, strain curves were similar. The results in model and experiments are in good agreement in both failure mechanisms and magnitudes of outcomes except severely unreinforced cases of 3-point bending.

Parametric study indicates that thickness of the tensile steel plate and stud geometry have effect on the failure mechanisms in 4-point bending. Shear specimens were affected by stud geometry and stud position. With equal thickness of the tensile and compression steel plates, yielding of tensile steel plate was the failure mechanism in 4-point bending. Furthermore, stud geometric parameters significantly influenced the end slip between concrete and steel plate. In the range of parametric study, failure modes were neither affected by material parameters of steel plate in 4-point bending nor by material parameters of tie bar in 3-point bending. However, the ultimate force was affected.

9.1 Recommendations for future studies

After the completion of the thesis work, there are still issues remained for the future works. The foremost issue is the improvement of model. The material model of shear reinforcement could be improved to obtain better results for specimens in shear. Mesh size and proper meshing technique can also improve the results of FE analysis. The model seemed stiffer and the ultimate force is higher compared to the experiments. These errors can be reduced by developing improved contact models for the surfaces of SC beams. Although CDP model is the best approach to replicate the behaviour of concrete, it can also only provide general capability of analysis.

There were limited cases of SC configurations in the parametric study. The effects of geometric and material parameters on failure mechanisms of SC beams could be studied in wider ranges. In addition to geometric and material parameters, the effects of axial loading on specimen in bending could be studied. Parametric study of specimen in a 3-point bending with sparsely distributed shear reinforcements is limited due to large error of the ultimate force of specimen S5 between experiment and model. Therefore, parametric study of this kind of SC configuration would also be essential to recognize failure modes in the 3-point bending.

10 References

[1] Kim, C. H. Lee, H. W. Lee, J. B. and Noh, S. H. (2007) 'A study of fabrications of Steel Plate Concrete (SC) modular systems for nuclear power plants'. *Korean Nuclear Society.*

[2] Nelson Stud Welding, Inc. (2011), Shear Connector/ Concrete anchor Catalogue

[3] Oduyemi, T. O. S. and Wright, H. D. (1989) 'An experimental investigation into the behaviour of double-skin sandwich beams'. *Journal of Constructional Steel Research,* vol. 14, no. 3, pp. 197–220

[4] Fülöp, L. A. Guyot, N. and Petite, J. (2014) 'Analytical design of the ambient temperature SC element tests'. *VTT Technical Research Centre of Finland, Espoo,* Technical Report RFSR CT 2013-00017.

[5] IAEA (2004) 'Construction and commissioning experience of evolutionary water cooled nuclear power plants' *International atomic energy agency,* Austria

[6] Marshall, P.W. Palmer, A.C. Liew, J.Y.R. Wang, T.Y. and Thein, M.K.W. (2010) 'Bond Enhancement for Sandwich Shell Ice Wall'. *International Conference and Exhibition on Performance of Ships and Structures in Ice,* 20-23 September, Alaska, USA.

[7] Kaneuji, A. Okuda, Y. Hara, K. and Masumoto, H. (1989) 'Feasibility study of concrete filled steel (SC) structure for reactor building'. *International conference on Structural Mechanics in Reactor Technology (SMiRT).*

[8] Nawy, E.G. (2009) *Reinforced Concrete: A Fundamental Approach* (6th Edition). Upper Saddle River, N.J.: Pearson Prentice Hall

[9] Solomon, S.K., Smith, D.W., and Cusens, A.R. (1976) 'Flexural tests of steel-concrete-steel sandwiches'. *Magazine of Concrete Research*; 28(94):13-20.

[10] Burgan, B. A. and Naji, F. J. (1998) 'Steel-concrete-steel Sandwich Construction'. *Journal of Constructional Steel Research*, vol. 46, no. l-3: 219-344.

[11] Pryer, J.W. and Bowerman, H.G. (1998) 'The development and use of British steel Bi-Steel'. *Journal of Constructional Steel Research*; 46(1-3):15.

[12] Liew, J.Y. Wang, T.Y. and Sohel, K.M.A. (2008) 'Separation Prevention Shear Connectors for Sandwich Composite Structures'. *US Provisional Patent* Application No. 61/047, 130.

[13] Shukry, M.E.S. (1986) 'Composite shells subjected to expternal pressure and to point loads'. *University of Manchester,* UK. PhD thesis.

[14] Kumar, G. (2000) ‘Double skin composite construction’. *National University of Singapore*, Singapore, Master thesis.

[15] Sohel, K.M.A. (2008) ‘Impact behaviour of Steel-Composite sandwich beams’. *National University of Singapore*, Singapore, PhD. thesis.

[16] Donnadieu, M. and Fülöp, L. A. (2015) ‘Non-Linear Finite Element Modelling of Steel Concrete-Steel Members in Bending and Shear’. *Nordic Steel Construction Conference 2015,* Tampere, Finland.

[17] Koukkari, H. and Fülöp, L. A. (2015) ‘Material properties, loading and the measured responses for the ambient temperature tests’. *VTT Technical Research Centre of Finland, Espoo,* Technical Report.

[18] EN 1992-1-1:2004 Eurocode 2: Design of concrete structures - Part 1-1:General rules and rules for buildings

[19] Sohel, K.M.A. Liew, J.Y. and Zhang, M.H. (2011) ‘Analysis and design of steel-concrete composite sandwich systems subjected to extreme loads’ *Frontiers of Architecture and Civil Enginering in China*

[20] EN 1993-1-1:2005 Eurocode 3: Design of steel structures - Part 1-1: General rules and rules for buildings

[21] Varma, A. H. Sener, K. C. Zhang, K. Coogler, K. and Malushte, S. R.(2011) ‘Out-of plane shear behaviour of SC composite structures’ *International conference on Structural Mechanics in Reactor Technology (SMiRT).*

[22] Xie, M. Foundoukos, N. and Chapman, J.C. (2007) ‘Static tests on Steel–Concrete–Steel sandwich beams’. *Journal of Constructional steel research*; 63(6):735-750.

[23] Wright, H.D. and Oduyemi, T.O.S. (1991) ‘Partial interaction analysis of double skin composite beams’. *Journal of Constructional Steel Research,* Vol.19, pages 257–79.

[24] Hearn, E.J. (1997) *Mechanics of Materials, Volume 1 - An Introduction to the Mechanics of Elastic and Plastic Deformation of Solids and Structural Materials* (3rd Edition). Oxford: Butterworth Heinemann.

[25] Hibbeler, R.C. (2013) *Mechanics of Materials* (9th Edition). London: Prentice Hall International.

[26] EN 1994-1-1:2004 Eurocode 4: Design of composite steel and concrete structures-Part 1-1: General rules and rules for buildings

[27] ACI-ASCE COMMITTEE 326 (1962) ‘Shear and diagonal tension’. *Journal of the American Concrete Institute*; 59(1):1-30, 59(2):277-334, 59(3):353-396.

[28] Teng, J.G. and Chen, J.F. (2007) 'Debonding failures of RC beams strengthened with externally bonded FRP reinforcement: behaviour and modelling' *Asia-Pacific Conference on FRP in Structures (APFIS 2007)*

[29] Dassault Systèmes (2013) Abaqus Theory Manual, version 6.13

[30] Hradil, P. Talja, A. Real, E. and Mirambell, E. (2014) 'Structural Application of Ferritic Stainless Steel: Structural performance of steel members'. *VTT Technical Research Centre of Finland, Espoo,* Technical Report

[31] Rodríguez, J. Martínez, F. and Martí, J. (2013) 'Concrete Constitutive Model, Calibration and Applications' *SIMULIA Community Conference*

[32] Jankowiak, T. and Lodygowski, T. (2005) 'Identification of parameters of concrete damage plasticity constitutive model'. *Foundation of civil and environmental engineering.* No.6, pp 53-69

[33] Kmiecik, P. Kaminski, M. (2011) 'Modelling of reinforced concrete structures and composite structures with concrete strength degradation taken into consideration' *Archives of civil and mechanical engineering*, Vol. XI No. 3

[34] Wang, T. and Hsu, T.T.C. (2001) 'Nonlinear finite element analysis of concrete structures using new constitutive models'. *Computers and Structures,* vol. 79.

[35] International Federation for Structural Concrete. (2013) *FIB Model Code for Concrete Structures 2010,* Berlin: Wilhelm Ernst & Sohn.

Appendixes

Appendix I: Drawing of SC beam

Specimen S1

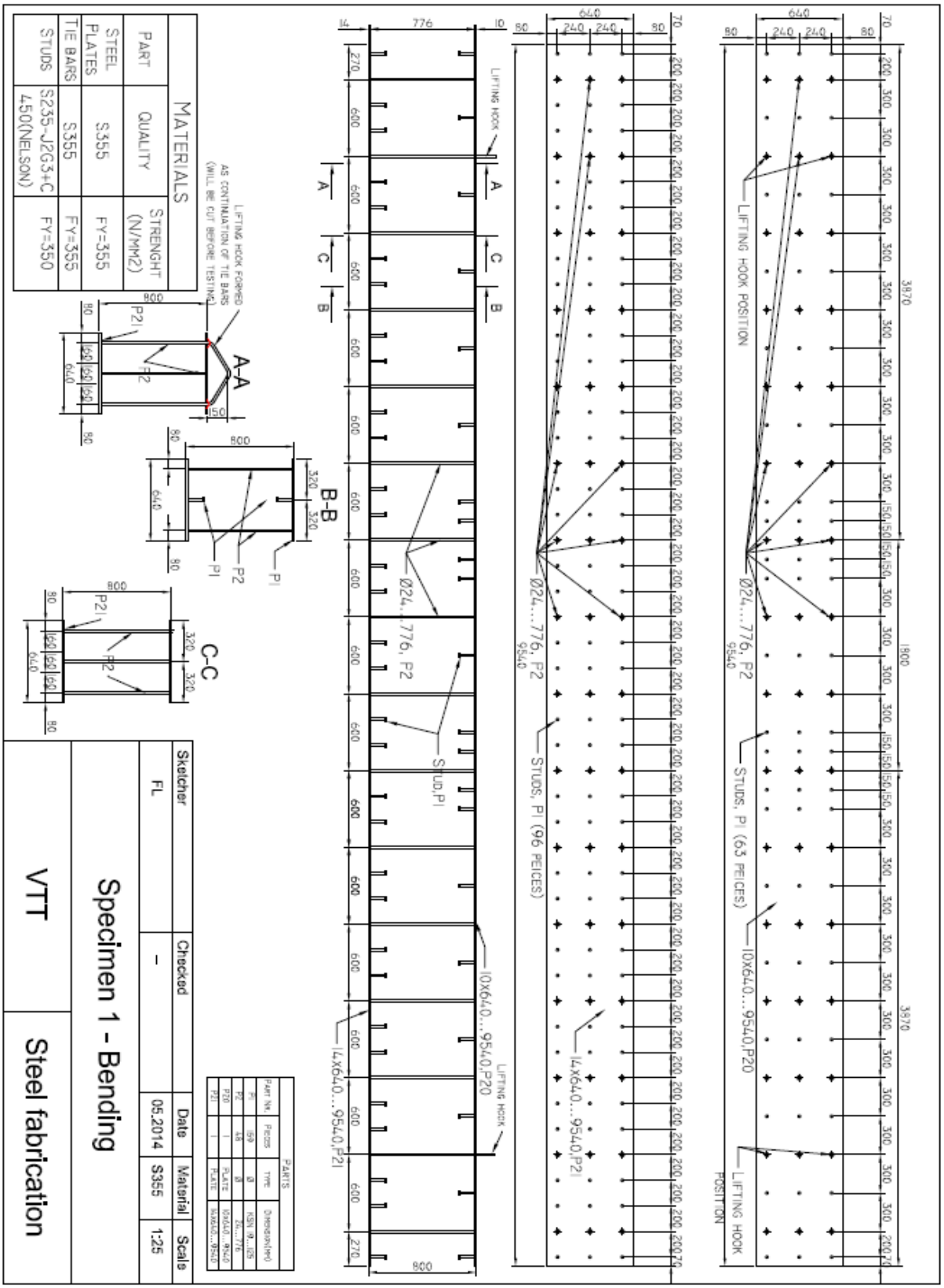

Specimen S2

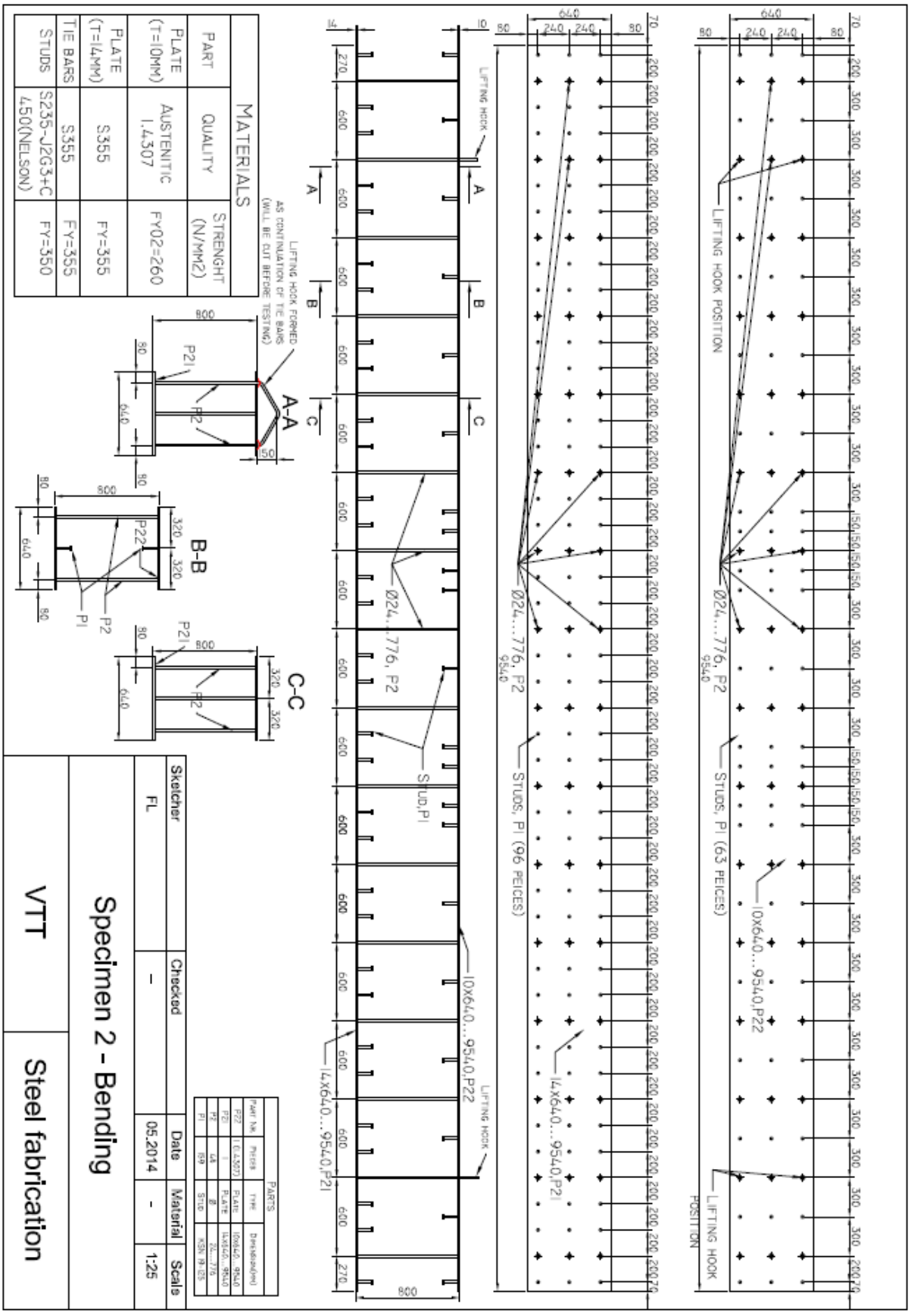
MATERIALS
PART
QUALITY
STRENGHT (N/MM2)
PLATE (T=10MM)
AUSTENITIC 1.4307
FY02=260
PLATE (T=14MM)
S355
FY=355
TIE BARS
S355
FY=355
STUDS
S235-J2G3+C 450(NELSON)
FY=350
LIFTING HOOK FORMED AS CONTINUATION OF TIE BARS (WILL BE CUT BEFORE TESTING)
A-A
B-B
C-C
LIFTING HOOK POSITION
LIFTING HOOK
STUDS, P1 (63 PIECES)
STUDS, P1 (96 PIECES)
Ø24...776, P2
STUD,P1
10x640...9540,P22
14x640...9540,P21
PARTS
Sketcher
FL
Checked
–
Date
05.2014
Material
–
Scale
1:25
Specimen 2 - Bending
VTT
Steel fabrication

Specimen S3

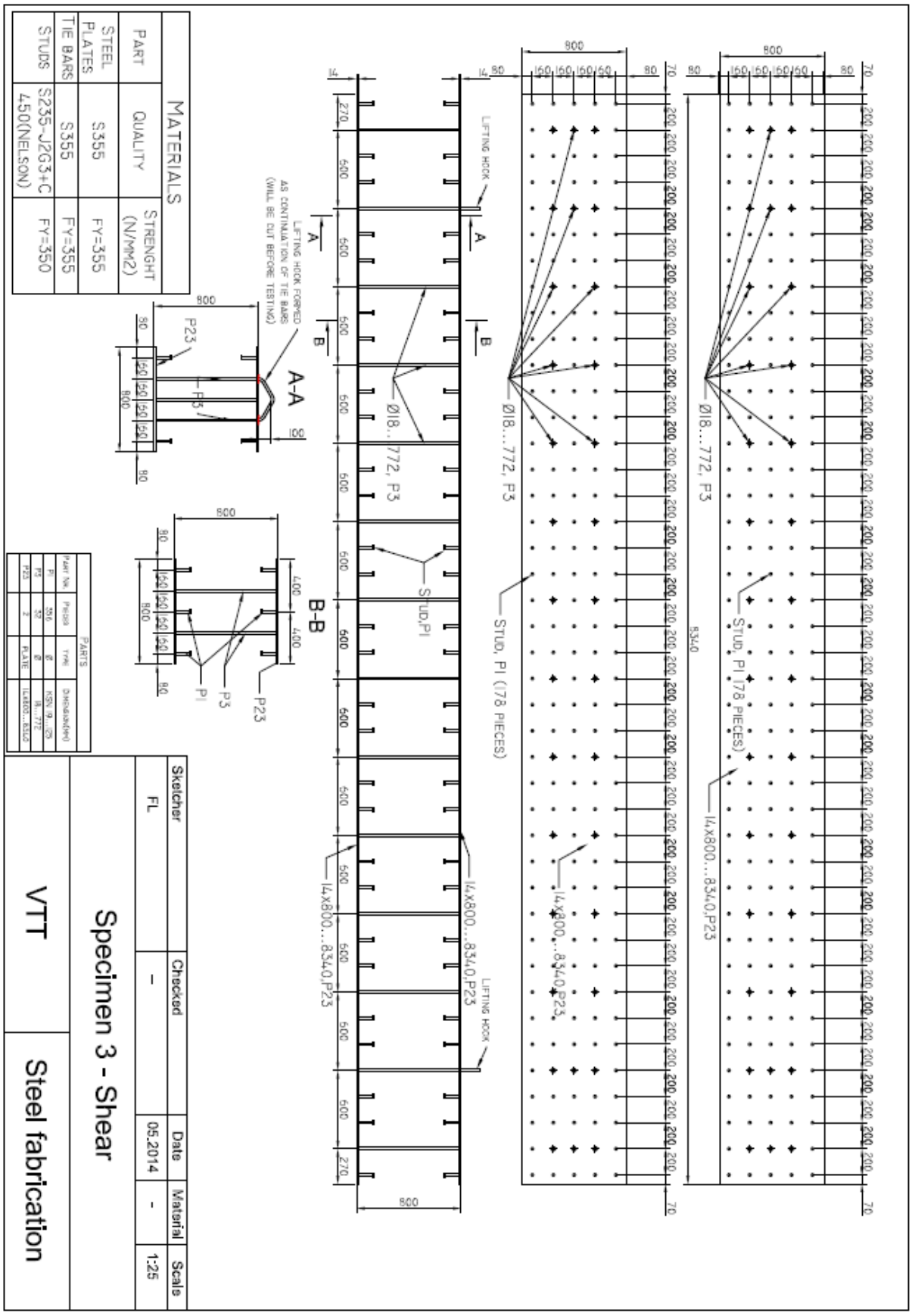
MATERIALS
PART
QUALITY
STRENGHT (N/MM2)
STEEL PLATES
S355
FY=355
TIE BARS
S355
FY=355
STUDS
S235-J2G3+C 450(NELSON)
FY=350
A-A
B-B
LIFTING HOOK FORMED AS CONTINUATION OF TIE BARS (WILL BE CUT BEFORE TESTING)
LIFTING HOOK
STUD, PI (178 PIECES)
Ø18...772, P3
14x800...8340,P23
PARTS
Sketcher
FL
Checked
–
Date
05.2014
Material
-
Scale
1:25
Specimen 3 - Shear
VTT
Steel fabrication

Specimen S4

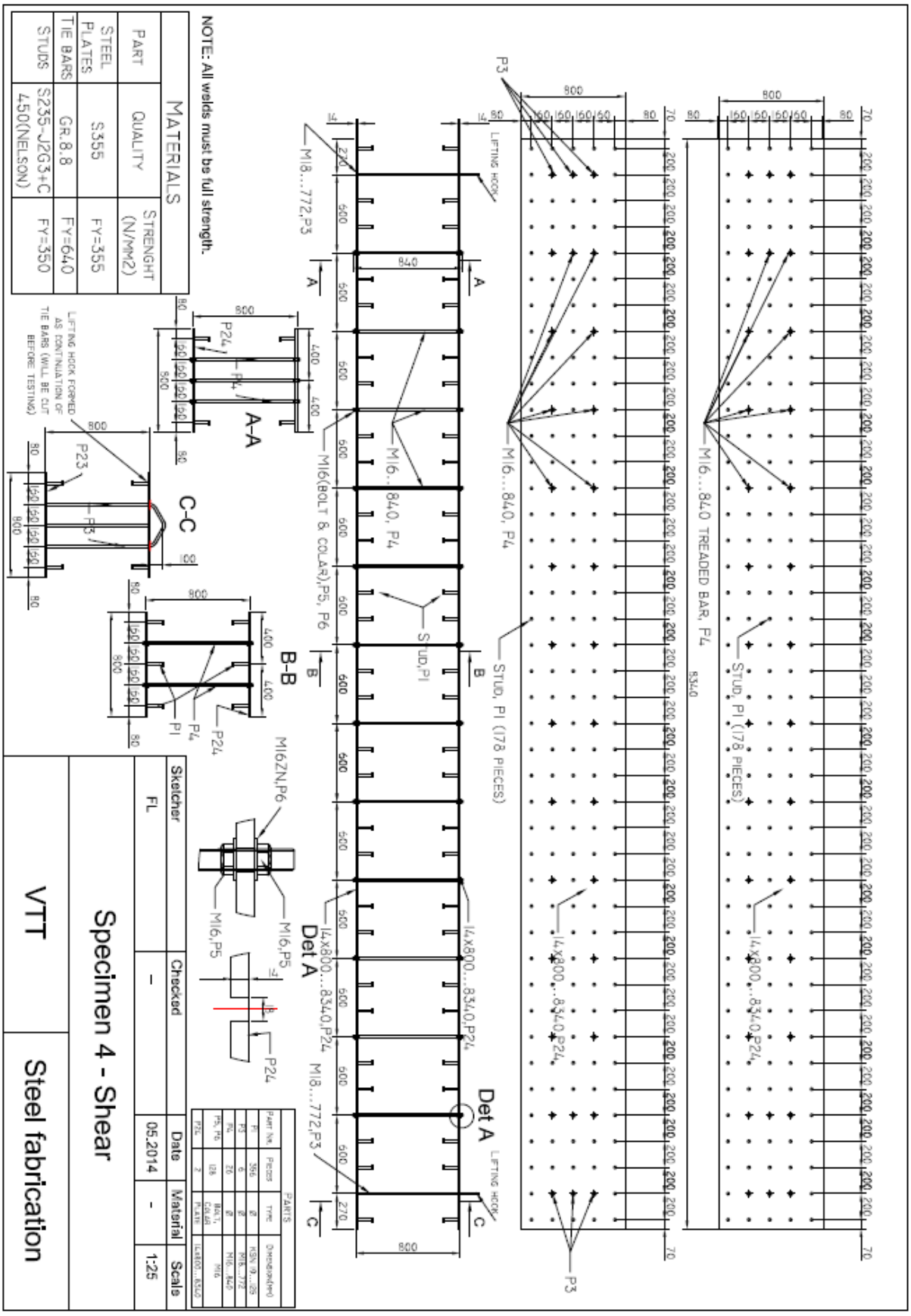
NOTE: All welds must be full strength.
MATERIALS
PART
QUALITY
STRENGHT (N/MM2)
STEEL PLATES
S355
FY=355
TIE BARS
GR.8.8
FY=640
STUDS
S235-J2G3+C450(NELSON)
FY=350
LIFTING HOOK FORMED AS CONTINUATION OF TIE BARS (WILL BE CUT BEFORE TESTING)
A-A
B-B
C-C
Det A
M16...840, P4
M16(BOLT & COLAR),P5, P6
M18...772,P3
STUD, P1 (178 PIECES)
M16...840 TREADED BAR, P4
14x800...8340,P24
M16ZN,P6
M16,P5
P24
P23
PARTS
Sketcher
FL
Checked
–
Date
05.2014
Material
–
Scale
1:25
Specimen 4 - Shear
VTT
Steel fabrication

Specimen S5

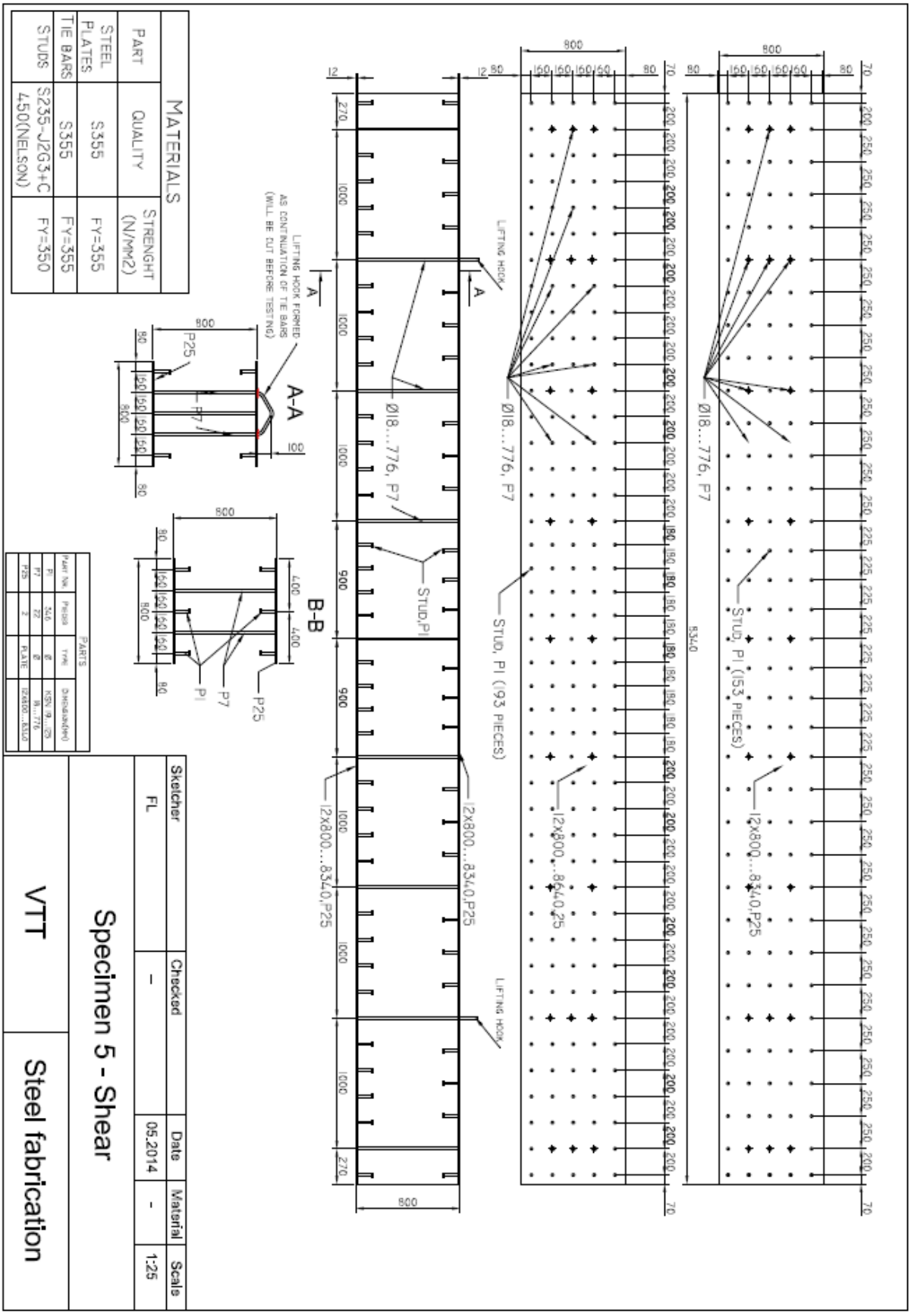
MATERIALS
PART
QUALITY
STRENGHT (N/MM2)
STEEL PLATES
S355
FY=355
TIE BARS
S355
FY=355
STUDS
S235-J2G3+C450(NELSON)
FY=350
PARTS
Part No.
Pieces
Type
Dimension(mm)
P1
346
Ø
Ø18...776
P7
22
Ø
Ø18...776
P25
2
PLATE
12x800...8340
Sketcher
FL
Checked
-
Date
05.2014
Material
-
Scale
1:25
Specimen 5 - Shear
VTT
Steel fabrication
LIFTING HOOK
STUD, P1 (93 PIECES)
STUD, P1 (153 PIECES)
Ø18...776, P7
12x800...8340,P25
LIFTING HOOK FORMED AS CONTINUATION OF TIE BARS (WILL BE CUT BEFORE TESTING)
A-A
B-B
P25
P7
P1

Specimen S6

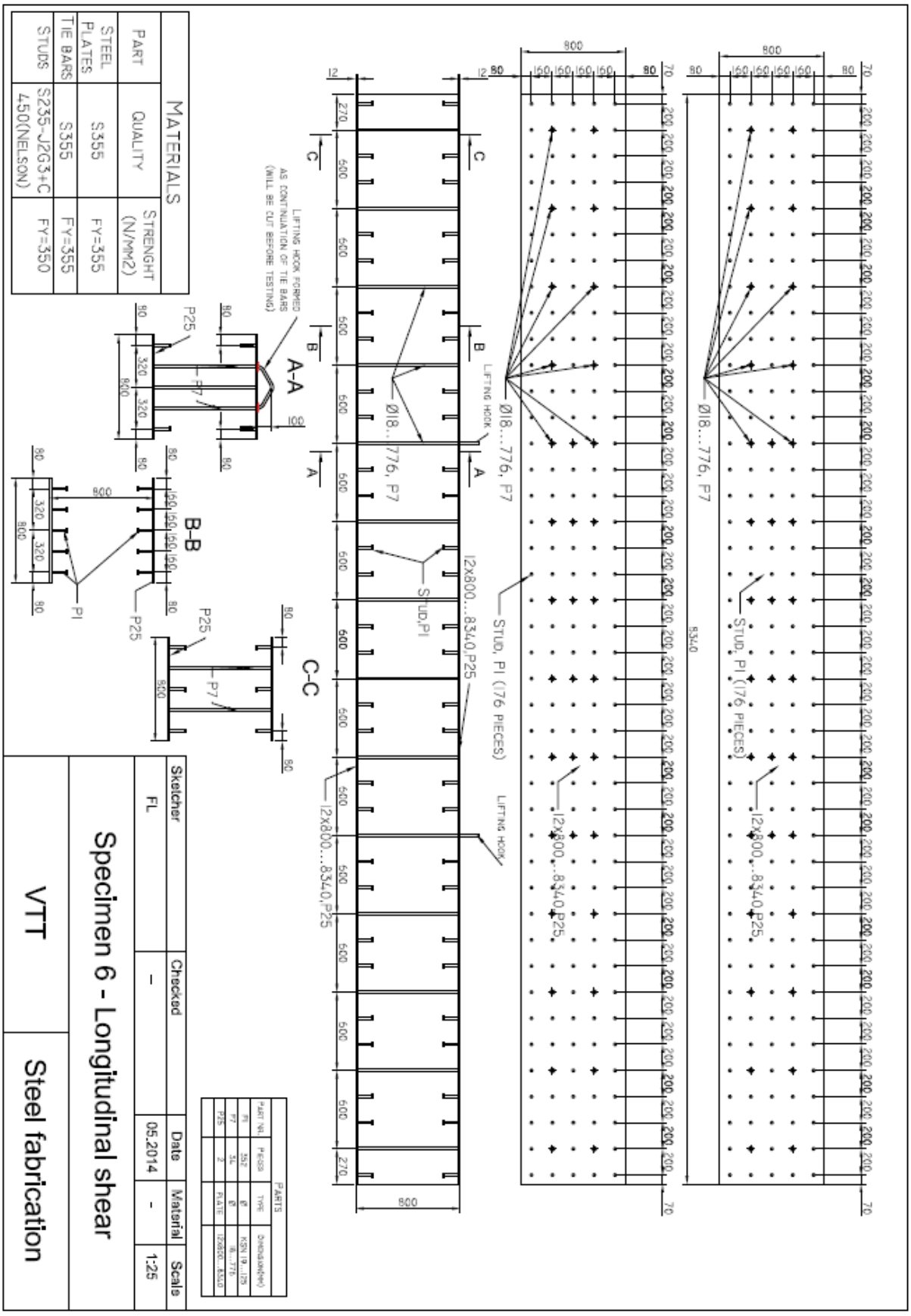
MATERIALS
PART
QUALITY
STRENGHT (N/MM2)
STEEL PLATES
S355
FY=355
TIE BARS
S355
FY=355
STUDS
S235-J2G3+C 450(NELSON)
FY=350
LIFTING HOOK FORMED AS CONTINUATION OF TIE BARS (WILL BE CUT BEFORE TESTING)
A-A
B-B
C-C
Ø18...776, P7
STUD, P1 (176 PIECES)
12x800...8340,P25
LIFTING HOOK
P1
P25
P7
Sketcher
FL
Checked
–
Date
05.2014
Material
–
Scale
1:25
Specimen 6 - Longitudinal shear
VTT
Steel fabrication

Appendix II: Strength and deformation characteristics for concrete

	Strength classes for concrete															Analytical relation / Explanation
f_{ck} (MPa)	12	16	20	25	30	35	40	45	50	55	60	70	80	90		
$f_{ck,cube}$ (MPa)	15	20	25	30	37	45	50	55	60	67	75	85	95	105		
f_{ctm} (MPa)	20	24	28	33	38	43	48	53	58	63	68	78	88	98	$f_{ctm} = f_{ck}+8$(MPa)	
$f_{ctk\ 0,05}$ (MPa)	1,6	1,9	2,2	2,6	2,9	3,2	3,5	3,8	4,1	4,2	4,4	4,6	4,8	5,0	$f_{ctm}=0,30\cdot f_{ck}^{(2/3)} \leq C50/60$ $f_{ctm}=2,12\cdot \ln(1+((f_{ctm}/10))$ $>$ C50/60	
$f_{ctk\ 0,05}$ (MPa)	1,1	1,3	1,5	1,8	2,0	2,2	2,5	2,7	2,9	3,0	3,1	3,2	3,4	3,5	$f_{ctk,0,05} = 0,7\cdot f_{ctm}$ 5% fractile	
$f_{ctk\ 0,95}$ (MPa)	2,0	2,5	2,9	3,3	3,8	4,2	4,6	4,9	5,3	5,5	5,7	6,0	6,3	6,6	$f_{ctk,0,95} = 1,3\cdot f_{ctm}$ 95% fractile	
E_{cm} (GPa)	27	29	30	31	33	34	35	36	37	38	39	41	42	44	$E_{cm} = 22[(f_{cm})/10)^{0,3}$ (f_{cm} in MPa)	
ε_{c1} (‰)	1,8	1,9	2,0	2,1	2,2	2,25	2,3	2,4	2,45	2,5	2,6	2,7	2,8	2,8	see Figure 3.2 $\varepsilon_{c1}(^0/_{00}) = 0,7\ f_{cm}^{0,31} \leq 2,8$	
ε_{cu1} (‰)	3,5									3,2	3,0	2,8	2,8	2,8	see Figure 3.2 for $f_{ck} \geq 50$ Mpa $\varepsilon_{cu1}(^0/_{00})=2,8+27[(98-f_{cm})/100]^4$	
ε_{c2} (‰)	2,0									2,2	2,3	2,4	2, 5	2,6	see Figure 3.3 for $f_{ck} \geq 50$ Mpa $\varepsilon_{c2}(^0/_{00})=2,0+0,085(f_{ck}-50)^{0,53}$	
ε_{cu2} (‰)	3,5									3,1	2,9	2,7	2,6	2,6	see Figure 3.3 for $f_{ck} \geq 50$ Mpa $\varepsilon_{cu2}(^0/_{00})=2,6+35[(90-f_{ck})/100]^4$	
n	2,0									1,75	1,6	1,45	1,4	1,4	for $f_{ck} \geq 50$ Mpa $n=1,4+23,4[(90- f_{ck})/100]^4$	
ε_{c3} (‰)	1,75									1,8	1,9	2,0	2,2	2,3	see Figure 3.4 for $f_{ck} \geq 50$ Mpa $\varepsilon_{c3}(^0/_{00})=1,75+0,55[(f_{ck}-50)/40]$	
ε_{cu3} (‰)	3,5									3,1	2,9	2,7	2,6	2,6	see Figure 3.4 for $f_{ck} \geq 50$ Mpa $\varepsilon_{cu3}(^0/_{00})=2,6+35[(90-f_{ck})/100]^4$	

Appendix III: NELSON stud catalogue

KB

NELSON BOLZENSCHWEISSEN
A FabriSteel Company

Kopfbolzen (früher BA/KD)

Werkstoff: S235 J2G3+C450, 1.4301 / 1.4303

Goujon d'ancrage/ connecteur

Matière: S235 J2G3+C450, 1.4301 / 1.4303

Shear Connector/ Concrete Anchor

Material: S235 J2G3+C450, 1.4301 / 1.4303

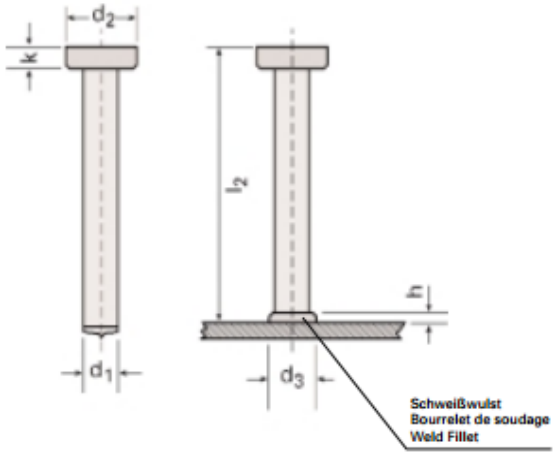

Bestellbeispiel: NELSON-Kopfbolzen Typ KB, 10 x 100 mm, S235 J2G3+C450, Bestell-Nr. 15-04-68
Exemple de commande: Goujon d'ancrage NELSON type KB, 10 x 100 mm, S235 J2G3+C450, No. de pièce 15-04-68
Ordering example: NELSON-concrete anchor type KB, 10 x 100 mm, S235 J2G3+C450, Part No. 15-04-68

Werkstoff: S235 J2G3+C450, Matière: S235 J2G3+C450, Material: S235 J2G3+C450

Ø	l_2	Bestell-Nr. / No de pièce / Part No.	Stück/Faß / Pièce/tonneau / Piece/barrel	Gewicht / Poids / Weight (kg/100)	d_1	d_2	d_3	k	h	Keramikring normal / Bague réfract. normale / Ferrule/norm. Type	Bolzenhalter / Mandrin / Chuck	Keramikringhalter / Porte-bague réfractaire / Ferrule Grip	Fußplatte / Semelle / Foot Assembly
1/4"(6)	50	15-09-17	10.000	1,6	6,35	12,7	9,7	4,7	3,0	KSN 1/4"	25-47-00	65-40-00	NS 20: 36-05-00
1/4"(6)	65	15-04-66	8.000	2,0	6,35	12,7	9,7	4,7	3,0	KSN 1/4"	25-47-00	65-40-00	NS 40: 36-06-14
1/4"(6)	100	15-05-79	4.500	2,8	6,35	12,7	9,7	4,7	3,0	KSN 1/4"	25-47-00	65-40-00	
3/8"(10)	50	15-04-82	4.500	4,1	9,52	19,05	12,5	7,1	4,0	KSN 3/8"	25-48-00	65-41-00	NS 20: 36-05-00
3/8"(10)	75	15-15-37	3.300	5,4	9,52	19,05	12,5	7,1	4,0	KSN 3/8"	25-48-00	65-41-00	NS 40: 36-06-14
3/8"(10)	100	15-04-68	2.400	6,8	9,52	19,05	12,5	7,1	4,0	KSN 3/8"	25-48-00	65-41-00	
3/8"(10)	125	15-29-20	1.900	8,2	9,52	19,05	12,5	7,1	4,0	KSN 3/8"	25-48-00	65-41-00	
3/8"(10)	150	15-11-31	1.400	9,5	9,52	19,05	12,5	7,1	4,0	KSN 3/8"	25-48-00	65-41-00	
3/8"(10)	175	15-41-34	1.000	10,8	9,52	19,05	12,5	7,1	4,0	KSN 3/8"	25-48-00	65-41-00	
1/2"(13)	25	15-16-87	4.000	5,2	12,7	25,4	17,0	8,0	5,0	KSN 1/2"	92-02-03	65-36-00	NS 20: 36-06-00
1/2"(13)	50	15-04-71	2.500	7,7	12,7	25,4	17,0	8,0	5,0	KSN 1/2"	92-02-03	65-36-00	NS 40: 36-06-15
1/2"(13)	75	15-04-72	1.800	10,2	12,7	25,4	17,0	8,0	5,0	KSN 1/2"	92-02-03	65-27-00	
1/2"(13)	100	15-04-73	1.400	12,7	12,7	25,4	17,0	8,0	5,0	KSN 1/2"	92-02-03	65-27-00	
1/2"(13)	125	15-04-74	1.100	15,2	12,7	25,4	17,0	8,0	5,0	KSN 1/2"	92-02-03	65-27-00	
1/2"(13)	150	15-21-16	900	17,7	12,7	25,4	17,0	8,0	5,0	KSN 1/2"	92-02-03	65-27-00	
1/2"(13)	175	15-28-87	700	20,2	12,7	25,4	17,0	8,0	5,0	KSN 1/2"	92-02-03	65-27-00	
5/8"(16)	35	15-28-02	2.000	9,2	15,87	31,7	21,0	8,0	7,0	KSN 16	25-50-00	65-98-00	
5/8"(16)	50	15-25-20	1.500	11,7	15,87	31,7	21,0	8,0	7,0	KSN 16	25-50-00	65-98-00	
5/8"(16)	75	15-04-77	1.200	15,6	15,87	31,7	21,0	8,0	7,0	KSN 16	25-50-00	65-29-00	NS 20: 36-06-00
5/8"(16)	100	15-04-78	900	19,5	15,87	31,7	21,0	8,0	7,0	KSN 16	25-50-00	65-29-00	NS 40: 36-06-15
5/8"(16)	125	15-04-79	700	24,2	15,87	31,7	21,0	8,0	7,0	KSN 16	25-50-00	65-29-00	
5/8"(16)	150	15-04-80	900	27,2	15,87	31,7	21,0	8,0	7,0	KSN 16	25-50-00	65-29-00	
5/8"(16)	175	15-28-55	500	31,1	15,87	31,7	21,0	8,0	7,0	KSN 16	25-50-00	65-29-00	
5/8"(16)	200	15-15-01	400	35,8	15,87	31,7	21,0	8,0	7,0	KSN 16	25-50-00	65-29-00	
3/4"(19)	50	15-04-88	1.250	16,1	19,05	31,7	24,0	10,0	9,0	KSN 19	25-50-00	65-29-00	NS 20: 36-06-00
3/4"(19)	60	15-04-89	1.100	17,6	19,05	31,7	24,0	10,0	9,0	KSN 19	25-50-00	65-29-00	
3/4"(19)	75	15-04-90	950	21,0	19,05	31,7	24,0	10,0	9,0	KSN 19	25-50-00	65-29-00	
3/4"(19)	80	15-04-91	850	22,1	19,05	31,7	24,0	10,0	9,0	KSN 19	25-50-00	65-29-00	
3/4"(19)	100	15-04-92	700	26,6	19,05	31,7	24,0	10,0	9,0	KSN 19	25-50-00	65-29-00	
3/4"(19)	125	15-04-93	600	32,2	19,05	31,7	24,0	10,0	9,0	KSN 19	25-50-00	65-29-00	
3/4"(19)	150	15-04-94	500	37,8	19,05	31,7	24,0	10,0	9,0	KSN 19	25-50-00	65-29-00	
3/4"(19)	175	15-17-95	400	43,4	19,05	31,7	24,0	10,0	9,0	KSN 19	25-50-00	65-29-00	
3/4"(19)	200	15-37-55	350	51,8	19,05	31,7	24,0	10,0	9,0	KSN 19	25-50-00	65-29-00	

Werkstoff: S235 J2G3+C450, Matière: S235 J2G3+C450, Material: S235 J2G3+C450

Ø	l_2	Bestell-Nr. / No de pièce / Part No.	Stück/Faß / Pièce/tonneau / Piece/barrel	Gewicht / Poids / Weight (kg/100)	d_1	d_2	d_3	k	h	Keramikring normal / Bague réfract. normal / Ferrule/norm. Type	Bolzenhalter / Mandrin réfractaire / Chuck	Keramikringhalter / Porte-bague / Ferrule Grip	Fußplatte / Semelle / Foot Assembly
7/8"(22)	75	15-04-95	700	27,8	22,22	34,9	28,0	10,0	10,0	KSN 22	25-51-00	65-30-00	NS 20: 36-06-00
7/8"(22)	90	15-04-97	600	32,7	22,22	34,9	28,0	10,0	10,0	KSN 22	25-51-00	65-30-00	
7/8"(22)	100	15-04-98	550	36,0	22,22	34,9	28,0	10,0	10,0	KSN 22	25-51-00	65-30-00	
7/8"(22)	125	15-04-99	450	44,2	22,22	34,9	28,0	10,0	10,0	KSN 22	25-51-00	65-30-00	
7/8"(22)	150	15-05-00	350	52,4	22,22	34,9	28,0	10,0	10,0	KSN 22	25-51-00	65-30-00	
7/8"(22)	175	15-05-01	310	60,6	22,22	34,9	28,0	10,0	10,0	KSN 22	25-51-00	65-30-00	
7/8"(22)	200	15-45-47	250	66,4	22,22	34,9	28,0	10,0	10,0	KSN 22	25-51-00	65-30-00	
7/8"(22)	250	15-45-49	200	81,3	22,22	34,9	28,0	10,0	10,0	KSN 22	25-51-00	65-30-00	
7/8"(22)	300	15-45-50	170	96,3	22,22	34,9	28,0	10,0	10,0	KSN 22	25-51-00	65-30-00	
7/8"(22)	350	15-45-51	–	111,3	22,22	34,9	28,0	10,0	10,0	KSN 22	25-51-00	65-30-00	
7/8"(22)	400	15-48–11	–	126,3	22,22	34,9	28,0	10,0	10,0	KSN 22	Sonderzubehör/Accessoire spécial/Special accessories		
7/8"(22)	525	15-45-55	–	163,7	22,22	34,9	28,0	10,0	10,0	KSN 22	Sonderzubehör/Accessoire spécial/Special accessories		
1"(25)	100	15-71-08	–	49,4	25,40	40,9	30,5	12,7	10,0	KSN 25	27-60-09	65-54-31	NS 20: 36-06-33
1"(25)	125	15-76-27	–	59,3	25,40	40,9	30,5	12,7	10,0	KSN 25	27-60-09	65-54-31	
1"(25)	150	15-69-29	–	69,3	25,40	40,9	30,5	12,7	10,0	KSN 25	27-60-09	65-54-31	
1"(25)	175	15-76-75	–	79,2	25,40	40,9	30,5	12,7	10,0	KSN 25	27-60-09	65-54-31	
1"(25)	200	15-79-98	–	89,1	25,40	40,9	30,5	12,7	10,0	KSN 25	27-60-09	65-54-31	
1"(25)	250	15-76-76	–	109,4	25,40	40,9	30,5	12,7	10,0	KSN 25	27-60-09	65-54-31	

Werkstoff: 1.4301 / 1.4303, Matière: acier inoxydable, Material: Stainless Steel

Ø	l_2	Bestell-Nr. / No de pièce / Part No.	Stück/Faß / Pièce/tonneau / Piece/barrel	Gewicht / Poids / Weight (kg/100)	d_1	d_2	d_3	k	h	Keramikring normal / Bague réfract. normale / Ferrule/norm. Type	Bolzenhalter / Mandrin / Chuck	Keramikringhalter / Porte-bague réfractaire / Ferrule Grip	Fußplatte / Semelle / Foot Assembly
1/4"(6)	50	15-04-95	10.000	1,6	6,35	12,7	9,0	4,7	3,0	KSN 1/4"	25-47-00	65-40-00	NS 20: 36-05-00
1/4"(6)	65	15-24-82	8.000	2,0	6,35	12,7	9,0	4,7	3,0	KSN 1/4"	25-47-00	65-40-00	NS 40: 36-06-14
3/8"(10)	50	15-21-13	4.500	4,1	9,52	19,05	12,5	7,1	4,0	KSN 3/8"	25-48-00	65-41-00	NS 20: 36-05-00
3/8"(10)	75	15-32-98	3.300	5,4	9,52	19,05	12,5	7,1	4,0	KSN 3/8"	25-48-00	65-41-00	NS 40: 36-06-14
3/8"(10)	100	15-24-78	2.400	6,8	9,52	19,05	12,5	7,1	4,0	KSN 3/8"	25-48-00	65-41-00	
1/2"(13)	50	15-40-55	2.500	7,7	12,7	25,4	17,0	8,0	5,0	KSN 1/2"	92-02-03	65-36-00	NS 20: 36-06-00
1/2"(13)	75	15-24-13	1.800	10,2	12,7	25,4	17,0	8,0	5,0	KSN 1/2"	92-02-03	65-27-00	NS 40: 36-06-15
1/2"(13)	100	15-24-11	1.400	12,7	12,7	25,4	17,0	8,0	5,0	KSN 1/2"	92-02-03	65-27-00	
1/2"(13)	125	15-36-18	1.100	15,2	12,7	25,4	17,0	8,0	5,0	KSN 1/2"	92-02-03	65-27-00	
5/8"(16)	50	15-47-39	1.500	11,7	15,87	31,7	21,0	8,0	7,0	KSN 16	25-50-00	65-98-00	
5/8"(16)	75	15-56-17	1.200	15,6	15,87	31,7	21,0	8,0	7,0	KSN 16	25-50-00	65-29-00	NS 20: 36-06-00
5/8"(16)	100	15-32-51	900	19,6	15,87	31,7	21,0	8,0	7,0	KSN 16	25-50-00	65-29-00	
5/8"(16)	125	15-47-41	700	23,4	15,87	31,7	21,0	8,0	7,0	KSN 16	25-50-00	65-29-00	
5/8"(16)	150	15-47-42	600	27,3	15,87	31,7	21,0	8,0	7,0	KSN 16	25-50-00	65-29-00	

Für Nelson-Kopfbolzen aus S235 J2G3+C450 und 1.4301 / 1.4303 liegt eine bauaufsichtliche Zulassung vom Institut für Bautechnik, Berlin, vor. Zulassungs-Nr.: Z-21.5-82. Außerdem liegt die „Stud Weldability Qualification" nach AWS und ASME für alle Kopfbolzen vor.

Pour les goujons connecteurs NELSON en S235 J2G3+C450 et 1.4301 / 1.4303, il existe un agrément pour le Bâtiment de l'Institut de technologie de la construction de Berlin homologation no. Z. 21.5.82. De plus teus les connecteurs NELSON font l'objet d'une homologation (Stud Weldability Qualification) selon AWS et ASME.

NELSON concrete anchors and shear connectors of S235 J2G3+C450 and material 1.4301 / 1.4303 have been approved by the Institut für Bautechnik (German Institute for Building Engineering), Berlin, under Permit Ne. Z 21.5-82. In addition, the report showing NELSON-Stud Weldability Qualifications, according to AWS and ASME, is available for all concrete anchors and shear connectors.

Kopfbolzen mit flachem Kopf auf Anfrage
Goujon d'ancrage à tête plate sur demande
Concrete anchors with special head dimensions available on request

Appendix IV: Additional Formulae

Slip deflection

$$\Delta_{SL} = \left(z_b - \frac{(CDz_b - 1)z_t}{D}\right) H_b \Big/ q^2 \Sigma EI \qquad \text{(A.1)}$$

where

$$C = \left[\frac{E_c A_{cu}(t_t + t_{cu})}{2\Sigma EI}\right] \Big/ \left[1 + \frac{E_c A_{cu}}{E_t A_t} + \frac{E_c A_{cu}(t_t + t_{cu})z_t}{2\Sigma EI}\right]$$

$$D = 1 + \frac{E_c A_{cu}}{E_t A_t} + \frac{E_c A_{cu}(t_t + t_{cu})z_t}{2\Sigma EI}$$

$$q = \sqrt{b_1 + \frac{b_2}{D}(CDz_b - 1)}$$

$$H_b = C_1 e^{qx} + C_2 e^{-qx} + \beta L/2$$

$$C_1 = -C_2 = -2\beta e^{\frac{qL}{2}} \Big/ q\left(2 + e^{qL} - \left(\frac{1 - e^{qL}}{1 - e^{-qL}}\right)\right)$$

$$\beta = \frac{(b_o + Cb_2)P}{2q^2}$$

$$b_1 = k_b\left[\frac{1}{E_b A_b} + \frac{1}{E_c A_{cu}} + \frac{z_b^2}{\Sigma EI}\right]$$

$$b_2 = k_b\left[\frac{1}{E_c A_{cu}} - \frac{z_t z_b}{\Sigma EI}\right]$$

$$b_0 = k_b \frac{z_b}{\Sigma EI}$$

$$k_b = \frac{n_b K_{s,b}}{s_{x,b}}.$$

The notation used in the above equations are given as follows:

B = width of section
E = elastic modulus
H = shear force transmitted by shear connection
h = overall depth of section
I = second moment of area
K_s = connector shear stiffness
k = shear connection stiffness per unit length
L = span of beam
M = bending moment
n = number of connectors across the width of beam
P = point load on beam
s_x = longitudinal connector spacing
u = distance of point load from support
x = distance along beam from support
z = distance between centroidal axes
Δ = deflection
ε = strain

subscripts:

b Bottom steel
c concrete
cu uncracked concrete
t top steel

Shear stiffness by Oehlers and Braford

$$S = \frac{G_c' h_c B}{k_s}$$

Notations used in the above equation are as follows:

B = width of section
G_c' = effective shear modulus
h_c = height of concrete core
k_s = stiffness of the mechanical connectors

Effective shear modulus

$$G_c' = \frac{\emptyset G_c}{1 + E_c h_c^2 / \left(6E_s \left(\frac{t_t + t_c}{2}\right) e\right)}$$

Notations used in the above equation are as follows:

e = distance between centre of the top and bottom face plate
E_c= Young's modulus of concrete
E_s= Young's modulus of steel
G_c= shear modulus of concrete
h_c = height of concrete core
$t_{c/t}$ = thickness of the compression/ tension steel plate
$\emptyset$ = shear modulus reduction factor accounting concrete crack